

**A MICROSCALE HIGH-THROUGHPUT PHENOTYPIC ASSAY TO
EVALUATE ECM REMODELING IN PULMONARY FIBROSIS**

A Dissertation
Presented to
The Academic Faculty

by

Stephen Timothy Robinson

In Partial Fulfillment
of the Requirements for the Degree
Doctor of Philosophy in
Bioengineering

Georgia Institute of Technology
August 2020

COPYRIGHT © 2020 BY STEPHEN T. ROBINSON

**MICROSCALE HIGH-THROUGHPUT PHENOTYPIC ASSAY TO
EVALUATE ECM REMODELING IN PULMONARY FIBROSIS**

Approved by:

Dr. Shuichi Takayama, Advisor
School of Biomedical Engineering
Georgia Institute of Technology

Dr. Krishnendu Roy
School of Biomedical Engineering
Georgia Institute of Technology

Dr. Eva Dyer
School of Biomedical Engineering
Georgia Institute of Technology

Dr. Nael McCarty
Department of Pediatrics
Emory University School of Medicine

Dr. Melissa Kemp
School of Biomedical Engineering
Georgia Institute of Technology

Date Approved: July 24, 2020

To everyone who helped me along the way.

ACKNOWLEDGEMENTS

I want to start by commemorating my late father, Dr. Timothy Wade Robinson. I owe most of my defining qualities to him. My passion for science & engineering, my skepticism towards accepted theories, and my determination to have a positive impact on the world all come directly from him. My father's death this past October shook our family; but we will always remember him for his love & support, his dedication to contributing to the community, and the countless sacrifices he made for us.

I need to thank the numerous students, post-docs, administrators, and professors who helped me throughout my research. In particular, I need to thank my collaborator and labmate Eric Parigoris, who continued to carry out my experiments as I grieved with my family in Baltimore and moved to Los Angeles for a fresh start. Without Eric's support, I would have neglected my final experiments and would be presenting a considerably different dissertation.

Finally, I need to express tremendous gratitude towards Professor Shuichi Takayama for his mentorship as my research advisor. Throughout my PhD, Shu placed my interests before his needs as the principal investigator of our lab. This included everything from scope of research and professional development, to work/life balance and mental health. Shu gave me the space and flexibility to formulate my own questions, make my own mistakes, and establish my own research directions.

TABLE OF CONTENTS

| | |
|----------------------------------------------------------------------------------------------------------|-------------|
| ACKNOWLEDGEMENTS | iv |
| LIST OF TABLES | vii |
| LIST OF FIGURES | viii |
| LIST OF SYMBOLS AND ABBREVIATIONS | xv |
| SUMMARY | xvii |
| CHAPTER 1. Introduction | 1 |
| 1.1 Research Objectives and Specific Aims | 1 |
| 1.2 Wound Healing and Fibrosis | 3 |
| 1.3 Pulmonary Extracellular Matrix and Cell Matrix Interactions | 4 |
| 1.4 Myofibroblasts | 6 |
| 1.5 Idiopathic Pulmonary Fibrosis | 7 |
| CHAPTER 2. Biofabrication of Phenotypic Pulmonary Fibrosis Assays | 8 |
| 2.1 Introduction | 8 |
| 2.2 Techniques for <i>in vitro</i> phenotypic analysis of pulmonary fibrosis | 16 |
| 2.2.1 Phenotypic assays incorporating epithelial damage | 16 |
| 2.2.2 Phenotypic assays incorporating fibroblast invasion | 19 |
| 2.2.3 Phenotypic assays incorporating fibroblast contraction | 22 |
| 2.2.4 Phenotypic assays incorporating collagen production and deposition | 36 |
| 2.3 Challenges in biofabrication of pulmonary fibrosis models | 39 |
| 2.3.1 Suggested design parameters for phenotypic assays of pulmonary fibrosis | 40 |
| 2.3.2 Biomaterials | 42 |
| 2.3.3 Bioprinting techniques | 44 |
| 2.4 Conclusions and future directions | 45 |
| CHAPTER 3. Aqueous Two-Phase Printing and Fibrinolysis of Fibroblast-Laden Fibrin Micro-Scaffolds | 47 |
| 3.1 Introduction | 48 |
| 3.2 Materials and Methods | 50 |
| 3.2.1 Cell culture and ATPS reagents | 50 |
| 3.2.2 Cell preparation | 51 |
| 3.2.3 ATPS printing of fibrin microgels | 52 |
| 3.2.4 High-throughput brightfield image analysis | 53 |
| 3.2.5 Phenotypic evaluation of stimuli | 53 |
| 3.2.6 Statistical Analysis | 54 |
| 3.3 Results and Discussion | 54 |
| 3.3.1 Fabrication of microscale fibrin scaffolds | 55 |
| 3.3.2 Label-free quantification of fibrin degradation | 57 |
| 3.3.3 Effects of cell seeding density and TGF- β 1 | 62 |

| | | |
|-----------------------------------------------------|-------------------------------------------------------------------|------------|
| 3.3.4 | Evaluation of hydrogen peroxide, therapeutics and IPF fibroblasts | 63 |
| 3.4 | Conclusions | 66 |
| CHAPTER 4. Lung Scarring-in-a-well | | 68 |
| 4.1 | Introduction | 69 |
| 4.2 | Materials and Methods: | 71 |
| 4.2.1 | Cell culture and ATPS reagents | 71 |
| 4.2.2 | Cell preparation | 71 |
| 4.2.3 | ATPS printing of fibrin microgels | 72 |
| 4.2.4 | Histologic analysis of fibrin microgels | 73 |
| 4.2.5 | mRNA quantification by qPCR | 74 |
| 4.2.6 | High-throughput brightfield image analysis | 75 |
| 4.2.7 | Phenotypic evaluation of stimuli | 77 |
| 4.2.8 | Statistical Analysis | 78 |
| 4.3 | Results and Discussion | 79 |
| 4.3.1 | Fabrication of microscale fibrin matrices | 79 |
| 4.3.2 | Response to TGF- β 1 | 82 |
| 4.3.3 | Label-free quantification of fibrotic remodeling | 87 |
| 4.3.4 | Evaluation of serum and cell number effects | 91 |
| 4.3.5 | Fibroblast donor variability | 93 |
| 4.3.6 | Drug response | 96 |
| 4.4 | Conclusion | 99 |
| CHAPTER 5. CONCLUSIONS AND FUTURE DIRECTIONS | | 101 |
| 5.1 | Conclusions | 101 |
| 5.1.1 | Novel fibrin remodeling assay | 101 |
| 5.1.2 | Context within the complexity of the lung | 103 |
| 5.1.3 | Fibrin remodeling as a model for IPF | 107 |
| 5.2 | Future Directions | 109 |
| 5.2.1 | High-Throughput Screening for COVID-19 Therapeutics | 109 |
| 5.2.2 | Evaluation of Nox4 Inhibitor for IPF | 110 |
| 5.2.3 | Co-culture models | 110 |
| APPENDIX A. Supplemental Information | | 112 |
| A.1 | Supplemental fibrinolysis | 112 |
| A.2 | Supplemental ECM remodeling | 115 |
| REFERENCES | | 121 |

LIST OF TABLES

| | | |
|---------|----------------------------------------------------------------------------------------------------------------------------------------------------------------------------------------------------------------------------------------------|----|
| Table 1 | Biofabricated phenotypic assays for pulmonary fibrosis. Colored dots correspond to fibrosis phenotypes, as in Figure 4. ● Epithelial injury and clot formation. ● Fibroblast invasion and differentiation. ● Contraction and ECM remodeling. | 12 |
| Table 2 | Patient-level phenotypic measurements in IPF. | 41 |
| Table 3 | Selected physical properties of the lung. | 43 |

LIST OF FIGURES

| | | |
|----------|-------------------------------------------------------------------------------------------------------------------------------------------------------------------------------------------------------------------------------------------------------------------------------------------------------------------------------------------------------------------------------------------------------------------------------------------------------------------------------------------------------------------------------------------------------------------------------------------------------------------------------------------------------------------------------------------------------------------------------------------------------------------|----|
| Figure 1 | Generalized steps of wound healing and fibrosis, whereby initial tissue injury resolves to restore functional tissue (or deposit fibrotic lesions in fibrosis) | 3 |
| Figure 2 | Elasticity and compliance of lung tissue are vital for maintaining effective gas exchange. When interstitial fibrosis interferes with the mechanical properties of the lungs, respiratory capacity gas exchange efficiency can decrease. | 4 |
| Figure 3 | Wound remodeling relies on coordinated fibrin degradation and collagen deposition. | 6 |
| Figure 4 | Simplified model of pulmonary fibrosis: Epithelial injury precedes formation of the clot-like provisional ECM. Fibroblasts invasion and differentiation accelerates wound closure by contracting and depositing ECM. The assays covered in this chapter are listed and roughly sorted by the phenotypes present in each assay, labelled by the gray arrows. | 10 |
| Figure 5 | Phenotypic assays for invasion: (a) In the Transwell scratch and invasion assay, fibroblasts are seeded on the underside of the Transwell, while epithelial cells are seeded on the top side. The epithelial layer is gently scratched with a pipet tip to remove a section of epithelial cells. After several days of culture, epithelial cells and fibroblasts may migrate into the opened area [50]. (b) The collagen plug covered in fibrin assay monitors fibroblast migration from an encapsulated collagen gel out into the surrounding fibrin gel [85]. (c) In a spheroid fibroblast invasion assay, spheroids are seeded in agarose-coated 384-well microplates. Fibroblasts added after spheroid formation can be observed invading the spheroids [56]. | 20 |
| Figure 6 | Collagen contraction adaptations: (a) Soluble, cell-laden collagen is pipeted into glass capillary tubes. After gelation, the collagen contracts linearly, enabling easy measurement of contraction [62]. (b) Teflon-coated surfaces contain the collagen gel, allowing smooth contraction without friction-induced deformations. The mineral oil layer helps confine the gel to the Teflon-coated contraction region [64]. (c) Aqueous two-phase systems (ATPS) enable formation of collagen microgels without excessive evaporation by confining soluble collagen to a dextran-rich phase until gelation. The ATPS components are washed out and floating collagen gel assay can contract [58]. | 25 |

- Figure 7 Microfabricated devices for fibroblast contraction: (a) Cell-laden collagen gels are formed inside of microfabricated, supersoft, donut-shaped wells. The cells are able to contract and deform the low elastic modulus pillars [63]. (b) Cell-laden collagen gels are seeded around micropillars. When the cells contract, the micropillars bend as predicted by cantilever solid mechanics [52]. 32
- Figure 8 Direct contact air/liquid interface: Epithelial cells are seeded on top of a fibroblast-laden collagen gel in a Transwell insert. After confluence is reached, culture media is removed from the top well, generating an air-liquid interface culture. The epithelial layer differentiates in response to the air-liquid interface. After stimulation, the collagen gel contracts, separating from the walls of the well [66]. 35
- Figure 9 Healthy function of the lungs: Requires compliant tissue that can readily expand and contract in response to diaphragmatic breathing in order to enable gas volume exchange during respiration. The line represents the volume of gas inside the lung over time. Normal tidal breathing uses a small fraction of the total lung capacity. A full inhale, followed by a full exhale (leaving residual gas volume behind) moves a volume of gas equal to the forced vital capacity (FVC). Formation of fibrotic foci interferes with this compliance due to the heterogenous accumulation of fibrous connective tissue. In the advancement of IPF, both FVC and residual volume progressively decline [129]. Models of pulmonary fibrosis could benefit from mimicking alveolar architecture and enabling fibrotic remodeling of alveolar tissue. Furthermore, phenotypic evaluation of more clinically relevant metrics such as gas volume exchange and tissue compliance may better suit evaluation of anti-fibrotic therapeutics. 39
- Figure 10 ATPS fibrin printing and cell-mediated degradation: (a) Illustration of the enzymatic control enabled by ATPS printing of fibrin scaffolds, whereby thrombin from the PEG phase diffuses into the dextran phase and crosslinks the fibrinogen into fibrin during the incubation period. (b) Process schematic of ATPS generation of microscale fibrin droplets and subsequent fibrinolysis. (c) Characteristic brightfield microscope images (taken at 4x magnification) illustrate the assay progression when stimulated with 0.5 ng/mL of TGF- β 1, showing an opaque fibrin matrix and progressive degradation. Scale bars are 1 mm. 55
- Figure 11 High-throughput quantification of fibrin degradation: (a) Automated image processing and analysis utilized Python's OpenCV library for thresholding and morphological filtering in order to establish an initial mask for each individual assay that was applied to all assay images for that well. Scale bars are 1 mm. (b) The average pixel intensity within masked regions was plotted for time course 58

evaluation, as illustrated here with different plasminogen addition times, where dotted lines indicate the plasminogen addition time and error bars represent the standard deviation between experimental replicates. (c) An example measurement demonstrates image metric extraction by fitting a logistic function to time course pixel intensity data with least squares regression. The time point for 50% degradation (d) and maximum slope from the sigmoid centroid (e) were determined using logistic functions fit for each experimental replicate. Note that the 50% degradation time (vertical axis) is indicated here as days after plasminogen addition, while the plasminogen addition time (horizontal axis) is in hours. (Statistical significance for (d, e) $P < 0.01$ by ANOVA. $ab = P < 0.01$; $bc = P < 0.05$; $ac = P < 0.1$ by post-hoc Tukey test. $N = 5$ for all conditions)

- Figure 12 Assay volume consistency: (a) ATPS printing of fibrin scaffolds demonstrated consistency in assay shape and texture between volumes. Scale bars are 1 mm. (b) Cross sectional area of assays was compared between image J, Python generated masks, and a geometric model of assay volume. (c) A doubled spherical cap demonstrated the best fit of the geometric volume models evaluated (including sphere, hemisphere, and single spherical cap). (d) Time course data shows changes in average pixel intensity for different assay volumes to demonstrate consistency in fibrin degradation time between volume conditions. Different initial pixel intensity values between conditions indicate varied transmission of light through different volume constructs. The 50% degradation time (e) and maximum slope (f) further demonstrate these trends. (Statistical significance for (b, f) $P < 0.01$ by ANOVA. $ab = P > 0.2$; $cd = P < 0.05$ by post-hoc Tukey test. $N = 4$ for all conditions) 60
- Figure 13 Cell density and TGF- β 1 effects: (a) Time course pixel intensity data demonstrates changes in fibrin degradation between different densities of cells within a 1 μ l assay. The 50% degradation time (b) and maximum slope (c) demonstrate decreased fibrinolysis time and increased slope with higher cell counts. (d) Pixel intensity data for various concentrations of TGF- β 1 indicates delays in fibrin degradation in response to the stimulus. The 50% degradation time (e) and maximum slope (f) show increases in fibrinolysis time but no significant changes in slope with higher concentrations of TGF- β 1. (Statistical significance $P < 0.01$ by ANOVA. In (b, c, e, f) $P < 0.05$ by post-hoc Tukey test between all bars with different lettered labels. $N = 4$ for all conditions) 62
- Figure 14 Cell donor and drug stimulation: Time-course pixel intensity data show the effects on fibrin degradation of several different stimulants, with NHLF cells on the left and diseased IPF cells on the right. The upper pixel intensity graphs have no TGF- β 1 (a and e) while the lower 64

graphs contain 2 ng/ml TGF- β 1 (b and f). Sigmoid fits were used to determine 50% degradation time (c, d, g and h) from the above pixel intensity graphs. (Statistical significance $P < 0.01$ independently for drug and TGF- β 1 stimulus by two-way ANOVA: As the positive control, plasmin was excluded from ANOVA. ‡ = $P < 0.01$; ad, be = $P < 0.05$; ac, fg, fh = $P < 0.1$ by post-hoc Tukey test. N = 4 for all conditions)

- Figure 15 ATPS fibrin printing and cell-mediated remodeling: (a) Process schematic of ATPS generation of microscale fibrin droplets and subsequent remodeling. After the initial pipetting step, thrombin from the PEG phase diffuses into the dextran phase for controlled crosslinking of fibrinogen into fibrin over the incubation period. Subsequent remodeling includes concurrent fibrinolysis and collagen deposition, followed by contraction. (b) Characteristic brightfield microscope images (taken at 4x magnification) illustrate the assay progression when stimulated with 2 ng/mL of TGF- β 1. Scale bars are 1 mm. (c) Microscale illustration shows the changes in ECM organization at stages of remodeling. Fibrosis denotes deposition and accumulation of fibrous extracellular protein. 80
- Figure 16 Matrix remodeling *in vitro*: (a) Brightfield images of histologic sections show the difference in final size between assays treated with varied concentrations of TGF- β 1. The contracted assays were harvested after 12 days, and sections were stained with picrosirius red. Scale bars are 250 μ m. (b) Evaluation of mean fluorescence intensity demonstrates consistency in collagen organization between conditions. Quantification of mRNA expression via qPCR evaluated dose-dependent time-course changes in *SERPENE1* (c), *COL1A1* (d), *ACTA2* (e), *PLAU* (f), *PLAT* (g), *MKI67* (h) in response to concentrations of TGF- β 1. The dotted lines indicate the zero time point used as reference for relative expression. Two-way ANOVA indicated significant combined effects of time and TGF- β 1 for *COL1A1* with $P < 0.01$; significant one-way effects for both variables with *SERPENE1*, *PLAU*, *PLAT*, and *ACTA2* with $P < 0.01$; and significant one-way effects for only TGF- β 1 concentration for *MKI67* of $P < 0.01$. 83
- Figure 17 High-throughput quantification of fibrin Remodeling: (a) The segmentation approach utilized Ilastik for pixel classification and the Python OpenCV library for thresholding and morphological filtering. Example images from diverse stages of assay remodeling were chosen to demonstrate the resilience of this segmentation approach to different image features. (b) The resulting masks enabled calculation of assay area, as illustrated here with NHLF cells and different concentrations of TGF- β 1. (c) An example measurement demonstrates image metric extraction for NHLF cells with no TGF- β 1. For each individual microwell, the logistic function is fit using a 88

least squares regression. This function enabled extraction of 50% contraction time (d), maximum contraction rate (e), and final area (f). Note that the 50% contraction time (vertical axis) is indicated here as days after start of assay, contraction rate in mm² per day, and final area in mm². (Statistical significance: ab, bc = P < 0.01; bd = P < 0.05)

- Figure 18 TGF- β 1, serum concentration, and seeding density effects: Output contraction times and final assay areas from image processing analysis were used to plot kernel density estimates showing interplay between contraction time and final assay area. (a) Stimulation with TGF- β 1 resulted in increases in both 50% contraction time and final assay area. (b) Evaluation of serum concentration demonstrated relatively consistent contraction time with increasing final assay area in response to higher serum concentrations. The disparity between apparent slope and maximum slope for 8% serum is detailed in Appendix Figure A-4. (c) Cell seeding density had an inverse relationship between contraction time and final assay area. Final contracted area is shown in mm² and statistical differences are annotated on graphs in Appendix Figure A-6. 91
- Figure 19 Consistency in response between cell lines: (a, b) Histologic sections show final contracted assays for NHLF B and IPF B with picrosirius red staining. For each example, color brightfield images are shown on the left with fluorescent images on the right. Scale bars are 250 μ m. (c-g) Individual plots for each fibroblast donor show remodeling response to TGF- β 1 and nintedanib stimulation. (h) TGF- β 1 response was compared between fibroblast donors with lines indicating the average responses with and without TGF- β 1. Final areas are indicated in mm² and statistical differences are annotated on graphs in Appendix Figure A-7. 94
- Figure 20 Response to therapeutic stimuli: (a) Time-course changes in assay area show the effects of IPF therapeutics on remodelling behavior. (b) Evaluation with therapeutics targeting the fibrinolytic system demonstrate the impact of a PAI-1 inhibitor (TM 5275) and a tPA/uPA inhibitor (aprotinin). (c) Additional experimental therapeutics were also evaluated. Final areas are indicated in mm² and statistical differences are annotated on graphs in Appendix Figure A-8. 96
- Appendix Figure A-1 Brightness correction for live cell imaging: The Incucyte S3 (Essen Biosystems) automatically adjusts image brightness to maintain white balance, with no option to manually fix the relevant settings. In order to compensate for this automated adjustment of images, brightfield micrographs were re-scaled so that the background was consistent between images. This adjustment was necessary for the volume 112

evaluation in figure 3. Here, upper images show original brightfield and lower images show adjustments made using an automated script in Python 3. These corrected images were used for analysis in figure 3 d-f. Scale bars are 1mm.

- Appendix Comparison of control conditions: Overlapping conditions from 113
Figure A-2 different experiments were compared according to cell passage number. All assays shown used 1 μ l of fibrin with 1000 fibroblasts and plasminogen added at 24 hours, with no additional stimuli. Respective conditions come from IPF therapeutic comparison in figure 5 (IPF p5), TGF- β 1 response in figure 4 (NHLF p3), NHLF therapeutic comparison in figure 5 (NHLF p5), cell number effect in figure 4 (NHLF p6), plasminogen timing in figure 2 (NHLF p12_P), and volume consistency in figure 3 (NHLF p12_V). Passage numbers were compared by time-course pixel intensity (a) and time to 50% degradation (b). (ad, ae, af, be, bf, ce, cf = P < 0.01 by post-hoc Tukey test)
- Appendix Description of Supplemental Video 1 - Fibrinolysis: This video 114
Figure A-3 demonstrates degradation of fibroblast-laden fibrin scaffolds with plasmin and plasminogen added at 24 hours. With active plasmin, the matrix degrades almost immediately; however, plasminogen is delayed due to the necessity for plasminogen to be activated by cellular activity. Graphs below each micrograph illustrate changes in average pixel intensity as determined by our automated image processing approach. Micrographs were taken by the Incucyte S3 with 4x objective.
- Appendix Area validation and time-course pixel intensity: (a) In order to 115
Figure A-4 validate the automated output from the assay mask generator, final assay sizes were compared between the automated image processing approach and ImageJ. This comparison showed no significant differences between alternate determinations of final contracted assay area. (b) Leading up to contraction, image brightness within the masked region was evaluated for different TGF- β 1 concentrations. While initial slopes appeared similar between conditions, the lines for time course pixel intensity diverged after 12-24 hours.
- Appendix Multi-step contraction and double sigmoid fit: Many conditions with 116
Figure A-5 higher concentrations of TGF- β 1 or serum contracted in a multi-step process. (a) The single sigmoid had relatively low R² values, so an alternative approach (b) using a double sigmoid was used for improved fit. This enabled more accurate determination of maximum slope.

| | | |
|------------------------|-------------------------------------------------------------------------------------------------------------------------------------------------------------------------------------------------------------------------------------------------------------------------------------------------------------------------------------------------------------------------------------------------------------------------------------------------------------------------------------------------------------------------------------------------------------------------------------------------------------------------------------------------------------|-----|
| Appendix Figure A-6 | Serum concentration and seeding density effects: (a, b) Time-course changes in assay area show the effects on assay contraction of FBS concentration on the left and fibroblast seeding density on the right. Fitting of sigmoidal functions to each experimental replicate enabled extraction of 50% contraction time (in days) (c, f) and maximum slope (d, g). Note that the disparity between apparent slope and maximum slope for 8% serum (a, d) is detailed in Appendix Figure A-5. (e, h) Final contracted area was also determined for each condition, shown in mm ² . (Statistical significance: ab, bc, ef = P < 0.05; de = P < 0.01) | 117 |
| Appendix Figure A-7 | Consistency in response between cell lines: (a, b) Histologic sections show final contracted assays for NHLF B and IPF B with picrosirius red staining. For each example, color brightfield images are shown on the left with fluorescent images on the right. Scale bars are 250µm. Time-course changes in assay area show the effects of cell line variability on assay contraction with no TGF-β1 (c) and with 2 ng/ml TGF-β1 (d). Dotted lines indicate conditions with the IPF therapeutic nintedanib. (e, f) Final contracted area was also determined for each condition. (Statistical significance: ab, cd = P < 0.01) | 118 |
| Appendix Figure A-8 | Response to therapeutic stimuli: (a, b) Time-course changes in assay area show the effects of various therapeutic stimuli on NHLF (left) and IPF fibroblasts (right) in the absence of TGF-β1. (c, d) Parallel conditions to the upper graphs show the effects of these therapeutics with addition of 2 ng/ml TGF-β1. (e, f) Final contracted area was also determined for each condition, indicated in mm ² . (Statistical significance: ab, de = P < 0.01; bc, df = P < 0.05) | 119 |
| Appendix Figure A-9 | Description of Supplemental Video 2 – ECM Remodeling: This video demonstrates altered remodeling of fibroblast laden fibrin scaffolds with different concentrations of TGF-β1. Higher concentrations result in delayed contraction and larger final size of the contracted matrix. Graphs below each micrograph demonstrate the image processing output of area masks for each time point. Micrographs were taken by the Incucyte S3 with 4x objective. | 120 |

LIST OF SYMBOLS AND ABBREVIATIONS

| | |
|--------------|----------------------------------------|
| AEC | Alveolar epithelial cell |
| α SMA | Alpha smooth muscle actin |
| BM | Basement Membrane |
| DMEM | Dulbecco's modified eagle's media |
| DMSO | Dimethyl sulfoxide |
| ECM | Extracellular matrix |
| EDTA | Ethylenediaminetetracetic acid |
| ELISA | Enzyme linked immunosorbent assay |
| EMT | Epithelial-mesenchymal transition |
| FBS | Fetal bovine serum |
| FGF | Fibroblast growth factor |
| IL | Interleukin |
| IPF | Idiopathic pulmonary fibrosis |
| KDE | Kernel density estimate |
| MMP | Matrix metalloproteinase |
| NHLF | Normal human lung fibroblast |
| PAI | Plasminogen activator inhibitor |
| PBS | Phosphate buffered saline |
| PDGF | Platelet derived growth factor |
| PFA | Paraformaldehyde |
| qPCR | Quantitative polymerase chain reaction |
| RNA | Ribonucleic acid |

ROS Reactive oxygen species
TGF- β Transforming growth factor beta
TNF- α Tumor necrosis factor alpha
tPA Tissue plasminogen activator
UIP Usual interstitial pneumonia
uPA Urokinase plasminogen activator

SUMMARY

In fibrotic disease, dysregulation of matrix remodeling generates excessive deposition of fibrous extracellular protein that can interfere with the architecture and function of tissue. The pathogenic role of aberrant fibrin remodeling is particularly interesting in idiopathic pulmonary fibrosis (IPF), which has proven largely unresponsive to conventional anti-fibrosis therapies. Due to the substantial variety of factors that combinatorially influence extracellular matrix (ECM) turnover, there exists the need for a phenotypic assay to evaluate cumulative effects involving cell-mediated fibrinolysis and collagen deposition. The goal of this project was to develop a novel *in vitro* assay that mimics fibroblast-mediated remodeling of the provisional fibrin matrix, in order to establish a model system for fibrotic scar formation and evaluate potential therapeutic compounds.

This work introduces and evaluates new methods to analyze ECM turnover in a high-throughput, label-free format. An aqueous two-phase printing technique was established to enable generation of microscale fibroblast-laden fibrin gels, which resemble the provisional fibrin matrix in wound healing. In a first variant of the assay, addition of exogenous plasminogen enabled cell-mediated activation of plasmin for gradual degradation of the fibrin matrix. While this assay for cell-mediated fibrinolysis effectively demonstrated the effects of pro-fibrotic stimuli on fibrin degradation rates, it showed no significant changes in cellular activity with established IPF therapeutics.

A second variation of the assay implemented higher fibroblast seeding densities with serum-supplemented media to facilitate remodeling of the fibrin matrix through

concurrent fibrinolysis and collagen deposition. Live-cell imaging provided time-course brightfield micrographs that were analyzed through an automated image processing protocol for high-throughput evaluation of different stages of remodeling. Stimulation of assays with IPF therapeutics demonstrated decreased formation of fibrosis. Application of this assay allowed convenient evaluation of normal and diseased donors of pulmonary fibroblasts and assessment of anti-fibrotic compounds to determine their effects on different stages of remodeling. Additionally, the differences in drug response between the two variations of fibrin assay indicated that established IPF therapeutics affect fibrotic remodeling through mechanisms unrelated to fibrin degradation.

This analysis of fibroblast-mediated remodeling of fibrin demonstrated characteristics of fibrotic ECM remodeling that are not assayed in other *in vitro* models of fibrosis. By investigating the cumulative effects of fibrinolysis and collagen deposition on fibroblastic remodeling of fibrin, this assay may provide a new resource for advancing understanding of fibrosis pathogenesis and for evaluating potential anti-fibrosis therapeutics.

CHAPTER 1. INTRODUCTION

The pathogenesis of fibrosis follows the same sequence of steps and utilizes the same biological machinery as healthy wound healing; however, in fibroproliferative disease, aberrant regulation of remodeling results in excessive accumulation of ECM. Current phenotypic assays for fibrotic activity focus on specific stages of fibrosis pathogenesis such as invasion or contraction. There are currently no phenotypic assays to broadly evaluate cumulative effects of fibrinolysis and ECM deposition on aberrant matrix remodeling.

1.1 Research Objectives and Specific Aims

This work introduces and evaluates a new method to analyze ECM turnover in a high-throughput, label-free format. An aqueous two-phase system (ATPS) is used to enable generation of microscale fibroblast-laden fibrin gels, which resemble the provisional ECM in wound healing. Fibroblasts carry out fibrinolysis, collagen deposition, and matrix contraction to remodel the matrix from fibrin into collagen and eventually contracted tissue. Compared to other *in vitro* fibrosis assays, this enables evaluation of a broader range of the steps contributing to pathogenesis. By establishing a microscale fibrosis assay that enables label free analysis of fibrinolysis and collagen deposition, this technique hopes to enable more sophisticated studies of fibrosis biology and fibrosis therapeutics than prior *in vitro* approaches.

Aim 1: Establish method for micro-printing fibroblast laden fibrin scaffolds. The first stage of this project focused on establishing a new technique to offer improved control over enzymatic crosslinking of fibrin. This was accomplished by implementing ATPS to

maintain fibrinogen and thrombin in separate phases until after the cell laden monomer solution had been dispensed. The optimization of a PEG/dextran ATPS enabled successful polymerization of sub-microliter volumes of cell-laden fibrin scaffolds, and improved control over crosslinking facilitated printing of scaffolds using standard multichannel pipettes in 96-well format. This novel fibrin printing approach enabled precise microscale control over hydrogel volume to create unprecedentedly small cell-laden fibrin scaffolds.

Aim 2: Implement fibroblast laden fibrin micro-scaffolds to evaluate cell-mediated fibrinolysis. The ATPS fibrin micro-printing approach was then utilized to develop an assay for cell-mediated fibrin degradation. Fibrin micro-scaffolds could be directly degraded through addition of plasmin, or fibrinolysis could occur through cell-mediated activation of exogenous plasminogen. A simple image processing approach was established to evaluate fibrinolysis, and fibroblasts were shown to degrade fibrin at a rate dependent on cell type, cell density, and the presence of soluble factors. This presented a novel approach to evaluate the multifactorial contributions to dysregulated fibrinolysis seen in fibrotic disease.

Aim 3: Establish fibrin remodeling assay & evaluate fibroblasts from normal and diseased donors with anti-fibrosis therapeutics. In order to broadly evaluate fibrotic remodeling another adaptation of ATPS fibrin micro-printing was implemented; where the combination of serum supplemented media, higher cell seeding density, and omission of exogenous plasminogen supported concurrent fibrinolysis and collagen deposition. A more sophisticated image processing approach from the prior aim was implemented in order to evaluate additional remodeling steps, and pro-fibrotic stimuli were evaluated for their effects on fibrinolysis, collagen deposition, and contraction. Multiple donors for normal

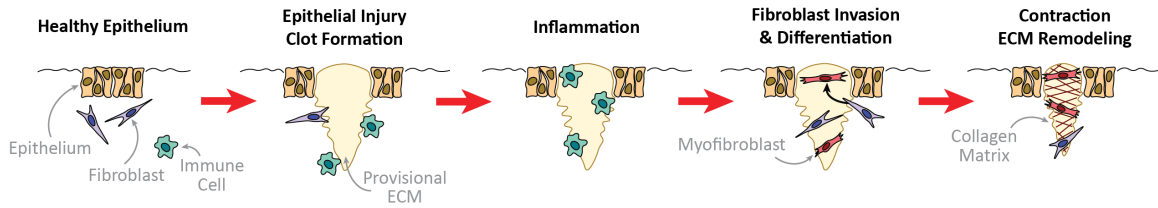


Figure 1: Generalized steps of wound healing and fibrosis, whereby initial tissue injury resolves to restore functional tissue (or deposit fibrotic lesions in fibrosis)

and diseased lung fibroblasts were utilized in order to evaluate consistency in response to therapeutic stimuli and investigate the interplay between fibrinolysis and collagen deposition.

1.2 Wound Healing and Fibrosis

Wound healing requires a coherent progression of interconnected steps to restore functional tissue. The process of wound healing is divided into multiple phases, which are labelled in

Figure 1 as clot formation, inflammation, proliferation, and remodeling [1]. After initial injury, the coagulation cascade establishes a fibrin clot to temporarily fill the wounded site. During the inflammatory phase, immune cells infiltrate the wound to prevent infection and orchestrate the recruitment fibroblasts. Next is the proliferative phase, where remodeling of the temporary fibrin matrix into collagen-dense ECM occurs [1]. Finally, during the remodeling phase, a more organized matrix resembling native ECM begins to restore healthy tissue function [1]. Dysregulation of this healing response can result in

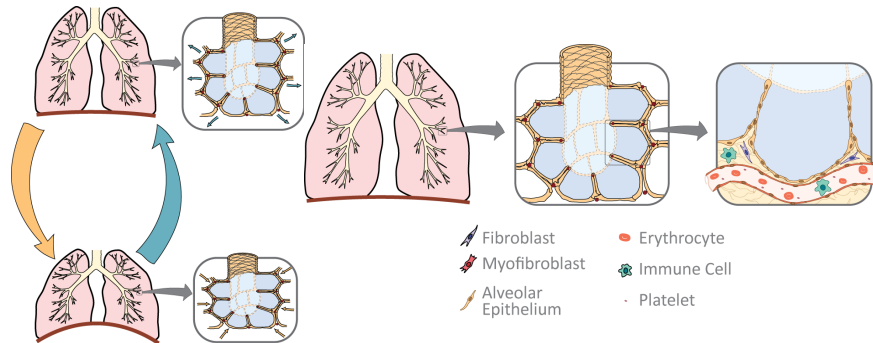


Figure 2: Elasticity and compliance of lung tissue are vital for maintaining effective gas exchange. When interstitial fibrosis interferes with the mechanical properties of the lungs, respiratory capacity gas exchange efficiency can decrease.

chronic wounds from inadequate ECM deposition or fibrotic scarring from excessive deposition. A substantial number of pathways contribute to this matrix turnover, and dysregulation can stem from a variety of sources [2]. In the lungs, matrix properties are particularly important due to biomechanical requirements for elasticity and compliance as illustrated in Figure 2. Alterations in lung architecture, such as excessive interstitial deposition of ECM, can reduce the efficacy of gas exchange leading to severe pathological conditions such as pulmonary fibrosis [3]. Specific matrix alterations and contributing biochemical pathways are detailed in the following sections.

1.3 Pulmonary Extracellular Matrix and Cell Matrix Interactions

ECM composition of the lungs plays a key role in defining the organ's physical and mechanical properties. The basement membrane in the airways consists of several ECM proteins including collagen type IV, laminin, fibronectin, and entactin; all of which are involved in regulating the diffusion of gases across the epithelial layer. Pulmonary interstitial ECM also modulates a variety of cellular functions including cell migration, proliferation, and differentiation [4]. Thus, ECM proteins play essential roles in normal

lung structure and function. Although there are several ECM components in the lung, this thesis will focus on fibrin and collagen due to their pronounced roles in fibrotic remodeling.

Fibrillar collagens are synthesized by fibroblasts in a process that is carefully regulated to maintain a balance between collagen synthesis and degradation. During pathological fibrotic remodeling, the collagen synthesis outpaces degradation and results in accumulation. Chemical signaling, biomechanical feedback, and cell-matrix interactions all contribute to maintaining this balance between synthesis and degradation [5]. The pulmonary ECM interacts dynamically with its surrounding cells, activating a variety of signaling pathways which influence cell morphology and behavior.

Cells are able to utilize the ECM for communication between cells through mechanotransduction. Integrins are the surface proteins responsible for these cell matrix interactions, and are able to mediate both cell-cell and cell-matrix interactions [6]. In addition to direct interaction with ECM protein, integrins also interact with the pro-fibrotic cytokine transforming growth factor beta I (TGF- β 1), enabling the activation of downstream signaling pathways that can increase expression of ECM proteins and ECM remodeling. Abnormal integrin signaling and elevated TGF- β 1 levels have been implicated in pathogenesis of pulmonary fibrosis [7].

Degradation activity in ECM remodeling is dependent on numerous mediators including cytokines, proteases, growth factors, mechanical forces, and lipid mediators. Collagens are primarily degraded by matrix metalloproteinases (MMPs), while fibrinolysis is predominantly mediated by the serine proteinases tissue plasminogen activator (tPA), urokinase plasminogen activator (uPA), and plasmin [8]. The dominant inhibitor of cell-

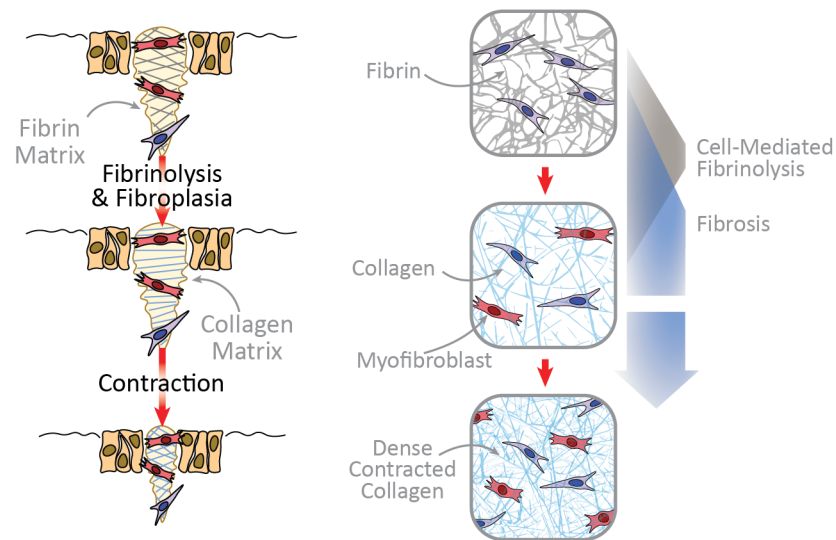


Figure 3: Wound remodeling relies on coordinated fibrin degradation and collagen deposition.

mediated fibrinolysis is plasminogen activator inhibitor type 1 (PAI-1), which has been observed in high levels in various forms of fibrosis [9, 10]. Maintaining a proper balance between fibrinolysis and collagen deposition is vital to wound remodeling (Figure 3).

1.4 Myofibroblasts

Fibroblasts are generally identified as collagen-producing cells that can anchor to the ECM; however, myofibroblasts are more synthetic and can anchor with more contractile stress than fibroblasts. These features enable the myofibroblast's key wound-healing roles in collagen production and matrix contraction. During healthy wound healing, fibroblasts differentiate into myofibroblasts and generate contractile forces through the expression of alpha smooth muscle actin (α SMA). They also produce various ECM proteins for remodeling of the damaged tissue [11]. In pathological pro-fibrotic conditions, myofibroblasts can persist and sustain excessive production of ECM components. This

excessive remodeling can disrupt tissue architecture and function [12]. During fibrosis, local fibroblasts are a major source of myofibroblastic cells. However, myofibroblasts may develop from other resident cellular precursors including alveolar epithelial cells and bone marrow-derived fibrocytes [13, 14].

1.5 Idiopathic Pulmonary Fibrosis

Idiopathic pulmonary fibrosis (IPF) is a progressive fibroproliferative disease with no known cause or cure, which affects an estimated 1 in 2000 people [15]. IPF occurs in aged demographics, and is diagnosed by histologic determination of usual interstitial pneumonia with no known underlying cause. In diagnostic CT scans and histologic sections from biopsied lung tissue, IPF is identified by presence of a variety of features including honeycombing, fibroblastic foci, excessive collagen accumulation, and loss of alveolar epithelial cells [16, 17]. Fibrotic scarring in the lungs not only disrupts the natural elasticity necessary for respiration, it also impairs gas exchange through thickening of alveolar walls [18]. Although there are two FDA-approved drugs on the market to treat IPF, neither is able to effectively halt or reverse disease progression [19]. The following chapter elaborates on current progress in developing phenotypic models of pulmonary fibrosis. Applications of these models are focused on evaluating fibrosis biology and establishing novel potential therapeutic.

CHAPTER 2. BIOFABRICATION OF PHENOTYPIC PULMONARY FIBROSIS ASSAYS*

Biofabrication techniques have enabled the formation of complex models of many biological tissues. We present a framework to contextualize biofabrication techniques within a disease modeling application. Fibrosis is a progressive disease interfering with tissue structure and function, which stems from an aberrant wound healing response. Epithelial injury and clot formation lead to fibroblast invasion and activation, followed by contraction and remodeling of the extracellular matrix. These stages have healthy wound healing variants in addition to the pathogenic analogs that are seen in fibrosis. This chapter evaluates biofabrication of a variety of phenotypic cell-based fibrosis assays. By recapitulating different contributors to fibrosis, these assays are able to evaluate biochemical pathways and therapeutic candidates for specific stages of fibrosis pathogenesis. Biofabrication of these culture models may enable phenotypic screening for improved understanding of fibrosis biology as well as improved screening of anti-fibrotic therapeutics.

2.1 Introduction

The field of biofabrication, the generation of complex structures from cellular and tissue building blocks, has seen widespread growth. These techniques may be useful in a wide variety of applications, including tissue engineering and regenerative medicine [20, 21], developmental biology, disease modeling, drug/toxicity screening models, and others. Much attention has been paid to the manufacturing aspect of biofabrication [22], but we

* This chapter has been reproduced from Yamanishi, Robinson, Takayama. *Biofabrication of phenotypic pulmonary fibrosis assays*. Biofabrication, 2019. 11(3)

focus here on a framework to consider and evaluate the application of biofabrication to disease modeling and drug screening. The design parameters for a biofabricated structure should consider the disease pathology, cellular composition, and structure. With cellular systems, unexpected structures and functions may arise in interesting ways [23]. As these systems are explored and better understood, application to disease pathology is critical for translation to effective drug screening. In this chapter, we will focus on biofabrication techniques in the context of generating phenotypic assays of idiopathic pulmonary fibrosis.

Idiopathic pulmonary fibrosis (IPF) is a devastating lung disease, in which normal lung parenchyma is progressively replaced with fibrotic scar tissue. An estimated 45% of deaths in the U.S. are attributed to disorders that are characterized by varying degrees of fibrosis, with a rising incidence [24]. Although the pathology of IPF is varied and still controversial, it generally involves dysregulation of the normal wound healing process. In a prevailing disease theory [25-28], an initial insult to the alveolar epithelial layer leads to recruitment of macrophages and other immune cells in a pro-inflammatory response (Figure 4). The epithelial injury leads to clotting and fibrin formation, accompanied by fibroblast invasion to plug the wound. The fibroblasts then proliferate and activate. Activated fibroblasts, termed myofibroblasts due to the expression of alpha-smooth muscle actin, contract the tissue and deposit extracellular matrix (ECM) to close the wound. In a healthy response, the myofibroblasts would subsequently apoptose to be cleared by macrophages, facilitating re-epithelialization and a return to the original healthy state. In pulmonary fibrosis, however, the myofibroblasts become senescent [29] and continue to generate stiff tissue. Lung stiffening is accompanied by irreversible alveolar collapse, ultimately preventing breathing in patients [30].

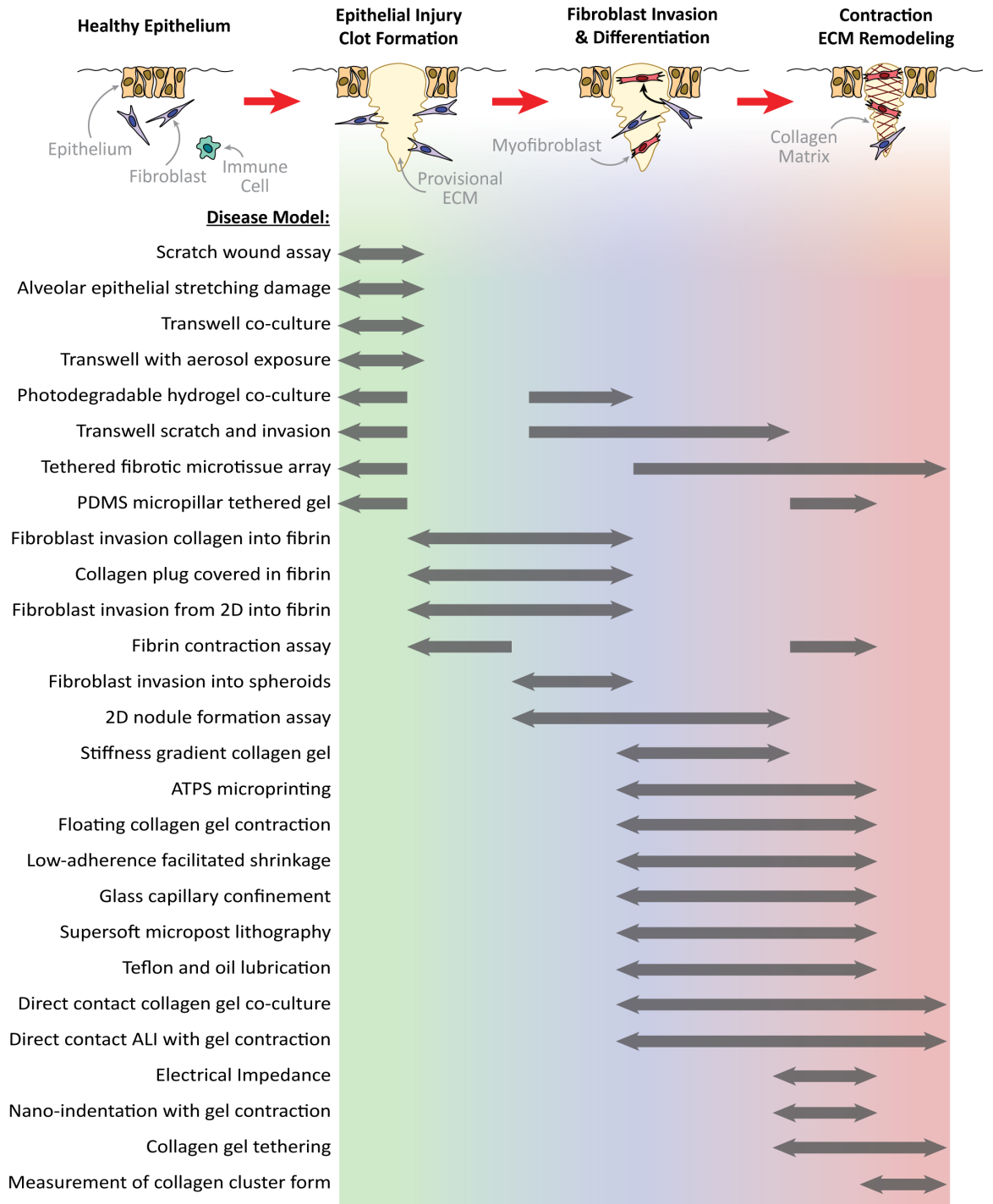


Figure 4. Simplified model of pulmonary fibrosis: Epithelial injury precedes formation of the clot-like provisional ECM. Fibroblasts invasion and differentiation accelerates wound closure by contracting and depositing ECM. The assays covered in this chapter are listed and roughly sorted by the phenotypes present in each assay, labelled by the gray arrows.

Treatment options for pulmonary fibrosis are sparse, highlighting the need for effective cellular and tissue models of the disease [31]. The standard animal model of pulmonary fibrosis uses bleomycin to generate scar tissue in rodents. This model yields lungs similar in histological appearance to fibrosis, but subtle differences from the human disease have led to misuse of the model [32]. In parallel with animal studies, there has been considerable progress in development of complex *in vitro* models of pulmonary fibrosis [33]. A subset of these models provides readouts of cell and tissue level phenotypes associated with pulmonary fibrosis. Phenotypic assays are complementary to mechanistic assays, because they can account for complex, multifactorial cell behaviors producing sometimes unexpected and emergent behavior [34-37]. Phenotypic assays have proven generally useful in the discovery of first-in-class therapeutics [38], although not yet for fibrosis. Biofabricated phenotypic assays have aided in understanding of disease pathology, particularly the role of mechanotransduction and matrix stiffness in a feedback loop of fibroblast activation [39-41]. Some of these discoveries have led to the investigation of new therapeutic targets [42, 43]. In this chapter, we will examine and contrast a variety of biofabrication techniques to assess pulmonary fibrosis phenotypes in the *in vitro* setting. This analysis aims to summarize progress and highlight challenges and opportunities in this field. We also note that while this chapter focuses on pulmonary fibrosis, many of the concepts are applicable to biofabrication of a broader range of diseases that involve fibrosis and we cite relevant examples from some of these other areas.

Table 1: Biofabricated phenotypic assays for pulmonary fibrosis. Colored dots correspond to fibrosis phenotypes, as in Figure 4. ● Epithelial injury and clot formation. ● Fibroblast invasion and differentiation. ● Contraction and ECM remodeling.

| Technique | Phenotypes | Cell types used | Exogenous materials | Additional equipment | Applications and findings | Ref |
|----------------------------------------------------------|----------------------------------------|----------------------------------------------|-----------------------------------|-----------------------------------------------------|----------------------------------------------------------------------------------------------------------------------------------------------|------|
| Scratch wound assay ● | Re-epithelialization | Primary endothelial cells and NIH3T3 | None | None | Decreased migration of primary ECs upon deletion of focal adhesion kinase | [44] |
| Alveolar epithelial stretching damage ● | Cell death | Rat alveolar epithelial type II cells | Silicone membrane | Cam motor, gasket setup | Cell death reduced by limiting the amplitude of deformation | [45] |
| Alveolar epithelial stretching damage ● | Cell death and detachment from surface | Mouse alveolar epithelial cells | PDMS membrane | Syringe pump, microfabrication | Meniscus propagation in addition to cyclic stretch resulted in additional monolayer detachment | [46] |
| Air Transwell co-culture ● | Protein expression | SAEC and endothelial | Transwell | None | Exposure of small airway epithelial cells to multi-wall carbon nanotubes induced pro-inflammatory responses in co-cultured endothelial cells | [47] |
| Transwell with aerosol exposure ● | Viability, cytokine expression | A549 | Transwell with 1 μ m pore | Nebulizer, gas containment chamber | ZnO nanoparticles induced pro-inflammatory and oxidative stress responses only above occupationally allowed exposure levels | [48] |
| Photodegradable microbeads in hydrogel co-culture ● ● | Migration | A549, human normal lung fibroblasts CCL-210. | Home-made microspheres, hydrogels | Operetta high content imaging system (Perkin Elmer) | A549 epithelial cells stimulated fibroblast migration | [49] |

Table 1 continued









| | | | | | | |
|-----------------------------------------------------------------------------------------------------------------------------------------------|----------------------------------------------------------|--------------------------------------------------------------------------------------|-------------------------------------------------|----------------------------------------------------------------|--------------------------------------------------------------------------------------------------------|-------------|
| <p>Transwell scratch and invasion</p>  | <p>Migration, wound closure, re-epithelialization</p> | <p>A549 and fibroblast (NHLF vs IPF)</p> | <p>Transwell with 8 μm pore</p> | <p>None</p> | <p>Fibroblasts from IPF patients had an impaired response to epithelial injury compared to healthy</p> | <p>[50]</p> |
| <p>Tethered fibrotic microtissue array</p>  | <p>Contraction, tearing epithelial layer, activation</p> | <p>Primary NHLF, human primary SAECs</p> | <p>PDMS, collagen, matrigel, fibronectin</p> | <p>Micropillar PDMS device</p> | <p>Pirfenidone and Nintedanib both reduce contractile and fibrotic phenotypes</p> | <p>[51]</p> |
| <p>PDMS micropillar tethered collagen gel</p>  | <p>Contraction</p> | <p>BEAS-2B normal lung epithelial cells</p> | <p>PDMS micropillars, collagen</p> | <p>Microfabrication</p> | <p>Short multi-wall carbon nanotubes stimulate contraction and pro-fibrotic phenotype</p> | <p>[52]</p> |
| <p>Fibroblast invasion from collagen into fibrin</p>  | <p>Invasion</p> | <p>Human adult dermal fibroblasts</p> | <p>Dried fibrin gels, collagen, fibronectin</p> | <p>None</p> | <p>Dermatan sulfate is a necessary proteoglycan for fibroblast invasion into fibrin gels</p> | <p>[53]</p> |
| <p>Fibroblast invasion from 2D into fibrin gel</p>  | <p>Invasion</p> | <p>Isolated human lung mesenchymal cells</p> | <p>Fibrinogen, thrombin</p> | <p>inverted phase contrast microscope</p> | <p>Fibroblast invasion into fibrin gels is CD44 dependent</p> | <p>[54]</p> |
| <p>Fibrin contraction Assay</p>  | <p>Proliferation and collagen synthesis</p> | <p>Human Dermal Fibroblasts</p> | <p>Fibrinogen, thrombin,</p> | <p>inverted microscope to measure height</p> | <p>TGF-β induced fibrin gel contraction and collagen synthesis</p> | <p>[55]</p> |
| <p>Fibroblast invasion into spheroids</p>  | <p>invasiveness</p> | <p>T47D (breast cancer), MCF7 + H1299 (lung cancer), HPF (pulmonary fibroblasts)</p> | <p>480 compound library</p> | <p>agarose for non-adherent surface for spheroid formation</p> | <p>Prostaglandins and ROCK inhibitors reduced fibroblast invasion into spheroids</p> | <p>[56]</p> |
| <p>2D nodule formation assay</p>  | <p>Nodule formation</p> | <p>Many different cells examined</p> | <p>None</p> | <p>None</p> | <p>Alk5 inhibitors and tranilast inhibited nodule formation</p> | <p>[57]</p> |

Table 1 continued

















| | | | | | | |
|-----------------------------------------------------------------------------------------------------------------------------------------------------|---------------------------------------|---------------------------------------------------------|--------------------------------------------------------|-----------------------------------------------|---------------------------------------------------------------------------------------------------------------|----------|
| Stiffness gradient collagen gel  | Activation, collagen production | Human lung fibroblasts (CCL-151) | Collagen, acrylamide, bisacrylamide, Irgacure 2959 | UV light source | Fibroblasts activate in response to stiff environments through COX-2 dependent pathway | [39] |
| Aqueous two-phase system microprinting  | Contraction | HEK 293, NIH 3T3, MC 3T3 | Polyethylene glycol, dextran, collagen | Robotic pipettor | Small volume collagen gels contract in response to 1 min of TGF- β 1 stimulation | [58, 59] |
| Floating collagen gel contraction  | Contraction | Human foreskin fibroblasts monoculture | Collagen | None | High population doubling level cells maintain contractile ability; gold standard method to assess contraction | [60] |
| Low-adherence plates facilitated collagen gel shrinkage  | Contraction | NB1RGB normal human dermal fibroblasts | Collagen | Flexcell compression | Cyclic compression induced hyaluronic acid production in fibroblasts | [61] |
| Glass capillary confinement  | Contraction | Primary human bladder-derived smooth muscle cells (SMC) | Glass capillary | None | U46619, a prostaglandin H ₂ analog, induces SMC contraction | [62] |
| Supersoft micropost lithography  | Micropost area reduction | HS-5 stromal fibroblast cell line | Microfabricated device | Microfabrication | LPA reversibly induces contractile stress in fibroblasts | [63] |
| Teflon and oil lubrication  | Contraction | Normal adult human dermal fibroblasts | Teflon-coated glass, teflon-coated washer, mineral oil | None | PDGF-BB induces fibroblast contraction | [64] |
| Direct contact collagen gel co-culture  | Macroscopic & microscopic contraction | A549, 16HBE14o-, CCD-18 lung fibroblast | Collagen | 2-photon microscope for collagen sub-analysis | Epithelial cells slow fibroblast contraction | [65] |
| Direct contact ALI with | Gel contraction | IMR-90 human fetal lung fibroblasts, | Collagen | None | Epithelial cells contribute to fibroblast expression | [66] |

Table 1 continued

| | | | | | | |
|-------------------------------------------------------------------------------------------------------------------------------------------------------------------|-------------------------------------------|--------------------------------------------------------------------------------------|-------------------------------------------|--------------------------------------------------|-----------------------------------------------------------------------------------------------------|------|
| collagen gel contraction  | | normal human bronchial epithelial cells (HBECs) | | | of MMP-9 and MMP-2 | |
| Electrical impedance  | Contraction | Human primary bronchial smooth muscle cells (BSMCs), primary lung fibroblasts (HLFs) | Gold electrode arrays | xCELLigence RTCA MP instrument | Identified non-covalent agonists and antagonists of TRPA1, applications in asthma and allergies | [67] |
| Nano-indentation with collagen gel contraction to measure contractile forces  | Contractile force | Human aortic adventitial fibroblasts | Collagen type I | Depth-sensing nanoindentation tester | Histamine-induced collagen gel contraction by fibroblasts reduced the stiffness | [68] |
| Collagen gel tethering  | Direct force measurement via strain gauge | Normal and diseased human and calf skin fibroblasts | Strain gauge | Custom strain gauge | Fibroblasts generate tensional homeostasis | [69] |
| Microfluidic droplet generation  | Not reported | 3T3 fibroblast cells | porcine gelatin, rat tail collagen type I | Blue LED for photocrosslinking, microfabrication | Fibroblasts spreading and invasion was enhanced by increased microgel stiffness | [70] |
| Optical measurement of collagen cluster formation  | Deposition | Normal primary human lung fibroblasts (WI-38) | Macromolecules (optional) | None | Known antifibrotic compounds reduced scarring; newer compound: microRNA29c found to be antifibrotic | [71] |
| Collagen microsphere generation  | None | MDA 231 cells | Collagen | Microfabrication lab | Cells were successfully encapsulated in collagen microgels and remained viable | [72] |
| Agarose-embedded collagen gels  | Contraction | U373-MG human glioma cells | Collagen, agarose | None | Microscale mechanics are more important for cell behavior than macroscale mechanics | [73] |

2.2 Techniques for *in vitro* phenotypic analysis of pulmonary fibrosis

This review is organized by describing *in vitro* cell-based assays that aim to recreate various aspects of pulmonary fibrosis pathogenesis roughly in their order of progression *in vivo*: epithelial damage, clotting, fibroblast invasion, fibroblast activation, myofibroblast contraction, and myofibroblast persistence. These techniques are summarized in Figure 4, where they are sorted roughly by the phenotypes they cover and when those phenotypes occur in a simplified model of IPF pathogenesis. Table 1 of this chapter further summarizes the techniques.

2.2.1 Phenotypic assays incorporating epithelial damage

In the context of pulmonary fibrosis, epithelial damage could arise from a variety of sources including aging, smoking, infection, inhaled toxins or nanoparticles, and a variety of other insults [74]. A common observation among IPF patients is telomere shortening. The telomere shortening hypothesis of disease pathogenesis is consistent with the strong correlation between prevalence and patient age. Assays of epithelial damage in the context of IPF should therefore include some consideration of aging, repetitive damage, or similar types of stress. Downstream biochemical signaling has been reviewed elsewhere [3, 75, 76], and should also be considered. A plethora of techniques for culturing and assaying epithelial cells exist, but this chapter will cover those assays that pertain most specifically to epithelial-fibroblast interactions in pulmonary fibrosis.

Several techniques have been developed to physically induce epithelial damage, the presumed first step towards development of pulmonary fibrosis. Some of these techniques use custom-built devices to impose cyclical strain on epithelial cells, similar to that seen in

healthy breathing. In one iteration, alveolar epithelial cells were seeded onto a flexible silicone membrane, anchored with a washer [45]. This membrane was cyclically stretched by pressing on the underside of the membrane with a motorized cam mechanism. The authors demonstrated that epithelial cells were damaged by strains of ~25%. Furthermore, additional culture time prior to cyclic strain had a protective effect on the epithelial cells. Another version of the technique comprised a stretching microdevice with flexible polydimethylsiloxane (PDMS) membrane and syringe pump hydraulic actuation [46]. This study found that air-liquid interface culture exposed cells to high damage from cyclic stretching at ~35% strain. They also examined fluid mechanical stress from liquid plug movement, finding that the damage could be reduced by addition of pulmonary surfactant. These studies examined physiological strain, but they could be adapted to replicate the fibrotic lung, which is less compliant than healthy lungs. Although hyperventilation has not been causally linked to pulmonary fibrosis, mechanical ventilation has been shown to correlate with bleak outcomes for patients with pulmonary fibrosis whose hypoxemia prompts the use of mechanical ventilation [77, 78]. These cyclic stretch models provide methods to assess the epithelial contribution to disease exacerbation.

In static culture settings, membrane culture techniques such as transwell culture have gained tremendous popularity. These devices comprise a porous membrane fixed to an insert that can be submerged into a culture well, enabling the membrane to physically separate co-culture with two distinct cell populations [47]. Transwells have also been used extensively to generate and test air-liquid interface (ALI) culture. ALI culture prompts many airway epithelial cells to differentiate into more physiologic epithelia [79]. The membrane ALI format has been adapted to allow aerosol exposure to nanoparticles in well-

plate formats [48] as well as microfluidic devices [80]. In addition to cell viability and biochemical assays, membrane cultures enable measurement of epithelial barrier integrity. Barrier function can be measured by either permeability assays using fluorescently-labeled macromolecules, such as dextran [81], or using trans-epithelial electrical resistance [82]. Transwell and membrane techniques present versatile tools for biofabrication of assays incorporating ALI epithelial components.

For analysis of epithelial injury and wound healing, the scratch wound assay is well established [44]. Briefly, a confluent monolayer of epithelial cells is denuded using a pipet tip or other blunt object to tear off the epithelial cells. The remaining edges are tracked visually as the epithelial cells proliferate and migrate to repair the wound area. A recent paper combined the scratch wound assay with Transwell co-culture [50], wherein A549 epithelial cells were grown on the top of the membrane, while primary human lung fibroblasts (normal vs IPF) were grown on the underside of the membrane, as depicted in Figure 2A. The authors reported differing behavior in normal and IPF patient-derived pulmonary fibroblasts. After scratching the epithelial layer, the A549 migrated over 4 days to close the wound. In co-culture with normal fibroblasts, the fibroblasts migrated into the wound site to plug the gap and inhibited re-epithelialization. However, pulmonary fibrosis-derived fibroblasts failed to invade the wound site, allowing the epithelium to close the wound. This study prompts interesting questions about the long-term behavior of pulmonary fibroblasts in healthy and diseased states, as the normal fibroblasts appeared more active in the short period examined than the diseased fibroblasts, contrary to what may be expected.

Despite the progress made with biofabricated assays of epithelial damage, there remains fertile ground for research regarding long-term culture, chronic epithelial damage, and downstream signaling relevant to IPF. A particularly challenging aspect of lung research has been the inability to culture alveolar epithelial cells. However, recent work has indicated that co-culture with pulmonary fibroblasts may help solve the problem [83]. New biofabrication methods could provide additional benefits by working directly with clinicians to establish cell cultures directly from the source.

2.2.2 Phenotypic assays incorporating fibroblast invasion

Following epithelial damage, a coagulation cascade results in the formation of the provisional ECM. Fibrinogen from blood plasma is cross-linked into fibrin, which is supported hydrostatically by glycosaminoglycans such as hyaluronic acid [84]. Fibroblasts from surrounding tissue then invade this provisional ECM in order to initiate the remodeling process. As illustrated in Figure 1, formation of the provisional ECM and invasion of fibroblasts is an early component of the wound healing response, where it can be exaggerated in fibrotic phenotypes [26]. A number of techniques have been developed to recapitulate behavior of fibroblasts in the provisional ECM, both for evaluation of the physiology of fibroblast invasion and for screening of potential therapeutics.

One such approach utilized a fibroblast-containing collagen matrix, formed on top of a dehydrated/rehydrated fibrin gel in media. Fibroblasts were then able to invade the fibrin matrix. This was used to evaluate the influence of fibronectin during fibroblast invasion into a fibrin matrix, and it was found that patterns of fibronectin provide a conduit for fibroblast transmigration from collagenous stroma into the fibrin clot provisional

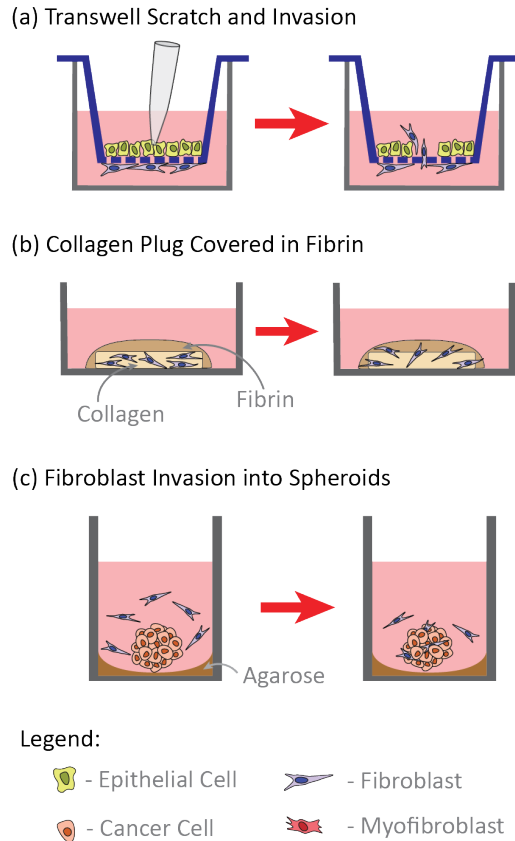


Figure 5. Phenotypic assays for invasion: (a) In the Transwell scratch and invasion assay, fibroblasts are seeded on the underside of the Transwell, while epithelial cells are seeded on the top side. The epithelial layer is gently scratched with a pipet tip to remove a section of epithelial cells. After several days of culture, epithelial cells and fibroblasts may migrate into the opened area [50]. (b) The collagen plug covered in fibrin assay monitors fibroblast migration from an encapsulated collagen gel out into the surrounding fibrin gel [85]. (c) In a spheroid fibroblast invasion assay, spheroids are seeded in agarose-coated 384-well microplates. Fibroblasts added after spheroid formation can be observed invading the spheroids [56].

matrix. Fibroblast migration began as early as 24 hours into the assay, but was significantly slowed by the removal of fibronectin [86]. This approach was used to further establish the necessity of CD44 and Syndecan-4 Proteoglycan in fibroblast invasiveness [53, 87].

Miron-Mendoza et al. used a similar assay to evaluate the differences in fibroblast migration through collagen compared to migration through fibrin. Cell-laden collagen discs were coated with fibrin for an easily imaged cell invasion assay (Figure 5B). This

was used to show that supplemental fibronectin was necessary for the invasive fibroblast phenotype, and fibroblast-fibronectin network formation was dependent on $\alpha 5\beta 1$ integrin. Fibronectin tracks (fluorescently labelled) were formed at the leading edge of migrating cells and fibroblasts preferentially migrated through pre-existing fibronectin tracks laid down by other cells [85].

Other phenotypic assays for fibroblast invasiveness have focused on migration from 2D adherent culture into fibrin matrices. One such approach used microdroplets of fibroblast suspension patterned on a 6-well plate and covered with a fibrin matrix [88]. Through this approach, migration from the 2D culture into the fibrin gel was used to evaluate invasiveness of fibroblasts isolated from patients with acute lung injuries. This was used to evaluate the role of CD44 in mediating fibroblast invasion and subsequent tissue fibrosis. By blocking the function of CD44 with monoclonal antibodies, fibroblast invasion into a fibrin matrix was inhibited [54].

An alternative, matrix-free approach focused on fibroblast invasion into cancer spheroids. This was used for evaluation of therapeutic candidates to combat fibrotic processes in cancer, but could be applied as a phenotypic assay for invasiveness in other forms of fibrosis. The approach was optimized for 384-well microplates for high-throughput evaluation of drug libraries. Tumor spheroids were formed in agarose-coated wells, as depicted in Figure 5C. A suspension of fluorescently labeled fibroblasts was then added and invasiveness was evaluated via confocal spinning disc microscopy to locate the fluorescent lung fibroblasts that had invaded the spheroids. A 480-compound library of bioactive substances was evaluated for anti-invasiveness, where several prostaglandins and ROCK inhibitors were identified as potential therapeutics [56].

Lewis et al. used a co-culture technique involving a photodegradable polyethylene glycol (PEG)-based hydrogel in order to evaluate the impact of crosstalk between fibroblasts and cancer cells on invasiveness of the fibroblasts. An Operetta high content imaging machine was used for high-throughput migration tracking in order to show the increased invasiveness and matrix metalloproteinase (MMP) expression of fibroblasts under the influence of cross-talk with cancer cells compared to fibroblasts alone [49].

Despite the involvement of the fibroblast invasion into the provisional ECM during fibrosis, there remains a question of whether it is necessary for the pathogenesis of fibrotic disease. In the case of pulmonary fibrosis, fibrin deposition does not itself appear to be required for pathogenesis because fibrinogen-null mice are still able to develop lung fibrosis after bleomycin-induced lung injury [89, 90]. Assays based on fibroblast invasion into the provisional ECM should therefore establish physiological importance before being used to evaluate compound libraries for potential therapeutic candidates.

2.2.3 Phenotypic assays incorporating fibroblast contraction

A histological hallmark of IPF is the presence of fibroblastic foci, dense clusters of cells and ECM in the lung. The characteristic cell type in these clusters is the myofibroblast. These cells are a differentiated and activated form of fibroblasts, which synthesize high amounts of collagen and contract the ECM. The myofibroblast is considered the primary effector cell in driving the progression of IPF [91]. There are extensive reviews covering the various roles and behaviors of myofibroblasts [91-95]. A plethora of biofabrication techniques have been developed to measure contraction, an identifying characteristic of the myofibroblast phenotype. The bulk of these techniques are based on collagen contraction,

but there are exceptions. Tuan et al. used a fibrin gel scaffold in their model as an analogue to the provisional ECM in wound repair. Gel contraction and collagen production were evaluated in order to show matrix remodeling under transforming growth factor (TGF- β 1) stimulation [55]. The use of other hydrogel alternatives to collagen is already covered in detail by other reviews [33, 96, 97].

2.2.3.1 Collagen gel contraction assay

Collagen gel contraction is the gold standard of phenotypic readouts for evaluation of fibrosis, with widespread use. The first reported use of a collagen gel contraction assay established the standard contraction assay format in 1979 [60]. When fibroblast-laden collagen gels are cultured in media with serum, they exhibit a high baseline level of contraction, shrinking gels to as small as 1/7th the original area within 24 hours [60, 98]. The collagen gel may adhere to the walls of the dish, so most protocols physically detach the gel from the wall using a sterile pipet tip after polymerization. The need for this step limits the throughput of collagen gel contraction assays. These assays are often called floating collagen gels [99]. The contraction has been divided into three phases: slow lag phase, rapid contraction phase, and sustained slow contraction phase [100]. During the lag phase, fibroblasts recover from trypsinization and elongate along collagen fibers. As previously reviewed [92], tensile force measurements of collagen gels indicated that the lag phase correlates with fibroblast adhesion and cell movement within the collagen gel. Therefore, the lag phase has also been called the traction phase [92]. The length of the lag phase can be shortened by using more cells, more serum, or cells at higher passage number [100]. Following the lag phase, the collagen gel is rapidly contracted and remodeled, at rates sped up by high cell number or serum concentration and slowed down by higher initial

collagen concentration or cytoskeletal inhibitors. Lastly, the system enters a state of slow, prolonged contraction.

Contraction by fibroblasts is regulated to a large extent by TGF- β 1 [101], which can be added exogenously to induce contraction [13] or it can be produced or activated by fibroblasts themselves [102], among other sources [102-104]. The combination of TGF- β 1 and tensile stress induces fibroblasts to differentiate to myofibroblasts, identified by their expression of alpha-smooth muscle actin (α -SMA), stress fibers, and high contractility [101]. It should be noted that tensile stress is also a necessary and critical component for myofibroblast differentiation [105]. The capacity for tensile stress within collagen gels can be increased by tethering gels to the dish [60] or altering gelation parameters to form stiffer gels. Gels formed at more acidic conditions down to pH 5.5 have demonstrated higher tensile strength than gels formed at more neutral or alkaline conditions up to pH 8.0 [106]. Collagen stiffness can also be increased by using higher concentrations of collagen [107].

Following the initial development of the collagen gel contraction assay, many adaptations to the format have been added. The conventional collagen contraction assay is low-throughput and high cost, due to the large consumption of collagen and cells. More modern techniques enable higher throughput with drastically lower collagen gel volumes. In addition to the cost benefit, low volume collagen gels also reduce the diffusion distance necessary for media and relevant exogenous biomolecules [58].

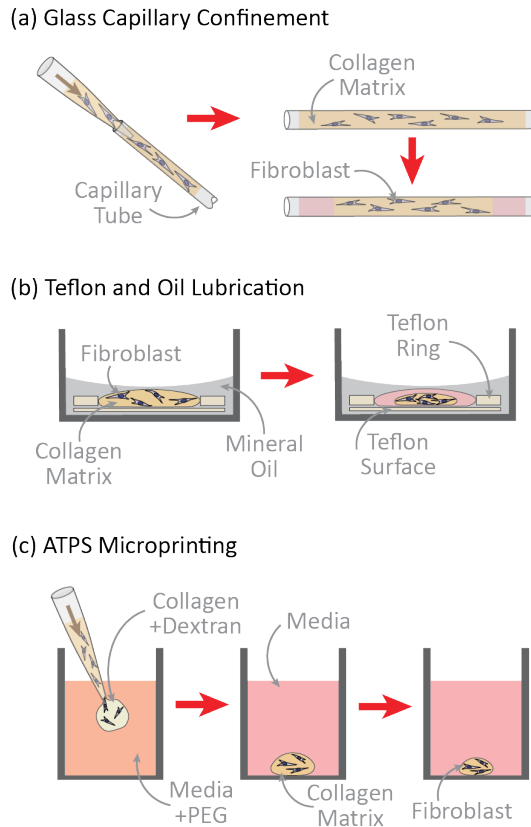


Figure 6. Collagen contraction adaptations: (a) Soluble, cell-laden collagen is pipeted into glass capillary tubes. After gelation, the collagen contracts linearly, enabling easy measurement of contraction [62]. (b) Teflon-coated surfaces contain the collagen gel, allowing smooth contraction without friction-induced deformations. The mineral oil layer helps confine the gel to the Teflon-coated contraction region [64]. (c) Aqueous two-phase systems (ATPS) enable formation of collagen microgels without excessive evaporation by confining soluble collagen to a dextran-rich phase until gelation. The ATPS components are washed out and floating collagen gel assay can contract [58].

One approach to improve assay consistency is to confine the collagen gel within a glass capillary tube, yielding a single, linear measurement, as in Figure 6A [62]. Suspended human bladder-derived smooth muscle cells in an uncured collagen solution were aspirated into glass capillary tubes and polymerized. The collagen gels were then detached from the capillary by gently applying air pressure to one end. Over 48 hours of culture, cell viability was consistent between the capillary culture method and the traditional whole well culture method. Due to the diffusive barrier introduced by the glass capillary, the stimulants and

inhibitors were added to the gel prior to polymerization. Standard deviations ran close to 1% between replicates. The authors also suggest that the capillary technique is amenable to future addition of electrical current. Although the capillary technique is limited to short-term culture applications due to diffusive limitations, it provides a consistent, easy-to-read assay that uses low volumes of collagen.

Although fibroblasts can contract collagen gels shortly after seeding, the gel can often attach to the walls and bottom surface of the well, introducing inconsistencies when measuring and analyzing the contraction. In addition to the pipet tip manual detachment method, several groups have developed techniques to consistently seed gels that cover only a fraction of the well area, often employing non-adherent surfaces to further reduce friction [61].

Sage and coworkers published a series of papers using the collagen gel contraction assay, with an array of techniques to reduce gel adhesion. They initially used agarose-coated microwells to reduce the adhesion of the collagen gels to wells [98]. In a subsequent study, however, their group designed a water-in-oil system to contain the collagen gel to a small Teflon-coated area in the center of the well, as shown in Figure 6B [64]. In this technique, a Teflon glass cloth was pinned to the bottom of a 12-well tissue culture well with a Teflon-coated washer. The pieces were then submerged in mineral oil. Collagen with suspended adult human dermal fibroblasts was then pipetted into the center of the Teflon washer ring and incubated to polymerize the gel. Interestingly, the authors found that as the collagen gel contracted, it expelled media, leaving a gel in water in oil 3-phase system. The oil and Teflon modified collagen gel contraction assay performed better than the conventional assay on multiple fronts. The gels maintained a more consistent circularity

compared to the conventional assay, wherein gels had a tendency to adhere to the well and form elongated shapes, stretched tightly between the anchor points. In addition to altering the gel shape, the anchor points in the conventional method also prevented full contraction, introducing noise to the measurements.

Furthermore, conventional assays exhibited cupping, a result of cells sedimenting to the bottom of the collagen gel as it cured, producing vertically asymmetric contraction. In the large gels, cupping can interfere with microscopy, as cells in the center of the gel are pulled to a higher plane than the cells at the bottom of the well. The pre-warmed oil facilitated more rapid polymerization, trapping cells in a more uniformly distributed state. In studies using platelet-derived growth factor (PDGF-BB) to stimulate contraction and measuring the reduction of area, Sage and coworkers achieved standard deviations of roughly 5% between replicates. While the oil and Teflon technique provides a more uniform and consistent contraction assay, it does lose some of the mechanical stress that has previously been shown to be a driving factor for fibroblast differentiation and activation [105]. The authors did not comment on this point. Additionally, the technique is rather low-throughput and still uses large volume gels. Nonetheless, their study presents a compelling case for addressing assay consistency. The widespread availability of non-adherent microplates for spheroid culture provide an accessible alternative to the Teflon-coated method.

More recently, aqueous two-phase systems (ATPSs) have been used to generate collagen microgels for contraction assays [58] (Figure 6C). Scaling down to single μL gels facilitates diffusion of stimulatory or inhibitory proteins and molecules into the center of the gel. However, these small gels evaporate during the 30 min collagen polymerization

process, often killing the embedded cells. The authors used ATPS to provide an aqueous buffer against evaporation, while confining the collagen and cells into the gel during polymerization. ATPS are phase separating solutions reminiscent of oil-water two-phase systems, but both phases contain primarily water. The distinction between phases in this particular ATPS is the presence of immiscible polymers: PEG and dextran. Conveniently, many cells and proteins partition preferentially to one phase, allowing ATPS to be used to spatially confine cells and collagen. After the collagen gel formed, the PEG and dextran were washed out and replaced with culture medium, leaving a 5 μ L cell-laden collagen gel. This technique is compatible with conventional liquid handling tools and imaging, making it appropriate for high-throughput studies. A follow-up study used the technique to produce 1 μ L collagen gels and showed excellent robustness of the technique to assess cytotoxicity in collagen gels [59]. However, the consistency and reproducibility of the microgel technique to assess contraction have not yet been established.

Several microfluidic approaches have facilitated formation of sub-millimeter collagen gels, as reviewed recently [108, 109]. These techniques use photolithography to generate channels 10s to 100s of microns in width for precise and controlled fluid mixing. Flow-focusing devices introduce a collagen-containing aqueous phase into a stream of oil to produce microdroplets of controlled size [110]. Several groups have utilized these device geometries to generate and cure cell-laden collagen microgels 10s to 100s of microns in diameter [70, 72, 111]. However, these studies have not yet examined the use of microfluidic collagen microgels in contraction assays.

2.2.3.2 Mechanics of collagen gel contraction

In parallel with the development of techniques for assay consistency and throughput, several groups have designed methods to measure more detailed mechanical information from collagen gel contraction assays. Liu et al. demonstrated the importance of substrate stiffness in pulmonary fibrosis by generating a stiffness-gradient collagen gel using photopolymerization of polyacrylamide [39]. They showed that fibroblasts are more active and responsive to TGF- β 1 on stiff substrates and less active on soft substrates. The lack of fibroblast activation was also found by inhibiting focal adhesion kinase formation with prostaglandin E2, a metabolic product produced by epithelial cells that has also been shown to suppress fibroblast activation in co-culture [112]. This technique was demonstrated as both a stiffness gradient gel and a 96-well discrete stiffness array, highlighting its versatility in probing the contractile phenotype of fibroblasts. It also provided evidence for the critical insight that fibroblasts enter a positive feedback loop, activating in response to a stiff microenvironment and contracting to exacerbate the stiffness.

A separate study used agarose to modulate collagen gel stiffness [73]. More agarose yields macroscopically stiffer gels, which can activate fibroblasts [39]. However, the agarose also reduces the effective local stiffness experienced by the cells, inhibiting the ability of the cells to cross-link and locally stiffen the matrix [73]. This study indicated that collagen concentration can increase contractility by increasing ligand availability, possibly also by reducing the ability of the collagen fibrils to slide past the agarose. The competing factors of agarose-to-collagen ratio and the collagen concentration allow fine tuning of both collagen stiffness and ligand availability.

Although the strength of fibroblast contraction can be inferred in relative terms by monitoring the shrinkage of the collagen gel, more granular mechanical information requires more advanced techniques. A variety of mechanical sensors and accompanying theoretical frameworks have been built into or applied externally to the collagen gels [11, 113]. Harley et al. made a collagen-glycosaminoglycan scaffold by freeze-drying [114]. The process generated somewhat uniform structures with repeating lattice units, allowing for single-cell microscopic measurements to be incorporated into a whole-gel solid mechanics model. The authors generated both homogeneous, isotropic structures and heterogeneous structures for comparison. They used an Euler model of buckling stress to determine how much force a cell must exert on the lattice to buckle a strut, given the strut's thickness and the overall elastic modulus of the material. Depending on the thickness of a given strut, the dermal fibroblasts exerted contractile stress of 11 to 52 nN per cell. The authors examined many individual cells buckling struts of various thicknesses and found an upper bound of 450 nN, which the cell was unable to contract. The mode of contractile failure was proposed to be at the focal adhesion. While this model provides granular information about the mechanical stresses exerted by cells, the collagen glycosaminoglycan structure represents a far stiffer matrix (~5 MPa linear elastic modulus) compared to the healthy or fibrosis lung (1-20 kPa) [39]. The analysis provided in this study could be adapted in future studies examining biofabricated materials with stiffness more relevant to pulmonary fibrosis, as well as biochemical stimuli relevant to IPF.

Another treatment of collagen gel contraction mechanics derived a solid mechanics model around a cylindrical collagen disc model [68]. The model assumes an incompressible solid with a non-linear strain-dependent elastic modulus. It uses linear

elastic mechanics to relate the area reduction and the elastic modulus (measured with a nano-indentation probe) to the bulk cell contraction force. These calculations yielded a contractile force of 1.41 nN (baseline) to 4.15 nN (activated) per human aortic adventitial fibroblast cell. The differences in substrate stiffness and cell type confound any comparisons between this method and the collagen-glycosaminoglycan scaffold calculations. One drawback to this model is the incompressible solid assumption. Several studies cited in this chapter indicate the collagen gels lose water as they compress and decrease volume [62, 64], invalidating the incompressible assumption. Nonetheless, this model provides a general method to approximate contractile forces from area reduction measurements for cylindrical collagen gels.

2.2.3.3 Strain gauge techniques

Several techniques have been developed to measure contractile forces using macroscale [69] and microscale strain gauges [11]. In most of these systems, cell-laden collagen gels are formed to span between two anchors. One or both of these anchors acts as a strain gauge. Early methods used large electronic strain gauges, converting the strain (or displacement) into a change in resistance using piezoelectric materials [69]. If the geometry and elastic modulus of the anchoring material is known, the force exerted by the cells can be calculated. Modern methods apply the same principle, but use microscale anchors and detect strain by time-lapse imaging. Because the force exerted by cells is relatively small, strains on the materials commonly used for cell culture (plastics, PDMS, etc.) can be difficult to detect. A common workaround forms the scaffold into tall micropillars, where the long torque arm and cantilever action amplifies the distance that the micropillar moves in response to the nN-scale cell contractile forces [11].

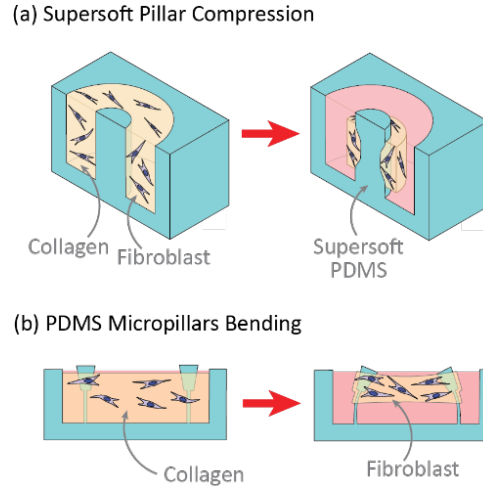


Figure 7. Microfabricated devices for fibroblast contraction: (a) Cell-laden collagen gels are formed inside of microfabricated, supersoft, donut-shaped wells. The cells are able to contract and deform the low elastic modulus pillars [63]. (b) Cell-laden collagen gels are seeded around micropillars. When the cells contract, the micropillars bend as predicted by cantilever solid mechanics [52].

Another technique to measure the contractile force of fibroblasts used supersoft PDMS to generate microposts inside donut-shaped wells, as shown in Figure 7A [63]. Although hydrogels and other supersoft materials can be produced, these materials often suffer from tearing during demolding in traditional replica molding techniques. The supersoft PDMS technique addressed the problem by using ‘hard candy’ recipes to generate sacrificial replica molds [63]. This technique enabled fabrication of PDMS microwells with 200 μm diameter microposts and an elastic modulus on the order of 0.1 kPa. Fibroblast-laden collagen gels were centrifuged into the microwells, where they formed a ring around the post. When the fibroblasts contracted, they squeezed the post. Solid mechanics analysis enabled the calculation of contractile force on the post by measuring the reduced post area. The authors reported the force exerted as a bulk radial stress and did not calculate a per-cell force. The authors also demonstrated the ability to

detect an initial contraction, apply an inhibitor, then see the cells and the post relax back toward its original shape, demonstrating reversible elastic compression.

Chen et al. modified the tethered collagen gel format to work at the microscale, as shown in Figure 7B [52]. They tested epithelial cells by treating the cells with multi-walled carbon nanotubes (MWCNTs) in the culture flask prior to seeding in the microdevice. Cells were then suspended and seeded into the microdevices along with type I collagen by centrifugation. The microtissues formed and detached from the outer walls within 12-24 hours, with cultures lasting for 1 week without detaching from the micropillars, due to their goblet shape. The authors found that low concentrations of MWCNTs increased contraction force, while high concentrations inhibited contraction force. The low dose conditions corresponded to a state of inflammation and activation, indicated by contraction, presence of reactive oxygen species (ROS), and miR-21 expression. The high dose caused considerable cell death, offsetting the activation, as measured by the contraction force. This study demonstrates the need for multifactorial analysis of phenotypic screens, as counteracting influences may confound the interpretation of results. In this case, measurement of both cell activation (contraction force and ROS production) and cell viability elucidated the behavior along a dose-response curve that indicated peak bulk pathologic behavior at a medium concentration.

The same group used a similar approach to evaluate anti-fibrotic therapeutics using their *in vitro* assay [51]. Fibroblasts were suspended by micropillars in a super thin (35 - 55 μm) collagen layer arranged in a leaflet shape in order to mimic the geometry of alveoli. Contractile forces in the collagen were measured by deflection of the micropillars that suspended the collagen and differentiation of fibroblasts into myofibroblasts was

confirmed by staining for α -SMA. This assay was then used to evaluate the therapeutics Nintedanib and Pirfenidone through measurement of both changes in tissue compliance and differentiation of fibroblasts into myofibroblasts. They confirmed anti-fibrotic activity with both drugs. This paper also used an alternative implementation of the micropillar supported collagen membrane to evaluate traction bronchiectasis, a condition involving irreversible dilation of bronchi and bronchioles as a result of pulmonary fibrosis. By modulating the rigidity of the micropillars, it was shown that increased stiffness in lung tissue due to fibrosis would compound lung damage as seen in traction bronchiectasis.

2.2.3.4 Co-culture collagen gel contraction assays

The interplay between epithelial cells and fibroblasts may be a key component of pulmonary fibrosis pathology [27]. In an early study, A549 or bronchial epithelial cells were seeded directly on top of fibroblast-laden collagen gels [65]. Compared to the fibroblast monoculture, the co-culture gels showed less total contraction over 15 days. The authors fit an exponential decay curve to the area reduction, finding that the co-culture gel had the same time constant as the monoculture, despite the differences in total extent of contraction. Furthermore, the authors used two-photon microscopy to show that co-culture decreased the degree of collagen crosslinking, as inferred by two-photon fluorescence intensity.

In another co-culture study, Ishikawa et al. prepared a similar collagen contraction gel with human bronchial epithelial cells seeded directly on top of the gel. However, this study also introduced air-liquid interface culture, as depicted in Figure 8 [66]. These gels were not manually detached and remained in place for 21 days before stimulation. The gels

Direct Contact ALI with Contraction

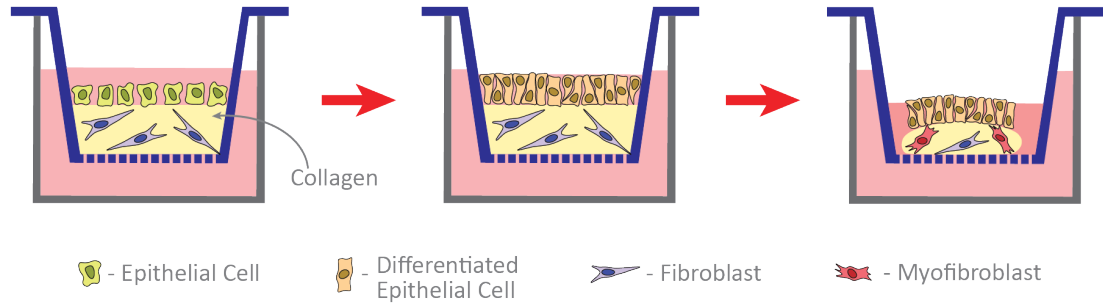


Figure 8. Direct contact air/liquid interface: Epithelial cells are seeded on top of a fibroblast-laden collagen gel in a Transwell insert. After confluence is reached, culture media is removed from the top well, generating an air-liquid interface culture. The epithelial layer differentiates in response to the air-liquid interface. After stimulation, the collagen gel contracts, separating from the walls of the well [66].

detached by cell contraction when cells were stimulated with TGF- β 1. Histology slices of the microtissue demonstrated that TGF- β 1 also induced a decrease in epithelial layer thickness. Immunostaining in these histological slices also revealed changes in MMP and tissue inhibitor of metalloproteinase (TIMP) expression due to the crosstalk between co-cultured cells. These techniques demonstrated the synergistic interactions often seen in co-culture approaches.

The biochemical mechanisms of epithelial-fibroblast co-culture have been reviewed [75]. Growing evidence indicates that epithelial cells secrete a variety of biochemical signals to regulate fibroblast behavior. Biofabrication of phenotypic IPF assays would benefit from consideration of this cross-communication.

2.2.3.5 Alternative techniques to measure fibroblast contraction

A recently developed technique enables measurement of cell contraction based on the cell coverage of the culture surface. The xCELLigence platform uses electrodes

patterned on the surface of a culture plate to measure the electrical impedance past the cells [67]. As the cells contract, they tighten and narrow, exposing electrode surfaces. The exposed surfaces pass current more easily, as the resistance from the cells is removed. One of the key benefits of this technique is its rapid response time. However, that may be more useful in studies of rapid contraction, as seen in muscle and cardiac tissues rather than the progressive contraction typically observed in fibrosis.

2.2.3.6 Discussion of contraction assays

As the key effector phenotype of IPF, considerable progress has been made to develop biofabrication techniques assessing contraction. However, one key phenotype that is missing from these cell-based contraction assays is the divergence between physiological contraction, which resolves, and pathophysiological contraction, which persists and progresses. The standard collagen gel contraction assay moves only in the direction of contraction, with little consideration or potential for reversal. The ability of epithelial cells to delay activation and contraction of fibroblasts [66] presents a promising building block for future biofabrication of assays that reflect the divergence of healthy contraction resolution and pathologic IPF persistence.

2.2.4 *Phenotypic assays incorporating collagen production and deposition*

In addition to collagen contraction, the production and deposition of new collagen by fibroblasts is a key event in disease progression. Collagen is produced by multiple cell types, but fibroblasts and myofibroblasts are responsible for the increase in collagen deposition seen in pulmonary fibrosis. The excessive accumulation of collagen seen in fibrosis is a product of both increased collagen production due to changes in transcriptional

regulation and decreased degradation modulated by altered expression of various MMPs and cathepsins [115]. In order to evaluate the contributions to collagen accumulation, many approaches have paralleled the clinical approaches based on staining biopsies and evaluating serum biomarkers [116, 117]. Histologic approaches generally utilize sirius red and picosirius red, however these methods lack specificity for collagen types [118]. Immunostaining enables identification of specific collagens, however quantification of collagen can still be challenging with these approaches. Methods based on soluble byproducts of collagen production and degradation have utilized radiolabelled amino acids and ELISAs [116, 117]. Other approaches specific to *in vitro* models have focused on evaluation of transcription PCR or electrophoretic mobility shift assay methods [119]. An alternative approach to evaluation of collagen remodeling focuses on quantification of collagen alignment [120]. Despite the wide array of collagen production assays, few biofabrication studies have utilized them.

A study of kidney mesangial cells in 2D culture indicated that they respond to TGF- β 1 by forming clusters, or nodules, that somewhat resemble the nodules seen in human pulmonary fibrosis [57]. Immunostaining of these nodules indicated localized deposition of collagen. The nodule assay was later adapted in several different publications, one of which used the assay to screen Chinese herbal medicine extracts for inhibition of kidney fibroblast nodule formation [121]. Another similar study found that macromolecular crowding with dextran sulfate causes much higher collagen deposition by fibroblasts [71]. Neutral macromolecular crowding with Ficoll produces less elevated, but more sustained collagen deposition with greater cross-linking. Collagen deposition was assessed and screened using immunochemical staining and optical microscopy of the cluster formation.

This 2D method lacks the complex microenvironment of some of the other techniques, but it does provide disease-relevant information by assessing the collagen deposited by the fibroblasts.

In addition to collagen, fibronectin and elastin play substantial roles in pulmonary fibrosis. Fibronectin is also an important ECM component that shows increased expression in various forms of pulmonary fibrosis [122] and can be quantified by analogous methods to those used for collagen. Globular fibronectin in blood serum is integrated in the fibrin matrix during formation of the provisional ECM [123] and plays a major role in invasion of fibroblasts into the provisional matrix [86]. Fibronectin expression can be up-regulated by treatment with TGF- β 1 [124]. Fibronectin also binds a large number of growth factors that may promote myofibroblast differentiation [125]. Furthermore, a comparison between 2D and 3D models of fibroblast adhesion highlighted the importance of 3D scaffolds in interactions between fibronectin and integrins [126]. This demonstrates the importance of 3D biofabricated models in evaluation of ECM remodeling. Elastin is another ECM component of interest in pulmonary fibrosis due to its roles in absorption of mechanical loads and preventing tissue damage [127]. This role in maintaining elasticity and breaking strength in lung tissue makes elastin homeostasis vital in maintenance of lung function. However, elastin expression is up-regulated in pulmonary fibrosis, contributing to the increased stiffness of fibrotic lung tissue [128]. Due to the importance of ECM composition in lung function, future biofabricated phenotypic assays for pulmonary fibrosis may consider including evaluation of expression of various ECM components.

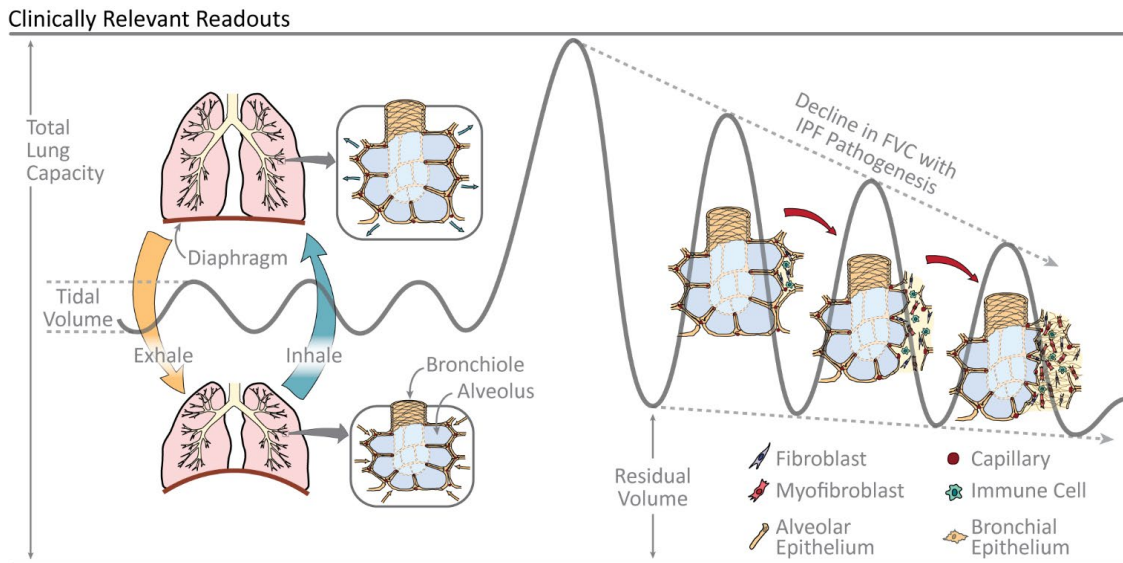


Figure 9. Healthy function of the lungs: Requires compliant tissue that can readily expand and contract in response to diaphragmatic breathing in order to enable gas volume exchange during respiration. The line represents the volume of gas inside the lung over time. Normal tidal breathing uses a small fraction of the total lung capacity. A full inhale, followed by a full exhale (leaving residual gas volume behind) moves a volume of gas equal to the forced vital capacity (FVC). Formation of fibrotic foci interferes with this compliance due to the heterogenous accumulation of fibrous connective tissue. In the advancement of IPF, both FVC and residual volume progressively decline [129]. Models of pulmonary fibrosis could benefit from mimicing alveolar architecture and enabling fibrotic remodeling of alveolar tissue. Furthermore, phenotypic evaluation of more clinically relevant metrics such as gas volume exchange and tissue compliance may better suit evaluation of anti-fibrotic therapeutics.

2.3 Challenges in biofabrication of pulmonary fibrosis models

Despite the considerable progress in the field of phenotypic assays, there remains opportunity to design microtissues that better capture the complex microenvironment of the lung. Specifically, there is a lack of appropriate alveolar models. Existing alveolar models typically use artificial substrates to provide the thin membrane structure [130]. Although most lung microtissue models use static air or flow-over gas exchange, recent work has incorporated more physiologic diaphragmatic breathing [130]. However, these models have not been shown to allow the cells to remodel the space, generating healthy or

fibrotic tissue. Furthermore, these models generate cell monolayers, lacking the complex and interconnected structure of native alveoli, as in Figure 9. This type of architecture and cell-driven assembly and construction is a ripe area for the field of biofabrication, biomaterials, and bioprinting. In this section, we discuss relevant physiological parameters and considerations for adaptation into biofabricated microtissue.

2.3.1 Suggested design parameters for phenotypic assays of pulmonary fibrosis

Problems associated with pulmonary fibrosis are predominantly caused by the accompanied decline in respiratory function. Excess accumulation of fibrous connective tissue interferes with the architecture and function of the lungs, such that gas exchange is restricted [131]. This restriction is caused by a number of factors including a decrease in number of functional alveoli and an increase in the mechanical stiffness of lung tissue [132]. Figure 9 illustrates how fibrotic foci in the lung can interfere with gas exchange at the level of individual alveoli.

To extract biological information from a fibrotic microtissue, the cells should have an opportunity to remodel their own microenvironment. Compared to the phenotypic assays presented in this chapter, modern biofabrication techniques, such as bioprinting, hold additional potential for their ability to use bioactive and degradable bioinks, while still establishing complex structures. A major shift in microtissue phenotypic assays would examine restoration of function, rather than only measuring therapeutic interventions at the point of disease progression/exacerbation.

To recapitulate the restoration of lung function, consideration of relevant patient-level measurements may be informative. In patients, overall lung decline is typically

measured in four ways: forced vital capacity (FVC - the maximum volume of air that can be inhaled and exhaled), carbon monoxide diffusion capacity (DLCO, a measure of gas transfer efficiency across the alveolar-capillary membrane), dyspnea (shortness of breath) and oxygen saturation after exertion (6-minute walk test). Each of these measurements reflect aspects of the total lung decline in pulmonary fibrosis. The FVC reflects a decline in compliance and the fraction of volume occupied by gas. Both DLCO and the 6-minute walk test assess the ability of the lungs to transfer oxygen species into the blood, while dyspnea may reflect an inability to effectively remove carbon dioxide. The reduction in gas exchange results from both a thickening of the alveolar wall and the reduction in the volume of gas exchanged in a full breath, as indicated by the reduction in FVC. Typical values for these measurements are included in Table 2. Incorporation of these patient-level measurements to a model would provide more directly relevant phenotypic readouts.

Table 2: Patient-level phenotypic measurements in IPF.

| Macroscopic patient phenotypic parameter | Description | Functions measured | Numbers | Ref |
|--------------------------------------------------|-------------------------------------------------------------------------------------------------------|--------------------------------------------------------|------------------------------------------------------------------|------------|
| Forced vital capacity (FVC) | Max volume of air that can be inhaled and exhaled in a single breath. | Volumetric gas exchange | >10% decrease indicates disease progression | [133, 134] |
| Dyspnea | Shortness of breath | Gas exchange, inability to respond to ventilator needs | NA | [134, 135] |
| 6-minute walk test. | The patient is instructed to walk for 6 minutes, after which the blood oxygen saturation is measured. | Gas exchange measurement with stress test | 6MWT followed by desaturation (<88%) | [134] |
| Carbon monoxide diffusion capacity (DLCO) | Measure of the conductance of gas transfer from inspired gas to red blood cells | Gas exchange at the blood level | Lower in IPF [136] Drop of >15% indicates disease progression | [133] |

2.3.2 *Biomaterials*

As biofabricated models of pulmonary fibrosis become more sophisticated, it is important to mimic the physiological parameters of both healthy and fibrotic lung tissue, particularly with the selection of biomaterials. General guides for selecting biomaterials for biofabrication have been published [137-140]. In the lungs, the dominant ECM components are collagen IV, laminin, entactin, and proteoglycans in basement membranes; and fibrillar collagens, elastic fibers, and proteoglycans in interstitial connective tissue. Fibronectin and tenascin are also present in the provisional ECM, which is important during development and wound repair [4]. In fibrosis, there is increased expression of elastin, fibronectin and collagens I, III, and IV. This alteration in ECM composition increases the stiffness of lung tissue, consequently decreasing the lungs' ability to exchange gas [141]. In healthy tissue, alveolar compliance has been measured at 1-5 kPa, while fibrotic lung tissue is much stiffer, at 20-100 kPa [142].

Cellular composition of lung tissue also changes significantly during the pathogenesis of fibrosis. Cells found in the lungs include epithelial cells, endothelial cells, interstitial cells, macrophages, fibroblasts, and immune cells among others. These cell types are covered in greater detail in prior reviews [143, 144]. As stated previously, following epithelial injury, inflammatory cells such as macrophages, neutrophils, and T cells migrate to damaged epithelium where they produce a variety of cytokines and chemokines that amplify the inflammatory response. This also triggers fibroblast recruitment, proliferation, and activation of myofibroblasts [145]. Small aggregates of proliferating fibroblasts, myofibroblasts, and immune cells are concentrated in areas known as fibrotic foci. These areas are the sites of excessive ECM production where

scarring disrupts lung architecture and function [25]. Figure 9 demonstrates the effect that fibrotic foci can have on gas exchange function.

The micro-scale structure of alveoli has been analyzed through a variety of imaging methods, including *in vivo* fluorescence microimaging [146], cryosectioning [147], and casting [148]. These measurements converge on alveolar diameter on the order of hundreds of microns and alveolar mouth openings that are 85-90% of the alveolar diameter (Figure 9 and Table 3). Furthermore, many of the gaseous alveolar compartments abut capillaries, enabling gas exchange. In healthy patients, this translates to a fractional tissue volume (mL tissue to mL of total lung) of 0.106-0.191 between inspiration and expiration [149]. However, in fibrotic lungs, the accumulation of tissue increases the fractional tissue volume to 0.220-0.345 [149]. In the diseased state, fibroblast foci generate local alveolar collapse [150], making measurements of individual alveolar geometry difficult. Accurately designed micro-alveolar tissues should approximate these ratios of gas to tissue in order to reflect the altered microenvironment between healthy and diseased states.

Table 3: Selected physical properties of the lung.

| Property | Values in healthy people | Values in IPF patients |
|-------------------------------------------------------------------|---------------------------------------------------------------------------------------------------------------------|---------------------------|
| Compliance | 1-5 kPa [142] | 20-100 kPa [142] |
| Fractional tissue volume (mL tissue per mL tissue and gas) | 0.106 – 0.191 (inspiration - expiration) [149] | 0.220 – 0.345 [149] |
| Alveolar mouth opening | 278 μm [146] | 291.4 μm [151] |
| Alveolar depth to mouth diameter | 0.85-0.9 for residual capacity to total lung capacity. 0.95-1.5 below residual capacity – results in collapse [147] | NA |
| Alveolar half-opening angle | 60 degrees [148, 152] | NA |
| Alveolar lining layer thickness | 0.1-0.2 μm [152, 153] | NA |
| Alveolar diameter | 225 μm [154] | NA |

The use of exogenous biomaterials, such as polymers, can augment mechanical properties [39] or structure [51, 52, 63] of biofabricated models [137]. However, these exogenous materials can disrupt local mechanical properties in often unexpected ways [73], in addition to potential questions of cytotoxicity. Nonetheless, the interplay between exogenous and native biomaterials may produce interesting discoveries and further inform biofabrication of future models.

2.3.3 *Bioprinting techniques*

The choice of biofabrication technique may pose additional constraints on the selection of biomaterials. The technique of 3D bioprinting remains poorly explored in the area of fibrosis assays, but the general field of bioprinting has been reviewed extensively. A recent review of bioinks elaborated on several approaches to print fibroblast-laden hydrogels, however none of these methods were used to evaluate fibrosis [155]. Another review covering 3D bioprinting techniques evaluated bioprinting for creation of complex 3D biomimetic architectures to provide improved *in vitro* analogues to *in vivo* tissue organization [156]. Decellularized ECM bioprinting techniques provide additional promise, as they already include native architecture [157]. These various techniques could be utilized to provide an added level of sophistication to fibrosis assays in order to evaluate a broader range of contributors to fibrosis pathogenesis.

2.4 Conclusions and future directions

Considerable progress has been made in the past two decades to biofabricate complex 3D lung culture environments that recreate aspects of pulmonary fibrosis pathogenesis. These encompass epithelial damage, fibroblast invasion, contraction, and ECM deposition. Furthermore, some of these techniques have been adapted and applied as medium-throughput phenotypic screens for potential therapeutics.

However, there remains unexplored territory, particularly in the areas of alveolar architecture, provisional extracellular matrix and long-term disease progression. These areas present particularly challenging hurdles for cell-based assays. Clotting is a complex process involving many different factors from blood. Incorporation of endothelial compartments or fibrin assays has somewhat addressed the issue. Recent literature implicates aging and fibroblast senescence as key differences between fibrotic and healthy tissue in both animal models [158] and in human patients [159]. The role of senescence in fibrosis has been reviewed recently [29]. Maintaining long-term culture has proven difficult, although multicellular systems have shown some success, including the direct contact epithelial-fibroblast culture that lasted 21 days [66]. Furthermore, we have deliberately neglected the ever-present immune system in this chapter. The exact role of the immune system in IPF remains controversial and the challenges surrounding biofabrication of immune components are immense, but new work in this area could have tremendous benefits.

Development of future phenotypic assays should carefully consider the unique features of the lung environment: mechanical compliance, tissue geometry, and the

composition of cells and matrix proteins. Furthermore, selection of appropriate readouts will be critical to answering the right questions about disease progression. If the assays are to be adapted to high-throughput screens, then extensive optimization of the reproducibility and performance of the assay should be performed. Biofabrication of culture models that enable phenotypic screening of pulmonary fibrosis presents a compelling approach to finding new therapies in pulmonary fibrosis and potentially other related aberrant wound healing diseases.

CHAPTER 3. AQUEOUS TWO-PHASE PRINTING AND FIBRINOLYSIS OF FIBROBLAST-LADEN FIBRIN MICRO- SCAFFOLDS[†]

This chapter describes printing of microscale fibroblast-laden matrices using an aqueous two-phase approach that controls thrombin-mediated enzymatic crosslinking of fibrin. Optimization of aqueous two-phase formulations enabled polymerization of consistent sub-microliter volumes of cell-laden fibrin. When plasminogen was added to these micro-scaffolds, the primary normal human lung fibroblasts converted it to plasmin, triggering gradual degradation of the fibrin. Time-lapse live-cell imaging and automated image analysis provided readouts of time to degradation of 50% of the scaffold as well as maximum degradation rate. The time required for degradation decreased linearly with cell number while it increased in a dose-dependent manner upon addition of TGF- β 1. Fibroblasts isolated from idiopathic pulmonary fibrosis patients showed similar trends with regards to response to TGF- β 1 stimulation. Addition of hydrogen peroxide slowed fibrinolysis but only in the absence of TGF- β 1, consistent with the notion that cellular phenotypes induced by TGF- β 1 are mediated, at least in part, through increased production of hydrogen peroxide. FDA-approved and experimental anti-fibrosis drugs were also tested for their effects on fibrinolysis rates. Given the central role of fibrinolysis in both normal and pathogenic wound healing of various tissues, the high-throughput cell-mediated fibrinolysis assay described has broad applicability in the study of many different cell types

[†] At the time of dissertation submission, this chapter was under review as Robinson, et al. *Aqueous two-phase printing and fibrinolysis of fibroblast-laden fibrin micro-scaffolds*. Biofabrication, xxxx.

and diseases. Furthermore, aqueous two-phase printing of fibrin addresses several current limitations of fibrin bio-inks, indicating additional applications in tissue engineering and *in vitro* models.

3.1 Introduction

Degradation of the provisional fibrin matrix is a key process in wound healing [160]. Following tissue damage, fibrin serves as a temporary scaffold that enables fibroblasts to migrate to the injury site for matrix remodeling [161]. Accelerated fibrin degradation can delay healing by hindering cells' ability to migrate into the wound [3], while suppressed fibrin degradation can promote fibrotic scarring by contributing to excessive collagen accumulation [162, 163]. Properly regulated fibrinolysis is crucial to wound resolution; however, few phenotypic assays are available to evaluate cell-mediated fibrin degradation [164]. Due to the variety of cell-produced proteases and inhibitors as well as biomechanical cellular processes that combinatorially influence fibrinolysis [165], there exists the need for a high-throughput phenotypic assay for cell-mediated fibrin degradation.

Many techniques to evaluate cell-mediated fibrinolysis focus on quantifying mRNA and protein expression for specific components of the fibrinolytic system; however, these approaches are liable to overlook the fibrinolytic contributions of any components that are not specifically evaluated [166-169]. Cell-mediated modulation of the fibrinolytic system occurs predominantly through regulating conversion of the proenzyme plasminogen into the active enzyme plasmin, which degrades fibrin into soluble degradation products. This activation of plasmin is controlled by cellular expression of a variety of proteases and inhibitors, enabling cells to both positively and negatively regulate fibrinolysis [170-174].

Due to this large number of regulators involved in fibrinolysis, experimental approaches that focus on specific contributors to cell-mediated fibrin degradation are liable to overlook unexpected changes to the fibrinolytic system.

Here, we analyze human lung fibroblast-mediated fibrinolysis with a focus on idiopathic pulmonary fibrosis (IPF), a disorder of unknown etiology where repeated small injuries have been suggested to play a role. This chronic fibroproliferative disease presents as an exaggerated aging process; where epigenetics, senescence, and biomechanics have all been proposed as potential contributing factors [27]. The progression of IPF results in a continued decline in lung capacity that ultimately leads to respiratory failure [25]. A growing body of evidence indicates that dysregulation of the fibrinolytic system may be a contributor to IPF pathogenesis [175-177]. Current FDA-approved drugs for IPF are incapable of halting or reversing fibrosis, and can only slow the spread of fibrotic scarring throughout the lungs [26]. A high-throughput phenotypic assay for fibrinolysis may contribute to efforts to find therapeutic compounds.

There are currently few phenotypic approaches to evaluate fibrinolysis. One implementation of cell-laden fibrin gels was able to differentiate between fibrinolytic stimuli and cell source tissue by comparing relative amounts of degraded matrix between conditions [164]. Importantly, this approach implemented a fibrin hydrogel, which enabled the biophysical feedback of matrix interactions to contribute to fibrin remodeling [178, 179]. However, this fibrinolysis assay faces limitations due to its large volume format. A high-throughput adaptation of this fibrin-based fibrinolysis assay would require establishing a microplate-compatible technique to generate the cell-laden fibrin scaffolds. This poses an engineering hurdle due to difficulties controlling thrombin-mediated

crosslinking for low volume fibrin structures [180]. No prior methods to fabricate microscale fibrin scaffolds were suitable for this high-throughput assay.

To consistently print microscale cell-laden fibrin scaffolds with standard liquid handling equipment, this work details a new approach that controls crosslinking during the polymerization process by introducing fibrinogen and thrombin within separate aqueous phases. We utilize an aqueous two-phase system (ATPS), in which soluble polymers thermodynamically drive aqueous systems to form two distinct phases. Our research group has previously developed ATPS assays to evaluate collagen contraction with living cells [58]. Here, the optimization of a PEG/dextran ATPS enables successful polymerization of sub-microliter volumes of cell-laden fibrin scaffolds. These microgels can be directly degraded through addition of plasmin, or fibrinolysis can occur through cell-mediated activation of exogenous plasminogen. Fibrinolysis rates vary in response to pro-fibrotic stimuli and anti-fibrotic therapeutics, as determined through label-free brightfield microscopy. We demonstrate our fibrin-printing technology as a simple, versatile, and easily managed approach to fabricate precise microscale scaffolds, and this technology was applied for high-throughput evaluation of cell-mediated fibrinolysis.

3.2 Materials and Methods

3.2.1 Cell culture and ATPS reagents

A stock solution of DEX (20% w/w dextran T500; Sigma) was prepared in phosphate buffered saline (PBS) on a rocker overnight. A stock solution of PEG (6% w/w, 35k MW; Sigma) was prepared in fully supplemented culture media with 10% deionized water to balance osmolality. Both stock solutions were passed through a 0.22 μm sterilizing

syringe filter before storage. PEG working solutions were stored for up to 2 weeks at 4C. Thrombin (Human Alpha Thrombin; Enzyme Research Labs) was also added to the PEG solution at a concentration of 0.1 U/mL immediately preceding experiments. Fibrinogen-DEX solutions were prepared by diluting fibrinogen stock solution (human fibrinogen 3; Enzyme Research Labs) to a final concentration of 4 mg/mL in a sterile solution of 4% 10x DMEM, 15% DEX stock solution (to a final concentration of 3% dextran), and 50% cell suspension in growth media. For all experiments excluding cell concentration evaluation, the cell suspension was diluted for 1000 cells per microliter in the final fibrinogen-DEX solution.

3.2.2 Cell preparation

Normal human lung fibroblasts (NHLF lot#0000580583; Lonza) from a 79 year old female with a history of smoking, and idiopathic pulmonary fibrosis fibroblasts (IPF lot#0000627840; Lonza) from a 52 year old male were cultured in fibroblast growth media (FGM; Lonza). Cells were passaged at 80-90% confluence, and were sub-cultured in 1:3 ratios by trypsinization. When at the desired confluence, cells were washed with PBS and 0.05% trypsin solution was added to the flask. Cells were incubated for 2 min, diluted with fibroblast growth media media, and then harvested and centrifuged (200 x g, 5min) in a conical tube. The supernatant was aspirated and the cell pellet was re-suspended in serum-free culture media. When used in fibrin degradation experiments, cells were re-suspended at 2x the final desired concentration (1000 cells/ μ l unless otherwise indicated). All experiments were conducted with cells at or below passage 12. In all experiments, media was changed every 48 hours and any media additives (plasminogen, TGF- β 1, drugs, etc.) were included.

3.2.3 *ATPS printing of fibrin microgels*

Working solutions of PEG with 0.1 U/mL of thrombin were warmed to 37C and pipetted into a 96-well plate. For production of droplets, fibrinogen-DEX solutions with cell suspension were maintained at 37C and pipetted directly into the PEG-thrombin media using either a manual pipette or a semi-automated 96-channel pipette (Viaflo-96; Integra). All assays utilized a volume of 1 μ l unless otherwise noted. Following dispensing of the DEX phase, the plates were placed in an incubator at 37C for 30 min to allow the thrombin to enzymatically crosslink the fibrinogen into a fibrin matrix (Figure 10A). The PEG-enriched media was then washed four times by removing, then replacing half of the media with PEG-free media. When applicable, the final media addition was supplemented with stimuli as detailed in section 2.5. For the duration of each experiment, assay plates were imaged every 2 hours at 4x with an automated cell culture monitoring system (Incucyte S3; Essen Biosystems). After one day of culture, plasminogen (50 μ g/mL) (Human Glu-Plasminogen; Enzyme Research Labs) was added as a 10x concentrated solution to each well in order to initiate assay degradation (Figure 10B), unless otherwise noted for specific conditions. Fresh plasminogen was included with each subsequent media addition. Positive controls with active plasmin (1 U/ml) (Human Plasmin; Enzyme Research Labs) and negative controls without plasminogen were included in each experiment. As cells activated plasminogen, the fibrin scaffold progressively degraded as illustrated in Figure 10C.

3.2.4 *High-throughput brightfield image analysis*

After each experiment, brightfield images for every time point were downloaded in jpeg format from the automated cell culture monitoring system. Python's OpenCV library was implemented for the masking approach illustrated in Figure 11A. First, a threshold was set at 50% of the maximum intensity (128 for 8-bit integer pixel values) in order to isolate the darker pixels of semi-opaque fibrin hydrogel from the background of the image. A closing morphological filter with a 25x25 kernel was then applied to each mask in order to remove noise. This masking approach was applied to the initial time point from every experimental condition in order to establish the relevant assay area for downstream measurements. As fibrin degrades during an experiment, the average pixel intensity within the masked area increases accordingly (Figure 11B). The automated live-cell imager (Incucyte S3; Essen Biosystems) automatically adjusts brightness to maintain consistent white balance between images. For experiments involving multiple assay volumes, image brightness was scaled to maintain consistent background intensity (Appendix Figure A-1).

For each experimental replicate, a sigmoid curve was fit using the `curve_fit` function from the SciPy library in Python. The logistic function given by the equation in Figure 11C enabled automated extraction of the time point for 50% degradation, as well as the maximum slope at the equation's centroid (Figure 11 D, E).

3.2.5 *Phenotypic evaluation of stimuli*

In order to evaluate fibrin degradation rate with a known anti-fibrinolytic stimulus, various concentrations of transforming growth factor type β 1 (Human Recombinant TGF-

β 1; Peprotech) were added to the assay media after ATPS polymers were rinsed out of the microplates.

To evaluate the capability of this assay to test the fibrinolytic effects of therapeutic stimuli, a variety of drug compounds were introduced to the fibrinolysis assays after the wash step. This included 40 μ M pirfenidone (Selleck Chem), 0.4 μ M nintedanib (Selleck Chem), 100 μ M hydrogen peroxide (Sigma), and 20 μ M diethyl-pythiDC (AOBIOUS). These concentrations were established in preliminary experiments that evaluated a range of concentrations used in prior literature. Stimuli were freshly mixed for each media change during experiments, and a minimum of four replicates were tested per experimental condition.

3.2.6 *Statistical Analysis*

All experimental values are reported as means \pm standard deviation. ANOVA tests were performed using the statsmodels library in Python 3 with the Tukey test for post-hoc pairwise comparisons.

3.3 **Results and Discussion**

The development and characterization of the cell-mediated fibrinolysis assay was focused on establishing a microplate-compatible fibroblast-laden fibrin scaffold and verifying the ability to distinguish between subtly different fibrinolytic environments. First, we implemented an ATPS approach to enable accurate printing of unprecedentedly small cell-laden fibrin scaffolds. Then, an automated image processing approach quantified fibrin degradation data from label-free brightfield images. Next, the established fibrinolytic

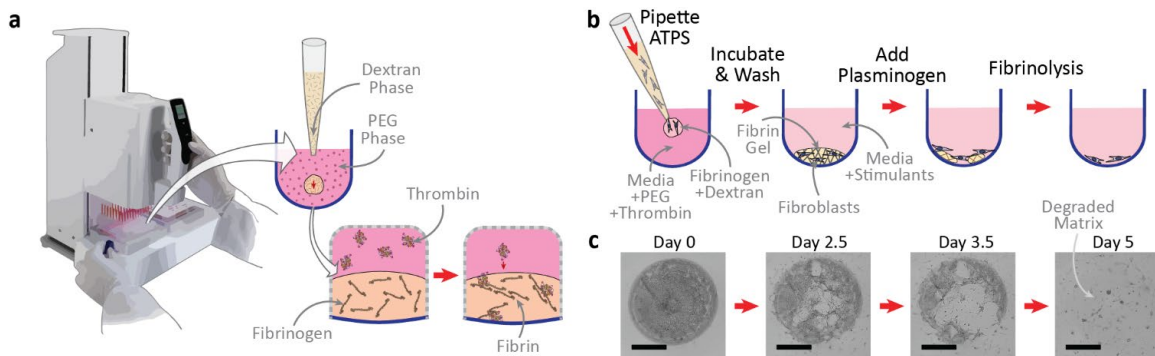


Figure 10. ATPS fibrin printing and cell-mediated degradation: (a) Illustration of the enzymatic control enabled by ATPS printing of fibrin scaffolds, whereby thrombin from the PEG phase diffuses into the dextran phase and crosslinks the fibrinogen into fibrin during the incubation period. (b) Process schematic of ATPS generation of microscale fibrin droplets and subsequent fibrinolysis. (c) Characteristic brightfield microscope images (taken at 4x magnification) illustrate the assay progression when stimulated with 0.5 ng/mL of TGF- β 1, showing an opaque fibrin matrix and progressive degradation. Scale bars are 1 mm.

effects of cell density and TGF- β 1 were used to validate the assay's capability to distinguish between conditions. Finally, the microscale cell mediated fibrinolysis assay was implemented to evaluate the effects of anti-fibrotic therapeutics on fibroblasts from normal and diseased donors.

3.3.1 Fabrication of microscale fibrin scaffolds

Biological environments establish fibrin matrices through coagulation, where a cascade of clotting factors activates thrombin, which enzymatically crosslinks fibrinogen into fibrin [161]. Similarly, *in vitro* fibrin scaffolds rely on exposing monomeric fibrinogen to thrombin [181]. Fibrin has been used extensively in a wide variety of tissue engineering applications, but it is generally implemented as a bulk cast hydrogel. There have been a few applications of fibrin bio-printing that control crosslinking by alternating between layers of fibrinogen and thrombin, but this poses limitations to accuracy and reproducibility due to lack of control over fibrinogen's exposure to thrombin [181-183]. There have also

been a variety of applications for fibrin microbeads where oil immersions were used to disperse microbeads during crosslinking in oil-suspended droplets, but this results in inconsistent size and cells must be added separately after the microbeads have been washed [184, 185]. Reliable microscale volume and microplate compatibility were necessary to enable high-throughput adaptation in this assay. Precise control over cell seeding density was also vital for our approach due to its effect on remodeling rate.

We established a new approach to maintain fibrinogen in a distinct droplet and control diffusion of thrombin into fibrinogen during the polymerization process by implementing an ATPS with PEG and dextran. Above their critical concentrations, these soluble polymers thermo-dynamically drive aqueous systems to form two distinct phases [186]. A previous ATPS microscale adaptation from our lab for collagen contraction demonstrated consistency in response between the conventional 100 μ L assay and ATPS microscale volumes. They specifically took advantage of the short length scales for time-dependent and burst stimulation profiles, which would not be possible with conventional approaches due to diffusion constraints [58]. A similar ATPS adaptation suits our approach, and enables fabrication of microscale fibrin scaffolds with standard liquid handling equipment to facilitate microplate compatibility.

During the initial optimization of PEG and dextran concentrations, we found that lower concentrations were unstable and resulted in fissure of the ATPS droplet. In order to maintain stable separation of phases during polymerization, minimum assay concentrations of 6% 35 kDa PEG and 3% T500 dextran were determined for stability during crosslinking (Figure 10A). Fibroblast viability has previously been verified at these ATPS concentrations in a prior microscale assay adaptation [58].

The necessity for this ATPS environment in our microscale fibrin degradation assay comes from the capability of aqueous two-phase partitioning to control diffusion of thrombin into the fibrinogen droplet. This restricts enzymatic crosslinking of cell-laden fibrin matrices until after the droplets have been dispensed (Figure 10A). After a 30 minute incubation period, the fibrin was sufficiently polymerized and the ATPS solutions could be rinsed and replaced with growth media and stimulants for specific conditions (Figure 10B). We waited an additional period of 24 hours before adding exogenous plasminogen to enable cells to anchor themselves to the fibrin matrix.

After plasminogen is added to the assays, various activators and inhibitors produced by cells regulate the conversion of plasminogen into plasmin [170-174]. Control conditions for each experiment verified rapid matrix degradation with the addition of exogenous plasmin and no matrix degradation when plasminogen is omitted (Supplemental Video 1). As the assay proceeds, the fibrin matrix gradually degrades with activated plasmin cleaving fibrin into soluble fibrin degradation products (Figure 10C). This is visually evident as disappearance of the opaque fibrin matrix. The following section is focused on implementing an image processing and analysis approach in order to automate quantification of differences in fibrin degradation between conditions.

3.3.2 Label-free quantification of fibrin degradation

In the context of wound healing and fibrosis, evaluation of cell-mediated fibrinolysis generally implements quantitative assays to measure specific mRNAs and proteins involved in plasmin activation [166-169]. This evaluation is generally limited to the proteases that cleave plasminogen into activated plasmin and the inhibitors of these

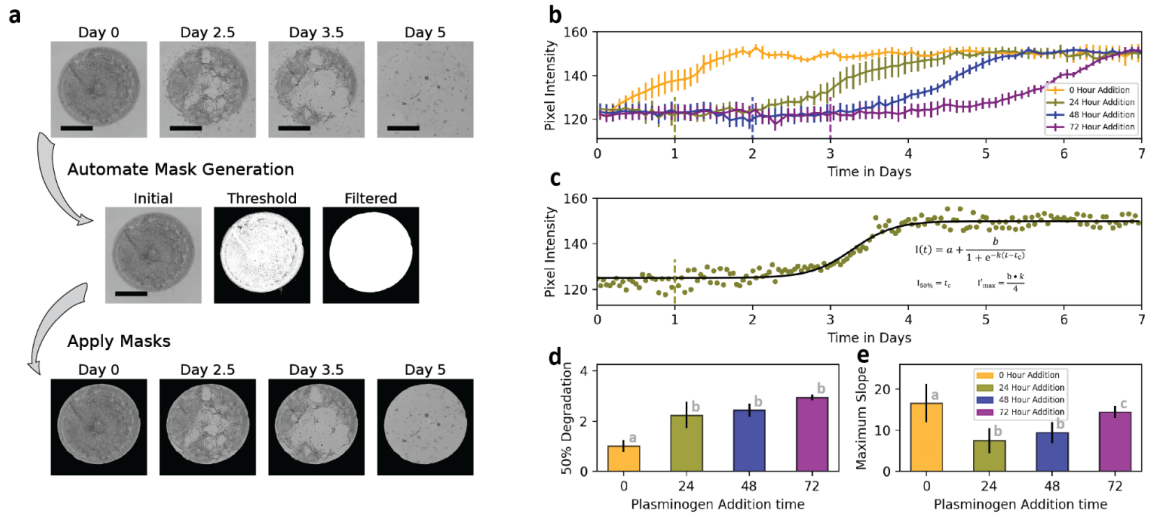


Figure 11. High-throughput quantification of fibrin degradation: (a) Automated image processing and analysis utilized Python’s OpenCV library for thresholding and morphological filtering in order to establish an initial mask for each individual assay that was applied to all assay images for that well. Scale bars are 1 mm. (b) The average pixel intensity within masked regions was plotted for time course evaluation, as illustrated here with different plasminogen addition times, where dotted lines indicate the plasminogen addition time and error bars represent the standard deviation between experimental replicates. (c) An example measurement demonstrates image metric extraction by fitting a logistic function to time course pixel intensity data with least squares regression. The time point for 50% degradation (d) and maximum slope from the sigmoid centroid (e) were determined using logistic functions fit for each experimental replicate. Note that the 50% degradation time (vertical axis) is indicated here as days after plasminogen addition, while the plasminogen addition time (horizontal axis) is in hours. (Statistical significance for (d, e) $P < 0.01$ by ANOVA. $ab = P < 0.01$; $bc = P < 0.05$; $ac = P < 0.1$ by post-hoc Tukey test. $N = 5$ for all conditions)

proteases; however, a variety of other enzymes and inhibitors, which are often overlooked, are also involved in regulation of cell-mediated fibrinolysis [172, 173]. Here, label-free evaluation of live-cell images enables quantification of fibrin degradation.

Due to the relative opacity of our fibrin scaffolds, pixels within the assay area are significantly darker than those in the background of microscope images. This enables an analysis approach based on pixel intensities within the assay area. Many established hemostasis assays take advantage of fibrin’s attenuation of light for quantification. These assays generally implement plate readers to measure absorbance during coagulation and

fibrinolysis [187, 188]. Evaluation of this assay in a microplate reader may therefore serve as an alternative to brightfield analysis. However, our approach favored evaluation of pixel intensity from brightfield images so that the micrographs could serve as validation of assay progression. Unfortunately, the commercial image analysis package embedded in our live cell imaging system was not able to reliably discern the microprinted fibrin scaffold. We therefore developed an alternative image analysis pipeline using Python's OpenCV library.

In order to isolate the assay area from background, a thresholding approach was sufficient because of the significant difference in pixel brightness. Here, any pixels brighter than the specified threshold were classified as background. A closing morphological filter was applied to the thresholded images to remove noise left by the thresholding process. Figure 11A demonstrates mask generation and its implementation at later time points as the fibrin matrix degrades. After isolation of the assay area, average pixel intensity within masked regions was plotted in order to visualize time-course fibrin degradation (Figure 11B). Fitting time-course data from each individual well with a sigmoidal curve facilitated extraction of the time point for 50% matrix degradation, as well as the maximum slope at the sigmoid's centroid (Figure 11C).

Figure 11D shows changes in the 50% degradation time point in response to different plasminogen addition times. The 50% degradation time point is shown as days since plasminogen addition. Increases in bar height indicate slower cell-mediated fibrinolysis. ANOVA indicated statistical significance of these differences in degradation time ($P < 0.01$), and post-hoc pairwise analysis with the Tukey test demonstrated statistically significant differences between specific conditions (Figure 11D). The increase in time to 50% degradation for later plasminogen additions indicates significant changes

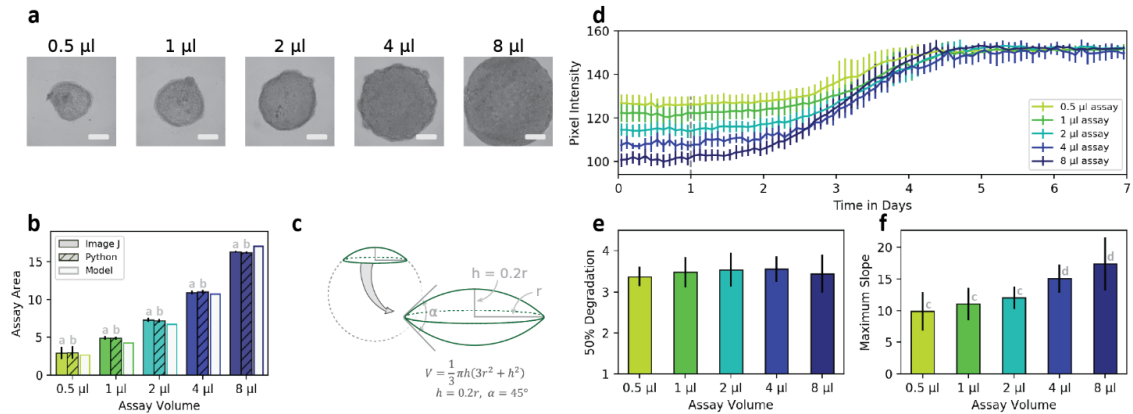


Figure 12. Assay volume consistency: (a) ATPS printing of fibrin scaffolds demonstrated consistency in assay shape and texture between volumes. Scale bars are 1 mm. (b) Cross sectional area of assays was compared between image J, Python generated masks, and a geometric model of assay volume. (c) A doubled spherical cap demonstrated the best fit of the geometric volume models evaluated (including sphere, hemisphere, and single spherical cap). (d) Time course data shows changes in average pixel intensity for different assay volumes to demonstrate consistency in fibrin degradation time between volume conditions. Different initial pixel intensity values between conditions indicate varied transmission of light through different volume constructs. The 50% degradation time (e) and maximum slope (f) further demonstrate these trends. (Statistical significance for (b, f) $P < 0.01$ by ANOVA. $ab = P > 0.2$; $cd = P < 0.05$ by post-hoc Tukey test. $N = 4$ for all conditions)

in the scaffold or cells in the first 24 hours. It has previously been demonstrated that cell-matrix interactions influence the rate of fibroblast-mediated fibrinolysis, so additional time before plasminogen addition may have influenced rates observed here through similar pathways [179]. Hence, it was important in subsequent studies to evaluate cell-mediated fibrin degradation with a consistent plasminogen addition time. A plasminogen addition time at 24 hours was implemented so that fibroblasts could initiate cell-matrix interactions.

The effects of assay volume were also evaluated. Assay volumes between 0.5 μl and 8 μl could be consistently printed and viewed within the field-of-view of a 4x microscope objective (Figure 12A). The Python-based image masking approach was compared against a manual approach that outlined the assay area in image J with no significant differences in cross sectional area between techniques (Figure 12B). Cross

sectional area was also compared to volume through evaluation of geometric models. Compared against spheres, hemispheres, and spherical caps; a doubled spherical cap fit the volume and area data most closely as determined through least squares regression (Figure 12C).

In our prior microscale adaptation of collagen contraction, we found that different assay volumes maintained consistent contraction rates as long as cell density was maintained [58]. Fibrinolysis trends in our experiments also depend on cell density rather than assay volume. While the pixel intensity of higher volume assays had lower starting values, this reflected the presence of more fibrin which resulted in decreased transmission of light through those assays (Figure 12D). Time points for 50% degradation, as determined by a sigmoid fit, showed no significant difference in degradation timing between different volume conditions (Figure 12E). This consistency in degradation timing indicates similar rates of cell-mediated fibrinolysis between different volume conditions. Differences in maximum slope between conditions followed the same trend as differences in initial pixel intensity, resulting from the decreased transmitted light through higher volume fibrin scaffolds.

The consistency in degradation rates between volume conditions indicates uniformity in fibrin organization. Fibrin network morphology has a significant impact on fibrinolysis rate, where tight fibrin conformations degrade at a slower rate than scaffolds with looser fibrin conformations and thicker fibers [189]. This suggests that at the concentration of thrombin used in our assays, ATPS-mediated control over the diffusion of thrombin into the fibrinogen-containing phase results in consistent fibrin organization across the range of assay volumes tested.

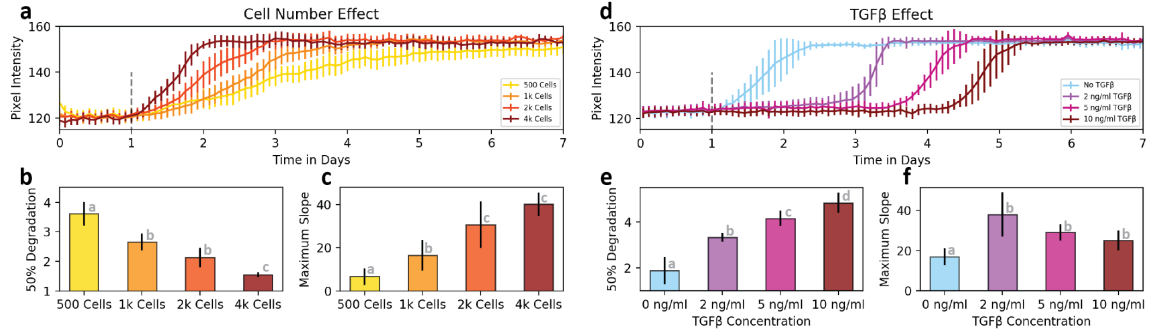


Figure 13. Cell density and TGF-β1 effects: (a) Time course pixel intensity data demonstrates changes in fibrin degradation between different densities of cells within a 1 μl assay. The 50% degradation time (b) and maximum slope (c) demonstrate decreased fibrinolysis time and increased slope with higher cell counts. (d) Pixel intensity data for various concentrations of TGF-β1 indicates delays in fibrin degradation in response to the stimulus. The 50% degradation time (e) and maximum slope (f) show increases in fibrinolysis time but no significant changes in slope with higher concentrations of TGF-β1. (Statistical significance $P < 0.01$ by ANOVA. In (b, c, e, f) $P < 0.05$ by post-hoc Tukey test between all bars with different lettered labels. $N = 4$ for all conditions)

3.3.3 Effects of cell seeding density and TGF-β1

Cell seeding density was also evaluated. Conditions with higher seeding densities demonstrated significantly faster fibrinolysis (Figure 13), with decreased time points for 50% degradation and increased maximum slope (Figure 13 B, C; $P < 0.05$ for all pairwise comparisons). The linear relationship between rate of fibrinolysis and cell number is consistent with a cell-mediated step being rate limiting in this process. This also highlights the importance of consistent cell-seeding density in fibrin printing applications. Our ATPS printing technique is uniquely capable of establishing microscale cell-laden fibrin scaffolds with a consistent seeding density [181, 185].

TGF-β1 is an established pro-fibrotic stimulus with well-characterized anti-fibrinolytic effects [190]. Various concentrations of TGF-β1 were used to stimulate NHLF cells in the fibrin assays (Figure 13D). Increasing concentrations resulted in longer time delays before fibrinolysis. The time points for 50% degradation further demonstrate this

trend (Figure 13E). All pairwise differences in 50% degradation time between conditions were significant with $P < 0.05$ (Figure 13F). Interestingly, these differences in fibrinolysis profile appear as a delay before initiation of fibrin degradation. Prior studies have linked elevated PAI-1 with delayed fibrinolysis [191], although additional evaluation is necessary to determine its relative contribution to the changes in fibrinolysis rate associated with TGF- β 1 stimulation [192].

In NHLF cells, we also noticed an effect of cell passage number on fibrinolysis (Appendix Figure A-2a). Higher passage numbers exhibited progressively longer 50% degradation times with slower fibrin degradation rates (Appendix Figure A-2b). These incidental observations are consistent with prior studies that demonstrate that PAI-1 is upregulated in senescent fibroblasts *in vivo* and *in vitro* [193-195].

3.3.4 Evaluation of hydrogen peroxide, therapeutics and IPF fibroblasts

Having established baseline cell response measurements for fibrinolysis of the bioprinted fibrin micro-scaffolds, we next compared fibrinolytic profiles between normal and diseased lung fibroblasts with a number of stimulants and inhibitors. Hydrogen peroxide is a reactive oxygen species (ROS) known to be produced by cells in response to TGF- β 1 stimulation, while nintedanib and pirfenidone are the only two FDA-approved therapies for IPF. Diethyl-pythiDC, an experimental anti-fibrotic drug, is an inhibitor of certain prolyl 4-hydroxylases that play a role in post-translational modification of collagen and other proteins [196]. The plasmin control condition was included in graphs for

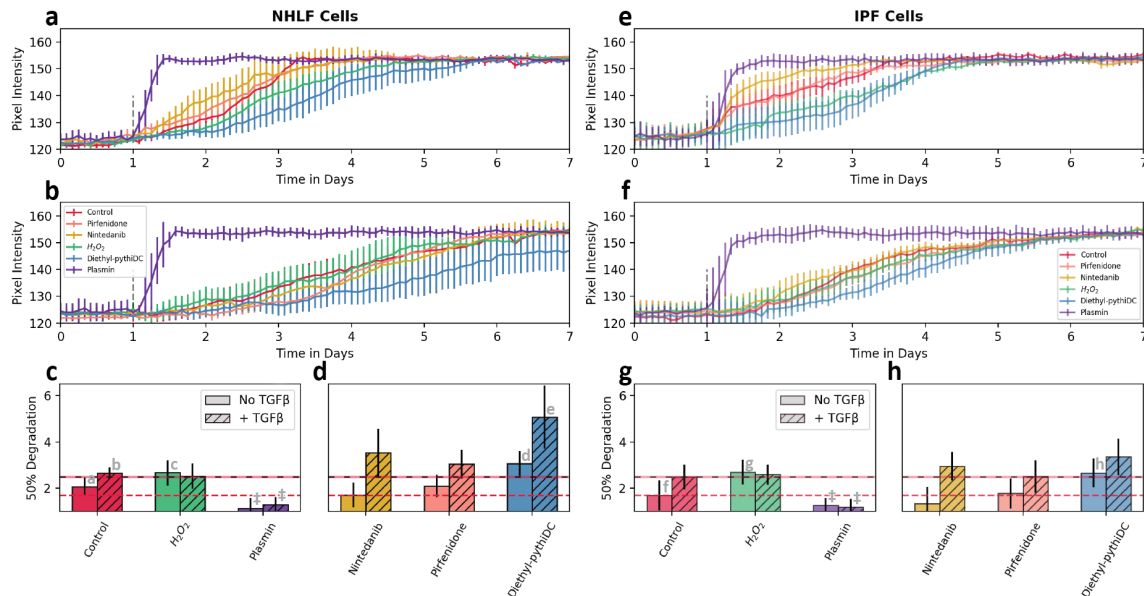


Figure 14. Cell donor and drug stimulation: Time-course pixel intensity data show the effects on fibrin degradation of several different stimulants, with NHLF cells on the left and diseased IPF cells on the right. The upper pixel intensity graphs have no TGF- β 1 (a and e) while the lower graphs contain 2 ng/ml TGF- β 1 (b and f). Sigmoid fits were used to determine 50% degradation time (c, d, g and h) from the above pixel intensity graphs. (Statistical significance $P < 0.01$ independently for drug and TGF- β 1 stimulus by two-way ANOVA: As the positive control, plasmin was excluded from ANOVA. ‡ = $P < 0.01$; ad, be = $P < 0.05$; ac, fg, fh = $P < 0.1$ by post-hoc Tukey test. $N = 4$ for all conditions)

reference, but was excluded from statistical analysis in the interest of focusing on therapeutic conditions of interest.

A general comparison between normal and diseased fibroblasts (Figure 14 A-H) demonstrates that cells from the IPF donor consistently degraded fibrin significantly faster than the normal fibroblasts ($P < 0.01$ by two-way ANOVA). However, prior research indicates that diseased fibroblasts from IPF donors express elevated levels of PAI-1 and should consequently exhibit slower fibrin degradation [10]. This unexpected decrease in fibrinolysis time in IPF fibroblasts may be due to the cells' extended removal from the diseased microenvironment. In the diseased lung, overactive epithelial cells secrete several growth factors, cytokines, and chemokines involved in migration, proliferation, and

activation of fibroblasts [197]. Additionally, the donor for these NHLF cells does not fit the typical profile for healthy lung tissue. This particular donor was a 79 year old female with a history of smoking. Age related cellular senescence and tobacco use have both been associated with increased levels of PAI-1, so the fibrinolytic system in these “normal” fibroblasts may be dysregulated compared to a younger non-smoking donor [198].

Stimulation with hydrogen peroxide alone demonstrated highly significant decreases in the rates of fibrinolysis ($P < 0.1$) suggesting a critical role of ROS in the process of cell-mediated fibrinolysis. In contrast, conditions that included TGF- β 1 showed no significant difference upon further stimulation with exogenous hydrogen peroxide. This non-additive effect is consistent with a notion that the effects of adding exogenous H₂O₂ and exogenous TGF- β 1 converge [199]. That is, TGF- β 1-triggered increase in endogenous H₂O₂ production [200, 201], may mask effects of any exogenous H₂O₂ addition. Such effects may also work in concert with ROS-induced reduction in TGF- β 1 receptors [43].

The two FDA-approved IPF drugs, nintedanib and pirfenidone, did not show a significant impact on fibrinolysis. These therapeutics have established anti-fibrotic effects, so these results indicate that the mechanism of action for nintedanib and pirfenidone may not be related to fibrinolytic activity of lung fibroblasts. As the precise mechanisms of action of these FDA-approved drugs are not known, the “negative” results of these drugs on fibroblast-mediated fibrinolysis is in and of itself of intellectual value. The experimental drug diethyl-pythiDC, on the other hand, significantly ($P < 0.05$) delayed fibrinolysis. Diethyl-pythiDC is a selective inhibitor of prolyl 4-hydroxylase, an enzyme best known for structure-stabilizing modifications of collagen [196] that also acts on a variety of proteins [202] including hypoxia inducible factor 1 [199, 203]. The ability of diethyl-

PythiDC to reduce fibroblast-mediated fibrinolysis is also a novel finding and demonstrates the utility of our assay.

While our assay is effective for finding molecules that modulate cell-mediated fibrinolysis, the lack of a significant effect with established IPF therapeutics does reveal limitations of using this assay for testing anti-fibrotic drugs. Although fibrinolytic proteases are known to play a significant role in IPF progression, their effects can be through non-fibrinolytic effects that our assay would miss, such as activation of protease activated receptors (PARs) [204]. Nintedanib and pirfenidone are also reported to exert anti-fibrotic effects through direct binding to collagen fibrils to inhibit their assembly [205], another mechanism of action our assay would miss.

3.4 Conclusions

This work describes an approach for ATPS-based printing of microscale cell-laden fibrin scaffolds. A droplet comprised of the heavier phase partitions cells and fibrinogen while the bulk phase provides thrombin to promote localized enzymatic crosslinking, leading to controlled production of microliter-scale fibrin constructs. Automated label-free image processing quantified rates of cell-mediated fibrin degradation from time-course brightfield images. We found that primary human lung fibroblasts degrade the fibrin scaffold at a rate dependent on source of cells, cell density, and the presence of soluble factors. Given the variety of contributors to dysregulation of fibrinolysis seen in cancer, fibrosis, and metabolic disease; this phenotypic assay for cell-mediated fibrin degradation provides a potentially valuable research tool for further studies in these and other fields. Additionally, the technique developed here for aqueous two-phase printing of cell-laden

fibrin can be much more broadly applied in bio-printing and tissue engineering applications.

CHAPTER 4. LUNG SCARRING-IN-A-WELL[‡]

Tissue damage often triggers rapid clotting followed by a slower, cell-mediated repair process of clot dissolution, deposition of new extracellular matrix, and contracture. This paper recreates key steps in this tissue repair process in 96-well plates using primary human lung fibroblasts and microscale fibrin clots. These cell-laden gels are formed by aqueous two-phase micro-printing, and the cell-mediated matrix remodeling is monitored by time-lapse microscopy and automated image processing. Stimulation of this wound healing model with the pro-fibrotic cytokine TGF- β 1 leads to an excessive scar formation response that manifests as a combination of slowed fibrinolysis and increased collagen production. Addition of drugs also shifted the scarring profile: the two FDA-approved fibrosis drugs (nintedanib and pirfenidone) and a collagen cross-linking inhibitor DiethylpythiDC reduced collagen deposition while a PAI-1 inhibitor, TM5275, and an autotaxin inhibitor, GLPG1690, reduced both collagen production and fibrinolysis time. An NMDA inhibitor, NP-120 also known as Ifenprodil, slightly increased collagen levels while a protease inhibitor, aprotinin, drastically delayed fibrinolysis and also increased collagen deposition. Not only is the assay useful for functional differentiation of drug action, it is highly sensitive; one of the few *in vitro* assays that can clearly detect Pirfenidone effects at physiological concentrations. Although this paper focuses on lung fibrosis, the approach opens new opportunities for studying a broad range of fibrotic diseases and for evaluating anti-fibrotic therapeutics.

[‡] At the time of dissertation submission, this chapter was under preparation for submission

4.1 Introduction

Fibrin degradation and collagen deposition are central to the wound healing process [206, 207]. The provisional fibrin matrix is formed by coagulation following initial injury and provides a temporary scaffold for tissue repair. Because fibrin lacks the organization of native interstitial extracellular matrix (ECM) it is gradually replaced through processes including cell-mediated fibrin degradation and collagen deposition [170, 208]. Dysregulation of this matrix turnover can result in pathological conditions such as fibroproliferative disease from chronic excessive collagen deposition [8, 209]. This dysregulation can result from multiple contributing pathways; however, there are currently no *in vitro* assays to evaluate multifactorial contributions to fibrin remodeling. Due to the variety of cytokines, proteases, inhibitors, and biomechanical factors that combinatorially influence remodeling [125, 175, 178, 210], a high-throughput phenotypic assay would be well suited to evaluate cell-mediated fibrin remodeling for applications in wound healing and fibrosis.

Idiopathic pulmonary fibrosis (IPF) is a chronic progressive disorder of aberrant ECM accumulation in the lungs. Current FDA-approved drugs for IPF can only slow, not halt or reverse, disease progression [211-213]; but several recent reviews have proposed regulators of fibrinolysis as potential targets for future IPF treatment strategies [214-216]. Evidence indicates that IPF progression is driven in part by a hypercoagulable and anti-fibrinolytic environment, where fibrin forms in the absence of exogenous tissue damage and degrades more slowly than the healthy physiological rate [26, 217]. However, specific mechanisms linking fibrin persistence to tissue fibrosis remain unclear. Different theories suggest that downstream signaling of the fibrinolytic system, mechanical persistence of the

fibrin scaffold, or biophysical feedback between cells and ECM may contribute to this pathological fibrin remodeling in fibroblasts [178, 179, 218-220].

Our lab recently established a technique to print unprecedentedly small cell-laden fibrin matrices by implementing aqueous two-phase systems (ATPS). ATPS printing enabled separation of fibrinogen and thrombin in two distinct immiscible aqueous phases so that thrombin must diffuse between phases before crosslinking. This method for ATPS fibrin micro-printing was previously implemented to establish an assay for cell-mediated fibrinolysis. The conditions in this prior study, however, did not provide readouts of fibrotic processes such as collagen deposition, which typically accompanies fibrinolysis in wound healing and scarring.

In this work, we adapt our prior ATPS fibrin micro-printing technique to enable high-throughput label-free analysis of scarring. This adaptation built upon our finding that a more physiological higher seeding density, and use of serum, promoted fibroblast differentiation and collagen deposition in addition to fibrin degradation. The fibrin microgels were then stimulated with pro-fibrotic cytokines to evaluate mRNA expression and ECM deposition. Multiple donors for normal and diseased lung fibroblasts were utilized in order to evaluate consistency in response to therapeutic stimuli and investigate the interplay between fibrinolysis and collagen deposition at physiologically relevant concentrations of these compounds. To our knowledge, this is the first *in vitro* assay to conveniently combine label-free readouts for fibrin degradation, collagen synthesis, and cell contraction to evaluate fibrotic tissue remodeling.

4.2 Materials and Methods:

4.2.1 Cell culture and ATPS reagents

A stock solution of DEX (20% w/w dextran T500; Sigma) was prepared in PBS on a rocker overnight. A stock solution of PEG (6% w/w, 35k MW; Sigma) was prepared in fully supplemented culture media with 10% deionized water to balance osmolality. Both stock solutions were passed through a 0.22 μ m sterilizing syringe filter before storage. PEG working solutions were stored for up to 2 weeks at 4C. Thrombin (Human Alpha Thrombin; Enzyme Research Labs) was also added to the PEG solution at a concentration of 0.1 U/mL immediately preceding experiments. Fibrinogen-DEX solutions were prepared by diluting fibrinogen stock solution (human fibrinogen 3; Enzyme Research Labs) to a final concentration of 4 mg/mL in a sterile solution of 4% 10x DMEM, 15% DEX stock solution (to a final concentration of 3% dextran), and 50% cell suspension in growth media. For all experiments, the cell suspension was diluted for 2500 cells per microliter in the final fibrinogen-DEX solution.

4.2.2 Cell preparation

Human primary lung fibroblasts were used in all experiments presented in this chapter. Unless otherwise noted, experiments utilized normal human lung fibroblasts (NHLF B lot#0000580583; Lonza) from a 79 year old female with a history of smoking. For experiments evaluating donor variability, the following cells were utilized: NHLF A (NHLF lot#0000608197; Lonza) from a 67 year old male, IPF A (IPF lot#0000627840; Lonza) from a 52 year old male, and IPF B (IPF lot#6F5002; Lonza) from a 83 year old male. All cells were cultured in fibroblast growth media (FGM; Lonza). Cells were

passaged at 80-90% confluence, and were sub-cultured in 1:3 ratios by trypsinization. When at the desired confluence, cells were washed with PBS and 0.05% trypsin solution was added to the flask. Cells were incubated for 2 min, and then harvested and centrifuged (200 xg, 5min) in a conical tube. The supernatant was aspirated and the cell pellet was re-suspended in serum-free culture media. When used in fibrin degradation experiments, cells were re-suspended at 2x the final desired concentration (2500 cells/ μ l unless otherwise indicated). All experiments were conducted with cells at or below passage 8 except for high passage experiments conducted at passage 12. In all experiments, media was changed every 48 hours and any media additives (plasminogen, TGF- β 1, drugs, etc) were included.

4.2.3 ATPS printing of fibrin microgels

ATPS printing of fibrin micro-scaffolds was previously documented in Chapter 2. Briefly, working solutions of PEG with 0.1 U/mL of thrombin were warmed to 37C and pipetted into a 96-well plate. For production of droplets, fibrinogen-DEX solutions with cell suspension were maintained at 37C and 4 μ l per assay (unless otherwise noted) was pipetted directly into the PEG-thrombin media using a semi-automated repeater pipette (Repeater E3X; Eppendorf). Following dispensing of the DEX phase, the plates were placed in an ambient air incubator at 37C for 30 min to allow the thrombin to enzymatically crosslink the fibrinogen into a fibrin matrix (Figure 15A). The PEG-enriched media was removed using a 12-channel micropipette and replaced with 100 μ l of fully supplemented media in each well. When applicable, this media addition was supplemented with stimuli as detailed in section 2.7. For the duration of each experiment, assay plates were imaged every 2 hours at 4x with an automated cell culture monitoring system (Incucyte S3; Essen

Biosystems). As the assay proceeded, the fibroblasts progressively remodelled the fibrin scaffold as illustrated in Figure 15C.

4.2.4 *Histologic analysis of fibrin microgels*

Contracted assays were harvested after 12 days of culture. These assays were prepared for histology, stained, and imaged as previously described for cultured spheroids. Briefly, the assays were washed with PBS and fixed in 4% paraformaldehyde (Alfa Aesar) for 1 hour at room temperature. The assays were stained with 0.5% methylene blue solution in PBS for 10 minutes at room temperature to aid in visualization during histology. Samples were placed in a cryomold containing optimal cutting temperate (OCT), and flash frozen in cooled isopentane. 10 um sections were obtained using a CryoStar NX70 cryostat (Thermo Fisher Scientific).

Upon warming to room temperature, the sections were washed with PBS, permeabilized with 0.2% Triton-X 100, and blocked for 1 hour at room temperature with 4% bovine serum albumin (BSA) (Millipore Sigma). Sections were stained for 30 min at room temperature with Sirius red (0.1% of Sirius red in saturated aqueous picric acid), as previously described for collagen bundle staining [221]. The samples were then washed with PBS, stained with DAPI for 15 minutes at room temperature, and coverslipped. Samples were imaged using a DMI8 microscope (Leica) equipped with 10x and 20x air objectives. Fluorescence was detected using Texas Red channel settings as previously described [222]. Mean fluorescence intensity was quantified in ImageJ as the average pixel intensity within the sectioned assay.

4.2.5 mRNA quantification by qPCR

RNA extraction and qPCR: 12 fibrin assays at the indicated time points were pooled together per condition, and lysed with 350 μ l of RLT lysis buffer. RNA was extracted from assays using an RNeasy Mini Kit (Qiagen, #74104) and was performed according to the manufacturer's instructions. RNA sample concentration was measured using a NanoDrop OneC Spectrophotometer (Thermo Fisher Scientific). A High-Capacity RNA-to-cDNA Kit (Applied Biosystems, #4387406) was used for reverse transcription; 400 ng of RNA for each sample was mixed with 10 μ l primer, 1 μ l reverse transcriptase enzyme and nuclease-free water to bring the final reaction volume to 20 μ l. The reaction was performed for 60 minutes at 37 C, followed by 5 minutes at 95 C using a Veriti Thermal Cycler (Applied Biosystems). qPCR was performed using a QuantStudio 3 Real-Time PCR System (Applied Biosystems). Each reaction consisted of 1 μ l cDNA, 10 μ l TaqMan Fast advanced master mix (Applied Biosystems, #4444556), 1 μ l primer, and 6 μ l nuclease-free water. TaqMan primers (Applied Biosystems) for smooth muscle actin (*ACTA2*, Hs00426835_g1), plasminogen activator (*PLAT*, Hs00263492_m1), Plasminogen activator inhibitor-1 (*SERPINE1*, Hs00167155_m1), collagen type I (*COL1A1*, Hs00164004_m1), plasminogen activator (*PLAU*, Hs01547054_m1), and Ki67 (MKI67, Hs01032443_m1) were utilized. The QuantStudio 3 was programmed with a 2 minute hold at 95 C, followed by 40 cycles of 95 C for 1 second and 60 C for 20 seconds. Each sample was run with biological triplicates. The relative gene expression was calculated using the $2^{-\Delta\Delta CT}$ method, with glyceraldehyde-3-phosphate dehydrogenase as the housekeeping gene (*GAPDH*, Hs02786624_g1). Fold changes were normalized with respect to the time zero

timepoint with no TGF- β 1 stimulation, and are reported as the mean with the error bars representing the minimum and maximum values.

4.2.6 *High-throughput brightfield image analysis*

After each experiment, brightfield images at two hour intervals from the 4x objective of our automated cell culture monitoring system (Incucyte S3; Essen Biosystems) were downloaded in jpeg format from the automated cell culture monitoring system. Separate processes for pixel classification, thresholding, and morphological filtering were implemented for the masking approach illustrated in Figure 17A in order to isolate the assay area from the background.

Image segmentation implemented Ilastic, a freely available image classification tool developed by the European Molecular Biology Laboratory. Ilastic's pixel classification utility implements a random forest classifier for quick and robust segmentation. In order to train the classifier, 10 characteristic images were selected to include different stages of ECM remodeling. In this step, each individual pixel is assigned a probability for belonging to layers for the background or the assay. Ilastic enables interactive training of the random forest classifier via user annotations of the training images. All default features ($\sigma = 0.3$ through 10 for intensity, edge, and texture) were utilized for this interactive training by methodically annotating mislabelled areas of each training image. Care was taken to equally annotate background and assay areas in order to prevent the algorithm from weighting features inappropriately. Through this iterative training method, the user can evaluate interactive predictions by the algorithm and then draw additional annotations to correct mistakes. When additional training annotations no

longer improved background noise and edge feature fit of the predicted mask over the assay area, the trained classifier was saved for future use. With each experiment, this trained classifier was reloaded and assay fit was evaluated on representative images (not from the training set) before use.

This pixel classification workflow performs semantic segmentation, and therefore returns a probability map for the background and assay area for each image. The probability map was transformed into background as assay area objects through thresholding. Thresholding of these probability masks then enabled generation of a single mask to isolate the assay area. A closing morphological filter with a 25x25 kernel was then applied to each mask in order to remove noise. This masking approach was implemented for each time-course brightfield image for every condition over the course of an experiment.

The area from segmented masks was used to quantify assay contraction. For each experimental replicate, a sigmoid curve was fit using the `curve_fit` function from the SciPy library in Python. The logistic function given by the equation in Figure 17C enabled automated extraction of the time point for 50% contraction and the maximum slope at the equation's centroid. In many cases, the final contracted assay was out of view for the 4x objective in the live cell imager. For this reason, final assay area was determined from brightfield images taken on a benchtop imaging system (2x objective; EVOS M7000; ThermoFisher) and evaluated by the same segmentation procedure described above.

Various concentrations of transforming growth factor type $\beta 1$ (Human Recombinant TGF- $\beta 1$; Peprotech) were used for validation due to its established anti-fibrinolytic and pro-fibrotic qualities. TGF- $\beta 1$ was added at indicated concentrations in the

assay media which was used to rinse and remove ATPS polymers after incubation. In order to visualize dynamics between assay contraction time and final assay area, kernel density estimate plots (KDE plots) were generated using the Seaborn Statistical Data Visualization library in Python 3. These bivariate kernel density estimates represent the probability density functions for each experimental condition.

In order to evaluate metrics not based on changes in assay area, the segmented images were used to generate masks that isolate the assay from image background. Within these masked regions, a variety of metrics were evaluated including average intensity, standard deviation, kurtosis, and skew from histograms of pixel intensity. Plots of time course changes in average pixel intensity were generated to evaluate ECM composition.

4.2.7 Phenotypic evaluation of stimuli

Our customized high-throughput image analysis approach was applied for phenotypic evaluation of all experiments. In order to evaluate assay remodeling behavior with established stimuli; experiments implemented different conditions of TGF- β 1, serum, and cell seeding density. TGF- β 1 was introduced at concentrations of 0, 0.5, 2, and 10 ng/mL; however the highest concentration did not contract within the duration of the experiment and was therefore omitted from analysis. In order to evaluate the remodeling effects of serum, foetal bovine serum (FBS, Lonza) at concentrations of 0, 1, 2, 4, and 8% by volume of the cell culture media was added during the washing step after fibrin crosslinking. For cell seeding density experiments, fibroblasts were suspended at appropriately modified concentrations in the dextran phase of the ATPS fibrin printing

formulation so that assays were printed with concentrations of 1, 2, 4, and 8 thousand cells per microliter within a 4 μ l assay.

In order to evaluate the capability of this assay to test the fibrinolytic and anti-fibrotic effects of therapeutic stimuli, a variety of drug compounds were introduced to the assays after the wash step. This included 1.0 μ M ifenprodil (MedChemExpress), 1 μ M nintedanib (Selleck Chem), 500 μ M pirfenidone (Selleck Chem), 10 μ M TM5275 (MedChemExpress), 0.50 μ M aprotinin (MedChemExpress), 1.0 μ M GLPG 1690 (MedChemExpress), and 20 μ M diethyl-pythiDC (AOBIOUS); all diluted and stored according to supplier data sheet recommendations. These concentrations were established in preliminary experiments that evaluated a range of concentrations used in prior literature. These stimuli were freshly mixed for each media change during experiments, and a minimum of four replicates were tested per experimental condition.

4.2.8 *Statistical Analysis*

All experimental values are reported as means \pm standard deviation. ANOVA tests were performed using the statsmodels library in Python 3 with the Tukey test for post-hoc pairwise comparisons. Experiments involving two independent variables (such as therapeutic stimulus and TGF- β 1) implemented two-way ANOVA to evaluate the significance of combined effects. Kernel density estimates were determined for KDE plots using the Seaborn Statistical Data Visualization library in Python 3.

4.3 Results and Discussion

In tissue repair, fibrin formation is followed by fibroblast migration, fibrinolysis and matrix remodeling. We previously reported a method to print microscale cell-laden fibrin gels to quantify cell-mediated fibrinolysis. Our prior study conditions, however, did not provide readouts of fibrosis formation such as collagen deposition and fibroblast activation.

In the work described here, we adapt our prior ATPS fibrin micro-printing technique to allow for high-throughput automated image-based analysis of fibroproliferation as well as fibrinolysis. This adaptation built upon the finding that a higher seeding density and the use of serum-supplemented media enabled fibroblast proliferation, differentiation, and collagen deposition. This newly discovered model for fibrin remodeling was characterized by staining histologic slices of remodeled matrices and quantifying mRNA expression in order to elucidate which proteins were affecting matrix turnover. Then, an automated image processing approach quantified different aspects of matrix remodeling from label-free brightfield images. Finally, the microscale cell mediated fibrinolysis-fibrosis assay was implemented to evaluate the effects of anti-fibrotic therapeutics on fibroblasts from normal and diseased donors.

4.3.1 *Fabrication of microscale fibrin matrices*

Biological environments establish fibrin matrices through coagulation, where a cascade of clotting factors activates thrombin to enzymatically crosslink fibrinogen into fibrin [161]. Similarly, synthetic fibrin scaffolds are formed by exposing monomeric fibrinogen to activated thrombin [181]. Our previously established technique for generating fibrin micro-scaffolds utilized an ATPS with PEG and dextran to improve

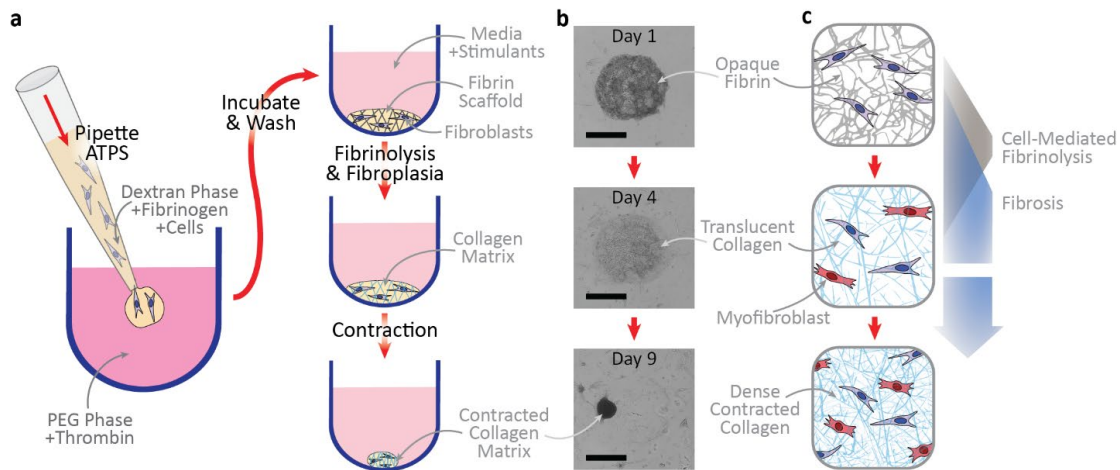


Figure 15. ATPS fibrin printing and cell-mediated remodeling: (a) Process schematic of ATPS generation of microscale fibrin droplets and subsequent remodeling. After the initial pipetting step, thrombin from the PEG phase diffuses into the dextran phase for controlled crosslinking of fibrinogen into fibrin over the incubation period. Subsequent remodeling includes concurrent fibrinolysis and collagen deposition, followed by contraction. (b) Characteristic brightfield microscope images (taken at 4x magnification) illustrate the assay progression when stimulated with 2 ng/mL of TGF- β 1. Scale bars are 1 mm. (c) Microscale illustration shows the changes in ECM organization at stages of remodeling. Fibrosis denotes deposition and accumulation of fibrous extracellular protein.

control over enzymatic crosslinking, which enables printing of unprecedentedly small cell-laden fibrin matrices with standard liquid handling equipment. This prior implementation of fibrin micro-printing was used to evaluate fibroblast-mediated fibrinolysis by utilizing lower seeding density (1000 cells/ μ l) in combination with a concentration of exogenous plasminogen comparable to levels found in serum [223]. However, most tissue *in vivo* is not exposed to serum-level concentrations. The majority of plasminogen is produced in the liver, so tissue availability depends on vascular permeability to plasma proteins [224]. In the current work, decreased availability of plasminogen in addition to higher fibroblast seeding density and serum supplemented media result in a significantly altered trajectory of fibrin remodeling compared to our prior approach. Rather than strictly degrading the

scaffold into fibrin degradation products and dissociated cells, these conditions enable deposition of significant collagen and contraction into a fibrotic spheroid.

In this approach, a microscale format was necessary to enable microplate implementation and evaluation with a conventional live-cell imager. In order to fit the entire assay within the field of view of a 4x objective, the fibrin scaffold needed an initial volume below 8 μ l. In order to establish this microscale fibrin environment, we implemented ATPS printing as previously described. The necessity for this ATPS environment in our microscale fibrin degradation assay comes from the capability of aqueous two-phase partitioning to control diffusion of thrombin into the fibrinogen droplet. This restricts enzymatic crosslinking of cell-laden fibrin matrices until after the droplets have been dispensed (Figure 15A). After a 30 minute incubation period, the fibrin was sufficiently polymerized and the ATPS solutions could be rinsed and replaced with growth media and stimulants for specific conditions.

During assay progression, remodeling is visually apparent in brightfield images as opaque fibrin transitioning into a translucent fibrous matrix and eventually contracting into a dense spheroid (Figure 15 B, C). Our previously implemented fibrin degradation assay demonstrated the opaque material to be fibrin, so qualitative analysis of the current assay indicates concurrent fibrinolysis and deposition of cell-secreted ECM. In the absence of serum, which contains plasminogen, the initial fibrin matrix remained opaque and intact with minimal change (Supplemental Video 2). Control conditions verified that presence of both serum and cells was necessary for degradation of the opaque fibrin scaffold, indicating that cell mediated activation of plasmin was necessary for fibrin degradation. Factors

contributing to altered fibrinolysis and increased collagen deposition are assessed in the following section.

4.3.2 *Response to TGF- β 1*

Exogenous addition of TGF- β 1 served as a broad pro-fibrotic stimulus to determine whether varying degrees of fibrosis are distinguishable in the context of this assay. Downstream signaling effects include inhibition of fibrinolysis, increased fibroblast proliferation, increased synthesis and deposition of connective tissue, and inhibition of connective tissue breakdown [225]. Preliminary qualitative assessment of microscale fibrin remodeling in our assay indicated dose-dependent increases in both timing of contraction and final contracted assay size. Specific biological contributions to these differences in remodeling were evaluated through histologic staining and qPCR analysis.

4.3.2.1 Final organization of deposited collagen

Histologic evaluation was used to determine the ECM content and organization of collagen in the final contracted assays. The most commonly used commercially-available method for quantification of deposited collagen is the Sircol™ insoluble collagen assay kit, which implements the dye Sirius Red F3B due to its high specificity for collagen [226]. These kits, however, are optimized for use on fixed quantities of excised tissue. Due to the low assay volume and variability in assay final size (Figure 16A), Sircol™ kits were not practical for use in this approach. Many alternative methods for benchtop quantification of collagen rely on ELISAs to evaluate soluble collagen and products of collagen synthesis. These methods were also infeasible for our application due to high background protein concentrations from the serum-supplemented media.

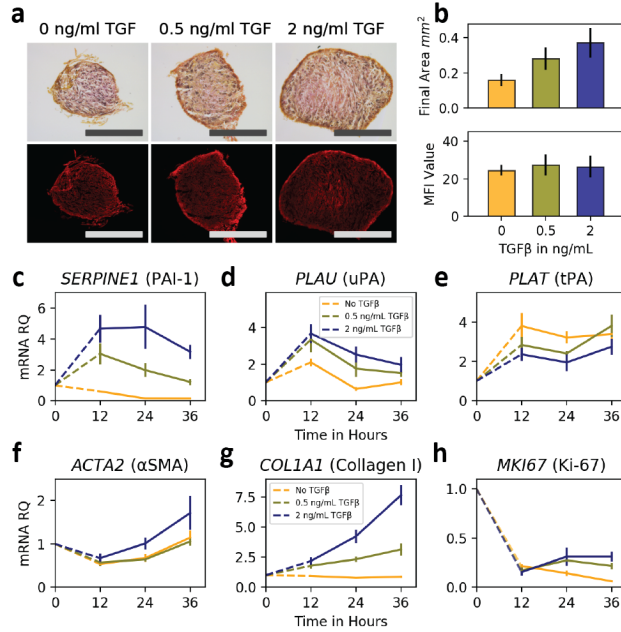


Figure 16. Matrix remodeling *in vitro*: (a) Brightfield images of histologic sections show the difference in final size between assays treated with varied concentrations of TGF-β1. The contracted assays were harvested after 12 days, and sections were stained with picrosirius red. Scale bars are 250μm. (b) Evaluation of mean fluorescence intensity demonstrates consistency in collagen organization between conditions. Quantification of mRNA expression via qPCR evaluated dose-dependent time-course changes in SERPINE1 (c), COL1A1 (d), ACTA2 (e), PLAU (f), PLAT (g), MKI67 (h) in response to concentrations of TGF-β1. The dotted lines indicate the zero time point used as reference for relative expression. Two-way ANOVA indicated significant combined effects of time and TGF-β1 for COL1A1 with $P < 0.01$; significant one-way effects for both variables with SERPINE1, PLAU, PLAT, and ACTA2 with $P < 0.01$; and significant one-way effects for only TGF-β1 concentration for MKI67 of $P < 0.01$.

Picrosirius red (PSR) utilizes the same anionic dye as Sircol™ assay kits to visualize collagen in paraffin embedded tissue sections. Under light microscopy, PSR stained collagen appears red and can be used for qualitative evaluation of collagen organization [221]. A variety of quantitative approaches for morphometric assessment of collagen networks implement polarized light to visualize fiber alignment; however, signal strength and hue under linear polarized light are heavily dependent on sample orientation [227]. Fluorescent imaging of PSR stained tissues with standard red filter sets yields a

strong red fluorescence signal that is sensitive, collagen-specific, and is unaffected by sample orientation [222, 227].

In order to evaluate deposited collagen, contracted assays were collected after 12 days of culture. Intermediate time points could not be sectioned due to adhesion of flat fibrin scaffolds to the microplate. Stained sections demonstrated consistent appearance of collagen between conditions, with a consistent increase in size for higher concentrations of TGF- β 1 (Figure 16A). Fluorescent micrographs demonstrate relatively homogenous collagen distribution for the interior of the contracted assay with higher deposition at the interface between the assay and the media. Evaluation of area demonstrated a dose-dependent increase in final contracted assay size ($P < 0.05$). Mean fluorescence intensity (MFI) was measured in order to evaluate relative differences in collagen organization between sections (Figure 16B). While this measure cannot provide absolute quantification of collagen content, it indicated relative consistency in organization of collagen networks between different TGF- β 1 conditions and the control.

Well-established mechanisms have linked TGF- β 1 signaling to exaggerated extracellular deposition of type I collagen in fibrosis [228]. Here, histologic evaluation demonstrated consistency in organization of collagen between histologic slides. This indicates that assay size is at least partially influenced by the total amount of collagen accumulated during assay progression; however, there are likely differences in collagen compaction due to variations in fibroblast contractility between conditions. Additional analysis is necessary to better characterize variability in collagen density. Potential contributors to collagen remodeling are evaluated in the following section.

4.3.2.2 Alterations in mRNA expression

In order to further evaluate the factors contributing to altered ECM remodeling with TGF- β 1 stimulation, qPCR was used to determine mRNA expression for proteins involved in fibrinolysis and collagen deposition. These genes were chosen for their involvement in specific pathways contributing to slowed fibrinolysis, increased collagen deposition, and increased myofibroblast activation in response to TGF- β 1 stimulation. Time points at 12, 24, and 36 hours evaluated time-dependent and dose-dependent response to TGF- β 1 within the dynamic fibrin-remodeling environment. Quantification of mRNA for *SERPENE1* demonstrated significant time-dependent and dose-dependent increases in expression in response to TGF- β 1 (Figure 16C).

The induction of *SERPENE1* by TGF- β 1 signaling is a well-established connection between TGF- β 1 and fibrinolysis because *SERPENE1* encodes the protein plasminogen activator inhibitor type 1 (PAI-1) [229]. PAI-1 is the dominant inhibitor of fibrinolysis, and acts by binding to the active sites of urokinase-type and tissue-type plasminogen activators (uPA and tPA). These three regulators have been evaluated extensively in animal models of IPF to evaluate their potential involvement in fibrosis pathogenesis [177]. TGF- β 1 mediated increases in PAI-1 contribute to the anti-fibrinolytic environment during certain stages of wound healing and fibrosis [230]. Additionally, gene polymorphisms of TGF- β 1 and PAI-1 have been associated with susceptibility to IPF due in part to dysregulation of the fibrinolytic system [231].

Time course measurements also show significant increases in expression of the genes for tPA and uPA relative to the initial time point, but the effect of TGF- β 1 stimulation

is inverted between these two plasminogen activators. uPA demonstrated relative upregulation compared to the control time series, while tPA demonstrated a relative downregulation (Figure 16 D, E). However, the qPCR results for tPA and uPA do not indicate relative quantities between the two, so additional quantitative evaluation is necessary to determine the dominant TGF- β 1 mediated changes.

This highlights the potential utility for a phenotypic assay in evaluating multifactorial contributions to fibrotic remodeling. While PAI-1 is generally credited as the anti-fibrinolytic mediator in fibrosis, other components of the fibrinolytic system demonstrate significant differential expression in response to a pro-fibrotic stimulus. Additionally, there are several other activators and inhibitors not evaluated here that are produced by cells and play roles in regulating conversion of plasminogen into plasmin [170-174]. This phenotypic evaluation of fibrin remodeling can incorporate these effects even though expression of individual contributing proteins was not specifically quantified.

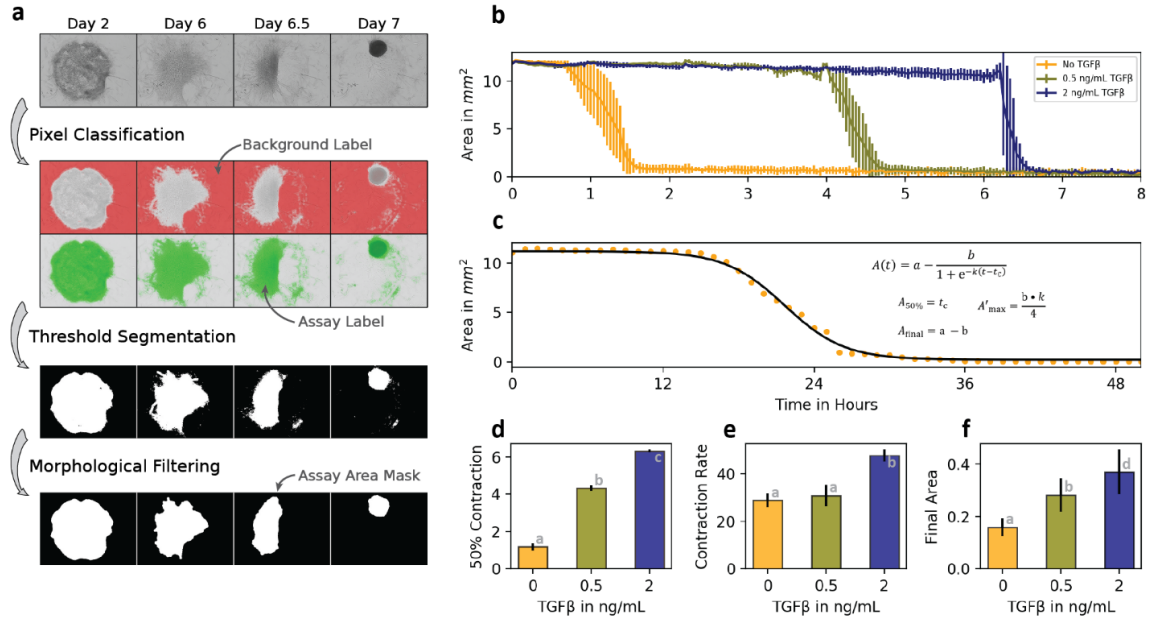
In addition to its effects on the fibrinolytic system, TGF- β 1 also has established roles in myofibroblast activation and collagen synthesis [192]. Myofibroblasts are collagen-producing cells that express the contractile protein alpha smooth muscle actin (α SMA). Increases in myofibroblast activation and myofibroblast resistance to apoptosis have been identified as major contributors to IPF pathogenesis [12]. Evaluation of *ACTA2* mRNA demonstrated significant time-course increases in α SMA expression as well as increased expression for the highest concentration of TGF- β 1 (Figure 16F). These time-course changes may be due to a variety of factors including biomechanical feedback, cytokine secretion, or downstream signaling of the fibrinolytic system [12, 232, 233].

COL1A1 encodes the pro-alpha1(I) chain, which is a primary component of type I collagen. Quantification of mRNA for *COL1A1* demonstrated significant combined effects of TGF- β 1 and time (Figure 16G). Collagen expression in pulmonary fibrosis is heavily dependent on myofibroblast activation [234], but increased collagen expression in fibroblasts has also been linked to downstream effects of anti-fibrinolytic environments [220]. Due to the variety of TGF- β 1 effects on cellular activity, the increased expression of *COL1A1* likely results from the combinatorial effects of multiple contributing pathways.

Expression of *MKI67* mRNA was evaluated as a marker for proliferation. The substantial decrease from initial RQ reference value to the first time point may be due to that time point's proximity to trypsinization and manipulation during experimental setup (Figure 16H). In later time points, *MKI67* expression was significantly upregulated with higher concentrations of TGF- β 1, indicating increased cellular proliferation relative to the control condition. TGF- β 1 is a key regulator of ECM remodeling and dysregulation of TGF- β function is closely associated with fibrosis [228]. Our assay reveals multiple effects of TGF- β 1 on fibroblasts including its ability to impact ECM remodeling through regulation of the fibrinolytic system and upregulated collagen synthesis.

4.3.3 *Label-free quantification of fibrotic remodeling*

In order to evaluate fibrosis *in vitro*, conventional approaches generally quantify specific contributors such as activation of myofibroblasts or concentration of soluble collagen. Here, an automated approach was developed in order to broadly assess phenotypic changes associated with fibrin remodeling. Preliminary qualitative assessment indicated that pro-fibrotic stimulation with TGF- β 1 increased the time before assay



contraction and increased the final assay size after contraction. There were also changes in assay appearance associated with the transition from an opaque fibrin matrix to a translucent collagen matrix.

The first step of image analysis was to isolate the assay from the background of each image. Due to transitions in assay appearance during remodeling, the basic image segmentation software for our live-cell imager was inadequate for accurate segmentation. In order to consistently isolate assay area, it was necessary to implement an approach that

utilized machine learning. Our approach utilized Ilastik, a freely available image classification tool developed by the European Molecular Biology Laboratory.

Ilastik's pixel classification tool utilizes a random forest algorithm that can be interactively trained through iterations of user annotations on a small set of training images. It was important here to use training images from time points throughout the experiment with a variety of different image features. Otherwise, the trained algorithm might misclassify brightfield images from stages of remodeling that were omitted from the training set. When additional training annotations no longer improved background noise and edge feature fit, the trained pixel classification algorithm was saved for future use. Figure 17A illustrates the output of this pixel classification algorithm. Ilastik performs semantic segmentation, which returns probability maps that can be converted into masks by thresholding. In order to remove remaining background noise, opening and closing morphological filters were applied to the masks.

After establishing segmented masks, time-course changes in assay area were plotted in order to visualize assay remodeling (Figure 17B). Fitting time-course data from each individual well with a sigmoidal curve facilitated extraction of the time point for 50% contraction and the maximum slope at the sigmoid's centroid (Figure 17C). Figure 17D shows changes in the 50% contraction time point in response to different TGF- β 1 concentrations. ANOVA indicated statistical significance of these differences in degradation time ($P < 0.01$), and post-hoc pairwise analysis with the Tukey test demonstrated statistically significant differences between specific conditions. The dose-dependent increases in time for 50% contraction correspond with changes in mRNA expression from the previous section.

Maximum contraction rate (Figure 17E) was determined as the centroid slope of the sigmoidal fit for each experimental replicate (Figure 17C). This value reflects contractile stress generated by cells within the assay. In order for contraction to initiate, stress within the assay must overcome adhesion to the microwell. In some cases, initial contraction was not sustained and occurred in multiple steps (Appendix Figure A-5). Due to this inconsistency, the slope of contraction did not serve as a reliable indicator of assay remodeling activity.

Final contracted cross-sectional area was also evaluated in our analysis, and demonstrated significant dose-dependent increase with TGF- β 1 stimulation (Figure 17F). *COL1A1* mRNA quantification and histologic analysis demonstrated increased collagen synthesis and deposition in response to TGF- β 1. Additionally, qualitative evaluation of assay appearance and pixel intensity quantification leading up to contraction (Appendix Figure A-4) also indicate increased deposition of collagen with TGF- β 1. These data and observations together suggest that final contracted cross-sectional area of the assay is correlated with total collagen deposition. However, variability in collagen density due to differences in generation of contractile stress likely also contribute to final cross-sectional area due to differences in compaction density. Fibroblast proliferation may also play a role. Additional evaluation is necessary to determine relative contributions to final cross-sectional area.

PAI-1 may be particularly relevant in this remodeling process due to its multiple effects on fibrin remodeling. In addition to inhibiting fibrinolysis, PAI-1 can disrupt integrins, which form cell-matrix adhesions [218]. Appendix Figure A-4 shows increasing pixel intensity leading up to assay contraction. We previously established that this increase

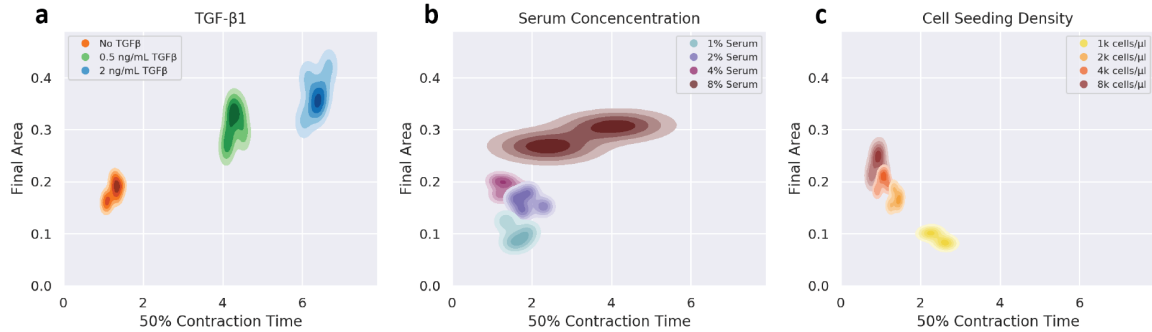


Figure 18. TGF- β 1, serum concentration, and seeding density effects: Output contraction times and final assay areas from image processing analysis were used to plot kernel density estimates showing interplay between contraction time and final assay area. (a) Stimulation with TGF- β 1 resulted in increases in both 50% contraction time and final assay area. (b) Evaluation of serum concentration demonstrated relatively consistent contraction time with increasing final assay area in response to higher serum concentrations. The disparity between apparent slope and maximum slope for 8% serum is detailed in Appendix Figure A-4. (c) Cell seeding density had an inverse relationship between contraction time and final assay area. Final contracted area is shown in mm² and statistical differences are annotated on graphs in Appendix Figure A-6.

in pixel intensity corresponds with degradation of the fibrin matrix. Initially, all conditions degraded fibrin at a similar rate; however, fibrinolysis slows down substantially with higher concentrations of TGF- β 1 after the initial 12 hours. This timing corresponds with the increases in PAI-1 expression determined by qPCR in the previous section. Fibrin degradation initially proceeds at similar rates between conditions until the TGF- β 1 mediated increase in PAI-1 can establish an anti-fibrinolytic environment. Time-course evaluation of pixel intensity before contraction may therefore serve as an indicator for fibrin degradation.

4.3.4 Evaluation of serum and cell number effects

In order to validate remodeling behavior, the established stimuli of TGF- β 1, serum, and cell seeding density were evaluated for their effects on matrix turnover. The relationship between contraction time and final contracted area of remodeled assays was

visualized using kernel density estimates to approximate probability density functions for each experimental condition. Figure 18A demonstrates the effects of TGF- β 1 stimulation on the 50% contraction time and final area as determined in the previous section. With increasing concentrations of TGF- β 1, the time for 50% contraction and the final assay area increased in a dose dependent manner.

The effects of serum concentration on matrix remodeling were also evaluated. FBS contains a complex mix of growth factors, hormones, cytokines, proteases, zymogens, co-factors, latent TGF- β 1, and inhibitors that influence cellular activity. In the context of fibrin remodeling, one important component of FBS is plasminogen which can be activated by fibroblasts into plasmin for cell-mediated fibrinolysis. The fibroblast growth media used for propagating NHLF cells contained 2% FBS, but conditions were evaluated here ranging from serum-free to 8% serum content in the assay media.

Serum free conditions did not contract within the length of the experiment, but there were slight changes in assay cross-sectional area over the course of the experiment. In the absence of serum, assays maintained their opaque appearance, indicating that very minimal fibrin degradation had occurred. Evaluation of contraction rate indicated no significant difference in contraction time for most conditions, however some replicates of the 8% condition contracted in multiple steps, resulting in larger values for 50% contraction time (Appendix Figure A-5).

Final assay cross-sectional area exhibited dose-dependent increases in response to serum concentration, indicating increased deposition of collagen (Figure 18B). Due to the vast number of distinct proteins in serum, it is difficult to speculate which specific

components contribute to the altered assay remodeling. However, latent TGF- β 1 and fibroblast growth factor (FGF) are both present in serum and have established effects on collagen production. These increases in concentration of serum are relevant to fibrotic disease. *In vivo* tissue availability of serum proteins depends largely on vascular permeability, and dysregulated endothelial permeability and vascular leak have long been associated with pulmonary fibrosis [217, 224].

The initial fibroblast seeding density used to form assays is also relevant to IPF. Fibroblasts from fibrotic lungs have particularly proliferative phenotypes, resulting in higher numbers of fibroblasts and myofibroblasts in fibrotic tissue [235]. Here, initial fibroblast seeding density were varied between 1000 and 8000 cells/ μ l in order to evaluate the impact on remodeling (Figure 18C). Evaluation of contraction rate indicated significant dose dependent decreases in contraction time and increases in maximum contraction slope. Final assay cross-sectional area exhibited dose-dependent increases in response to higher cell density. The volume of cells within each assay contributes significantly to the final contracted assay size, so additional evaluation is necessary to determine differences in collagen deposition between conditions. Final volume of the contracted assay is dependent on a variety of contributors including cell number, ECM accumulation, and contractile stress.

4.3.5 *Fibroblast donor variability*

Alternative donors of normal and diseased fibroblasts were utilized in our assay to evaluate variability in remodeling behavior. Prior studies have demonstrated exaggerated

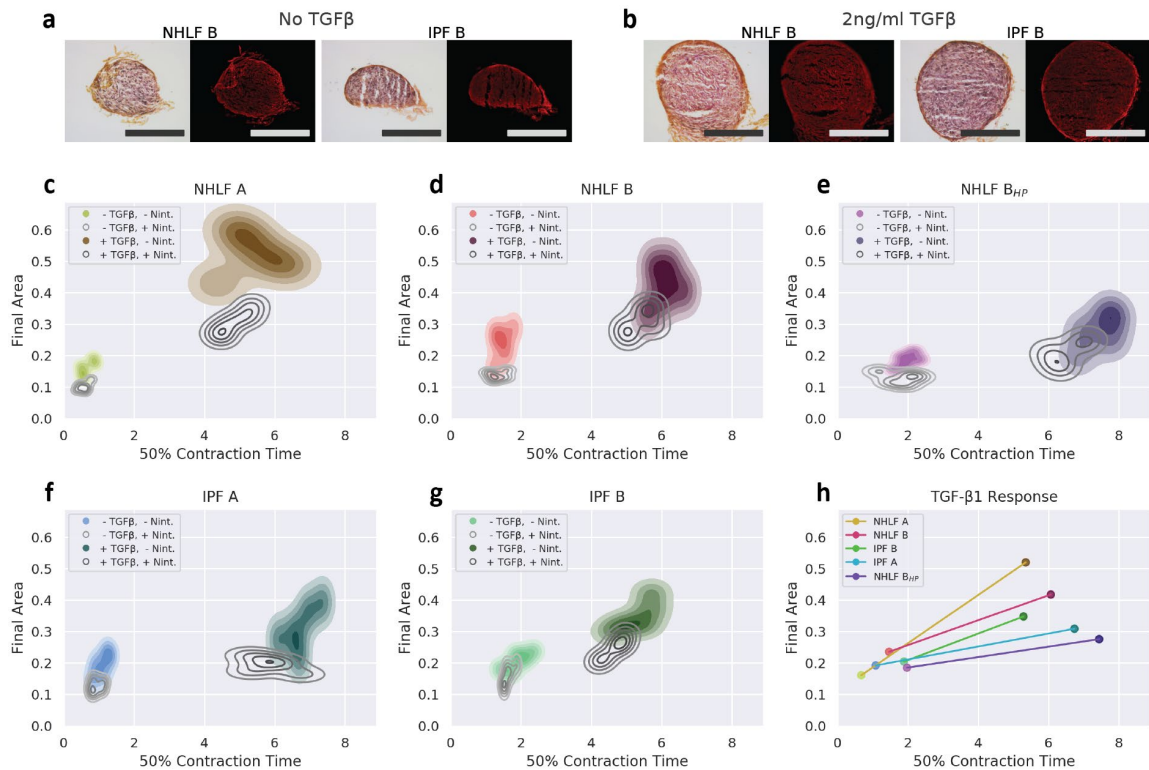


Figure 19. Consistency in response between cell lines: (a, b) Histologic sections show final contracted assays for NHLF B and IPF B with picosirius red staining. For each example, color brightfield images are shown on the left with fluorescent images on the right. Scale bars are 250 μ m. (c-g) Individual plots for each fibroblast donor show remodeling response to TGF- β 1 and nintedanib stimulation. (h) TGF- β 1 response was compared between fibroblast donors with lines indicating the average responses with and without TGF- β 1. Final areas are indicated in mm² and statistical differences are annotated on graphs in Appendix Figure A-7.

fibrogenic response in aged and diseased pulmonary fibroblasts compared to normal donors [197]. PAI-1 production and TGF signaling have both been implicated in this pathogenic alteration in behavior [10, 236]. We evaluated remodeling with pulmonary fibroblasts from 2 normal donors, 2 IPF diseased donors, and one higher passage (p11) in order to evaluate consistency in assay progression. Each fibroblast lineage was evaluated with TGF- β 1 to determine consistency in response to pro-fibrotic stimulus, in addition to nintedanib as an FDA-approved therapeutic.

Final contracted assays from normal and diseased fibroblasts were stained for histologic evaluation. These sections demonstrated consistency in organization of collagen in fluorescent images (Figure 19 A, B). However, PSR staining in color brightfield images had a darker hue in sections with IPF fibroblasts. It has previously been demonstrated that dysregulation of TGF- β 1 signaling in diseased fibroblasts can contribute to increased activation of myofibroblasts in IPF [237]. It is possible that the altered hue of PSR staining in brightfield images reflects differences in contractility and compaction, but additional analysis is necessary to evaluate potential contributions.

Evaluation of assay contraction time and final cross-sectional area demonstrated altered fibrin remodeling profiles between conditions (Figure 19 C-G). These shifts are particularly apparent in the response to TGF- β 1, where IPF fibroblasts and high passage fibroblasts have a muted effect on final assay area (Figure 19H). These data indicate consistency in remodeling response to TGF- β 1 and nintedanib between cell lineages, but magnitude of response to these stimuli varies between fibroblast donors.

Prior studies have demonstrated increased sensitivity to TGF- β in diseased fibroblasts [10, 238], but TGF- β conditions in the fibrin remodelling assay had smaller final assay sizes compared to normal fibroblasts. Prior literature has also shown that diseased fibroblasts express more PAI-1, differentiate more easily into myofibroblasts, and synthesize more type I collagen [10, 197, 236]; however, both IPF fibroblasts and the higher passage number normal fibroblasts in this fibrin remodelling assay contracted into a smaller final assay size. This smaller final size may indicate decreased accumulation of collagen or greater contractility of cells within the assay.

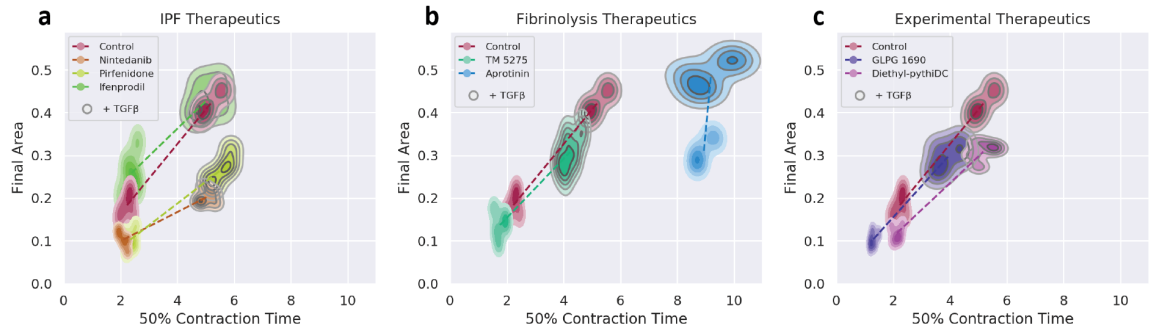


Figure 20. Response to therapeutic stimuli: (a) Time-course changes in assay area show the effects of IPF therapeutics on remodelling behavior. (b) Evaluation with therapeutics targeting the fibrinolytic system demonstrate the impact of a PAI-1 inhibitor (TM 5275) and a tPA/uPA inhibitor (aprotinin). (c) Additional experimental therapeutics were also evaluated. Final areas are indicated in mm² and statistical differences are annotated on graphs in Appendix Figure A-8.

4.3.6 Drug response

We then evaluated changes in remodeling with different therapeutic stimuli in order to assess applications as a pharmaceutical model of fibrotic disease. In IPF, specific sites of proliferative injury are identified as dense aggregates of ECM-producing fibroblasts, termed fibroblastic foci [17]. In clinical evaluation of IPF severity, the extent of fibroblastic foci within lung biopsies is used as a predictor of survival. Interestingly, the most important prognostic indicator from histologic analysis is the extent of young connective tissue present within the fibroblastic foci rather than the extent of interstitial cellularity or ECM accumulation [131]. Newly remodeled ECM is therefore a particularly important target for IPF therapeutic intervention.

Here, we compared fibrin remodeling between healthy and diseased lung fibroblasts with a variety of stimulants (Figure 20). Ifenprodil was included as a potential IPF therapeutic that is currently being evaluated in clinical trials. Final assay area showed marginal increases compared to control in most conditions with one condition showing a

significant increase (Figure 20A). Ifenprodil inhibits lung fibroblast proliferation and differentiation, and has been shown to reverse the damage of initial acute lung injury in an animal model of pulmonary fibrosis [239]. While the mechanism for ifenprodil's effects on fibrosis is not yet fully understood, current evidence indicates that it may play a role in reducing invasiveness of immune cells and fibroblasts [240, 241]. Ifenprodil may therefore act on aspects of fibrosis pathogenesis not evaluated in this assay.

Nintedanib conditions showed significant decreases in final area for all conditions ($P < 0.01$). Nintedanib is a multiple tyrosine kinase inhibitor with effects on expression of ECM proteins and TGF- β 1 induced signaling, so its tyrosine kinase inhibitory activity likely contributed to decreased final assay area through its effect on collagen production [242]. Stimulation with pirfenidone also demonstrated a significant decrease in fibrinolysis rate in most conditions ($P < 0.01$; except IPF TGF- β 1-). The specific mechanism of pirfenidone is unclear, but it has been established to reduce fibroblast proliferation, α -SMA expression, and collagen synthesis [243, 244].

Our prior assay for cell-mediated fibrinolysis did not show significant changes in fibrin degradation in response to nintedanib and pirfenidone, indicating minimal effects on the fibrinolytic system. By showing significant effects of these therapeutics on fibrinolysis, the fibrin remodelling assay demonstrated the utility of evaluating broader contributions to fibrosis. Nintedanib and pirfenidone are the two current FDA-approved therapeutics for IPF. In clinical use, administration of these drugs is incapable of halting or reversing fibrosis, and can only slow the spread of fibrotic scarring in the lungs [26]. The insufficiency of current IPF therapeutics served as motivation for development of this assay.

To address the need for alternative treatment strategies, several recent reviews have proposed components of the fibrinolytic system as potential targets for therapeutic intervention (Figure 20B) [214-216]. Inhibition of PAI-1 is of particular interest, as increased expression in IPF has been associated with worse clinical outcome [9, 10]. TM5275 is a small molecule inhibitor of PAI-1, which has been shown to minimize the extent of fibrotic remodeling in an animal model of pulmonary fibrosis [245]. Stimulation of assays with TM5275 decreased final assay size for all conditions, although these decreases were only statistically significant in the IPF condition without TGF- β 1 ($P < 0.05$). Interestingly, TM5275 was among the two drugs that demonstrated significant changes in contraction time (Appendix Figure A-8). This indicates that delays in start time of contraction may be related to inhibition of fibrinolysis by PAI-1.

GLPG 1690 also demonstrated significant changes in contraction time (Appendix Figure A-8). This decreased time to contract may also be related to PAI-1 production. GLPG 1690 has been demonstrated to decrease TGF- β 1-induced production of several pro-fibrotic mediators in fibroblasts which are involved in PAI-1 production [246]. Final contracted area was also significantly decreased in all conditions treated with GLPG 1690.

Diethyl-pyridylDC is an inhibitor of prolyl 4-hydroxylase, which plays a role in post-translational modifications that stabilize deposited collagen, and was included to evaluate the role of collagen matrix stability in remodeling of the assay [196]. However, prolyl 4-hydroxylase is responsible for a variety of other post-translational modifications of proteins important to cell function, so there are multiple potential contributing pathways to the measured changes in assay remodeling [202]. Alterations in PAI-1 expression may be also

be involved, but further evaluation of mRNA or protein expression would be necessary to confirm specific changes to the fibrinolytic system [199, 203].

Fibrosis is the aggregate outcome of diverse dysregulated contributions, and the readouts of this fibrin remodelling assay incorporate a broader variety of contributors than other current *in vitro* assays for fibrosis. A broad evaluation of protein and mRNA expression for components of each contributing pathway of the remodelling process would be necessary to fully understand which specific pathways cause changes to remodelling behaviour for a given set of conditions. This assay provides a pragmatic alternative by enabling phenotypic evaluation of the fibrinolytic system with high resolution time-course data for fibrin degradation. This enables visualization of the formation of fibrosis *in vitro*, resulting from the cumulative remodelling effects of fibrinolysis and collagen deposition.

4.4 Conclusion

Coordinated fibrinolysis and collagen deposition are necessary for restoration of tissue function after injury. However, no *in vitro* assays currently evaluate the combined effects of these processes on cell-mediated fibrin remodeling. Here, microscale fibroblast-laden fibrin matrices were used to investigate the cumulative effects of fibrinolysis and collagen deposition on fibroblastic scar formation. By implementing ATPS printing of microscale fibrin scaffolds, we established an *in vitro* analogue to the provisional ECM in wound healing. This fibrin micro-scaffold was remodeled by fibroblasts through concurrent fibrinolysis and fibroplasia, followed by contraction. Through implementing and evaluating this assay, we demonstrated applications for an *in vitro* model for aberrant fibrin remodeling in evaluation of anti-fibrosis therapeutics. Despite different therapeutic

mechanisms, the assay was able to indicate changes in fibrotic remodeling with diverse therapeutic compounds at physiologically relevant concentrations.

Given the variety of contributors to dysregulation of fibrinolysis seen in fibrosis, cancer, and metabolic disease; this phenotypic assay provides a potentially valuable research tool for further studies in these fields. By mimicking matrix remodeling of the provisional fibrin matrix *in vivo*, this method offer a new approach to phenotypically evaluate fibrotic remodelling with applications in biological inquiry, personalized medicine, and drug discovery.

CHAPTER 5. CONCLUSIONS AND FUTURE DIRECTIONS

Dysregulation of fibrinolysis contributes to the pathogenesis of fibrosis, cancer, and metabolic disease; however, no prior assays have evaluated the phenotypic effects of dysregulated fibrinolysis on cell-mediated ECM remodeling. The microscale fibrin remodeling assay described in this dissertation provides a new research tool for label-free evaluation of fibroblast behavior within a fibrin scaffold, with a variety of applications in biomedical research and drug discovery.

5.1 Conclusions

5.1.1 *Novel fibrin remodeling assay*

Fibrosis is the aggregate outcome of various dysregulated wound healing pathways. While wound healing is comprised of steps for initial epithelial damage, inflammation, proliferation, and remodeling; *in vitro* assays for fibrosis generally focus on quantifying specific proteins or mRNAs in a single stage of the remodeling process. In order to establish an assay that evaluates multifactorial contributions to the pathogenesis of fibrosis, this dissertation established a phenotypic assay for fibroblastic remodeling of microscale fibrin scaffolds.

Here, we recapitulated certain aspects of the provisional fibrin matrix, which is present during the initial steps of wound healing. By culturing fibroblasts within a fibrin clot with physiologically relevant concentrations of serum and nutrients, fibroblasts are able to remodel the fibrin scaffold into a collagen-rich fibrous ECM. The work presented

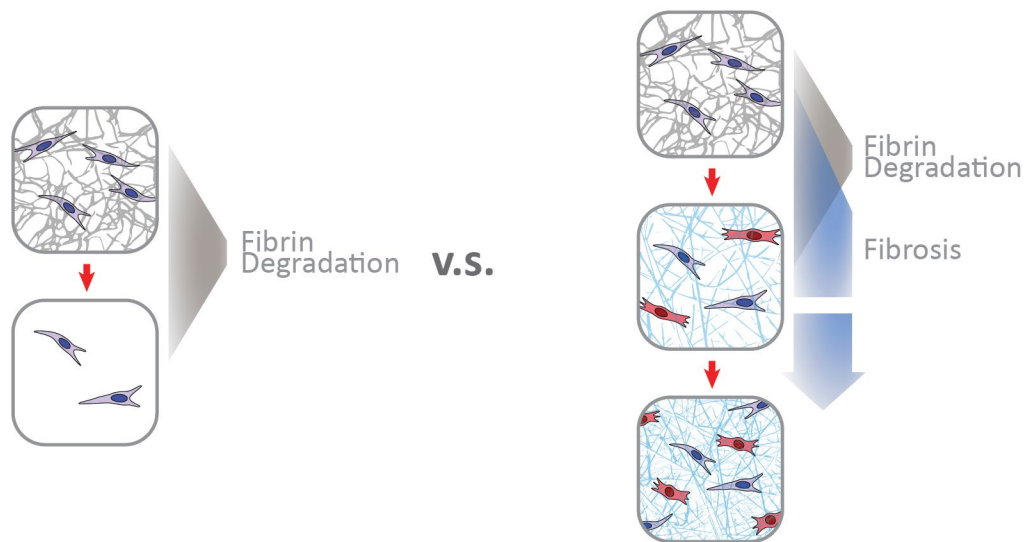


Figure 21. Fibrinolysis assay vs. remodeling assay: Chapter 3 of this dissertation established an assay for cell-mediated fibrinolysis, where fibroblasts activated plasminogen into plasmin in order to degrade the fibrin scaffold. In Chapter 4 of this dissertation, modified culture conditions enabled concurrent fibrinolysis and collagen deposition, so that formation of fibrosis was visualized *in vitro*.

here investigates the development and implementation of microscale fibrin scaffolds to assess cell-mediated fibrinolysis and remodeling. This required establishing a new approach to fabricate microscale fibrin scaffolds, which implemented aqueous two-phase printing for improved control over enzymatic crosslinking of fibrin. This offered unprecedented control over scaffold volume and cell seeding density for sub-microliter scaffolds, using standard liquid handling equipment.

These micro-printed fibrin scaffolds were implemented as two separate assays (Figure 21). In the first assay, serum-free media and late addition of exogenous plasminogen enabled evaluation of cell-mediated fibrinolysis. This assay for cell-mediated fibrinolysis demonstrated our capability to evaluate changes to the fibrinolytic system through label free evaluation of brightfield images. However, evaluation of this assay with conventional IPF therapeutics showed no significant change in fibrin degradation with

established drugs. This demonstrated insufficiency of this assay in evaluating fibrosis, as well as insufficiency of IPF therapeutics at addressing contribution of fibrinolytic system to fibrosis.

The second assay evaluated remodeling into collagen-dense fibrous matrix. Serum supplemented media in addition to a higher cell-seeding density and larger assay volume enabled concurrent fibrinolysis and collagen deposition (Figure 21). With these modified conditions, the fibroblast-laden fibrin scaffold effectively formed a fibrotic mass that could be quantified as a readout of fibrosis. This readout demonstrated effects for a variety of therapeutic compounds with diverse mechanisms. These results illustrated that therapeutic stimuli targeted at fibrinolysis had an effect on fibrotic remodeling besides just their degradation of the fibrin matrix. Drugs that targeted the anti-fibrinolytic environment and persistence of the fibrin matrix resulted in altered collagenous remodeling that affected the final size of the contracted assay. These findings provide novel insight into the contribution of aberrant fibrinolysis on fibrotic remodeling, and this newly established experimental model can facilitate future *in vitro* studies of fibrotic remodeling.

5.1.2 *Context within the complexity of the lung*

Respiratory function requires maintenance of a complex biological environment that enables efficient gas exchange. Lung architecture is optimized to meet this demand through thin barrier membranes, substantial tissue elasticity, and a high surface area to volume ratio (Figure 22). In order to maintain this environment, various cell types are involved in coordinated remodeling processes that continually degrade and deposit components of the ECM. Resident interstitial fibroblasts constitute much of this activity in

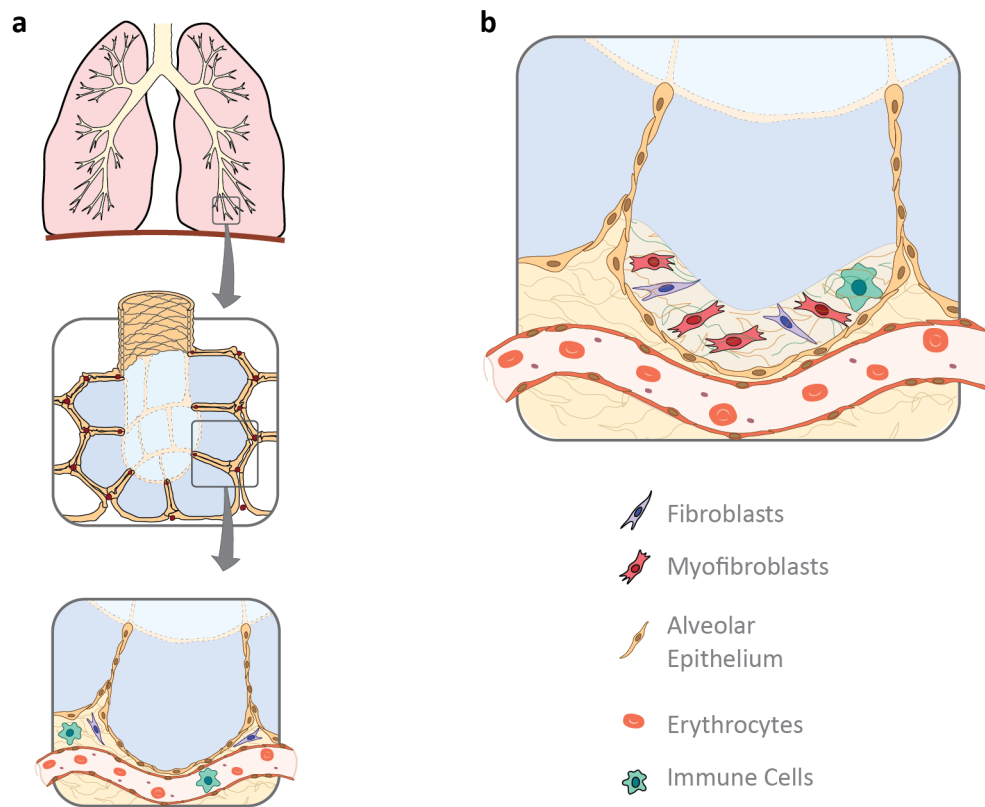


Figure 22. Lung structure and cellular composition: (a) Lungs require significant structural organization in order to optimize gas exchange function. The hierarchical structures accomplish this through thin barrier membranes, substantial tissue elasticity, and a high surface area. (b) The provisional extracellular matrix forms following tissue damage, and contains substantial cellular heterogeneity. Immune cells include predominantly monocytes, macrophages, neutrophils, dendritic cells, and eosinophils.

healthy tissue; however, several other cell types are involved in remodeling following tissue damage. During the wound repair process, differentiated myofibroblasts are predominantly responsible for ECM repair. These myofibroblasts can originate from circulating fibrocytes, epithelial cells (through epithelial mesenchymal transition), or resident interstitial cells [247]. The model system presented in this dissertation has exclusively been implemented with pulmonary interstitial fibroblasts. Due to heterogeneity

in remodeling behavior due to cell lineage and origin, the contribution of fibroblast and myofibroblasts to pathological remodeling varies by fibroblast source.

Airway epithelial cells also play a significant role in regulation of remodeling. In addition to their role in recovery of the epithelial layer after injury, epithelial cells use chemical and mechanical signaling to help coordinate activity of various growth factors and cytokines, including TGF- β 1 [248]. The effects of epithelial regulation on remodeling by fibroblasts and myofibroblasts helps to minimize space occupied by the interstitial matrix, with the epithelial and endothelial basement membranes fusing together. This allows for minimal distance and efficient gas exchange across the alveolar–capillary barrier [249]. When epithelium is damaged, it initiates the coagulation cascade in addition to releasing pro-inflammatory and pro-fibrotic factors [250]. This environment recruits immune cells and fibroblasts to the injury site in order to initiate the wound healing process. Additionally, crosstalk between epithelium and fibroblasts regulates altered collagen production in wounded and diseased lungs [251]. Because the fibrin remodeling assay starts with a fibroblast-laden fibrin scaffold, it bypasses the steps of coagulation and cellular invasion. Altered initial conditions involving thrombin, fibrinogen, serum, or cell concentrations in the assay may replicate certain aspects of altered epithelial activity; however, inclusion of airway epithelial cells in the fibrin remodeling assay would be necessary to more fully evaluate the effects of their chemical and mechanical signaling on fibroblastic remodeling.

Immune cells are also important in the remodeling of lung tissue due to their role in accommodating protection from infection and injury without considerably affecting tissue structure and function. Various cell types coordinate tissue repair responses that

entail inflammation for removal of potential threats, proper wound closure, and regeneration to maintain and restore healthy tissue. These cell types include monocytes, macrophages, neutrophils, dendritic cells, and eosinophils; which each have unique roles at certain stages of the wound healing process [252]. Activated macrophages play a particularly important role in remodeling due to their production of inflammatory cytokines and growth factors. Positive feedback loops between macrophages and fibroblasts promote augmented collagen production in wound healing and fibrosis [253]. By overlooking the effects of macrophages in our model, their contributions to the remodeling process are neglected.

In vitro models necessarily simplify the cellular heterogeneity and micro-environment from *in vivo* biological systems. In order to enable high-throughput adaptation, model systems must balance sophistication with ease of fabrication. By focusing specifically on fibroblast-mediated remodeling of fibrin, the assay developed in this thesis recapitulates aspects of wound healing related to fibrinolysis, collagen accumulation, and matrix contraction. Future implementations of this assay may incorporate additional cell types and modified microenvironments in order to address questions involving cellular interaction and mechanical feedback. However, *in vitro* assays will always neglect many of the interactions present *in vivo*. There are simply too many diverse feedback loops between cells, tissues, and organs. Animal models are also often insufficient to evaluate pathophysiology and therapeutic effects due to differences in enzymatic profiles and differences in pathologic mechanism in the animal model. Although the fibrin remodeling assay does provide convincing and intriguing results; specific

research question need to focus on mechanisms specific to fibroblast-matrix interactions and remodeling.

5.1.3 Fibrin remodeling as a model for IPF

Coordinated fibrinolysis and collagen deposition are necessary for restoration of tissue function after injury, and these processes are significantly dysregulated in IPF. The model system presented in this dissertation enables label-free phenotypic evaluation of the fibrin remodeling by fibroblasts. Despite the consensus that dysregulated coagulation and fibrinolysis contribute to IPF pathogenesis, current FDA-approved therapies have no significant effect on regulation of fibrinolysis [254, 255].

The fibrin remodeling assay enables specific questions about fibroblast-mediated fibrinolysis and collagen deposition in the fibrin-rich provisional ECM. Our fibrinolysis assay from Chapter 3 demonstrated that the IPF therapeutics nintedanib and pirfenidone have no significant effects on fibrin degradation. Then, in Chapter 4 we demonstrated that stimuli targeting the fibrinolytic system can have a significant impact on fibrosis formation. This approach of phenotypically evaluating drug effects on fibrin remodeling enabled demonstration of significant decreases in fibrotic remodeling with significantly lower concentrations of pirfenidone than prior studies. However, the drug ifenprodil still showed no significant effects on remodeling. This therapeutic is currently in stage 3 clinical trials, showing promising effects on IPF patients. Prior studies indicate that systemic interactions or crosstalk with other cell types may be responsible for ifenprodil's mechanism in IPF. Demonstrating remodeling effects with ifenprodil may therefore require a more sophisticated *in vitro* model in order to demonstrate its effects.

Future implementations of this fibrin remodeling assay may focus on enabling other cell types to contribute to therapeutic effects. In particular, alveolar epithelial cells and alveolar macrophages play an important role in IPF pathogenesis. The epithelium acts as both a physical and immunological barrier against the environment, but dysregulated epithelial cells in the IPF lung experience loss of barrier permeability and injury in the absence of external stimulus. This altered behavior affects cytokine production, inflammation, and myofibroblast activation in the fibrotic lung [250]. In addition to dysregulated epithelium, overactive macrophages in IPF have demonstrated excessive expression of inflammatory cytokines and growth factors. This creates a positive feedback loop between macrophages and fibroblasts, resulting in increased collagen production [253]. Drug effects on epithelial cells and macrophages are therefore an important consideration in evaluating IPF therapeutics.

While most drugs evaluated in Chapter 4 demonstrated altered remodeling activity with only fibroblasts, many of these compounds have established effects on other cell types. Nintedanib and pirfenidone have both been shown to minimize epithelial to mesenchymal transition in small airway epithelium and reduce the production of inflammatory cytokines in macrophages [256-259]. Other compounds from Chapter 4 have similarly demonstrated therapeutic effects on cell types besides their remodeling effects on fibroblasts and myofibroblasts. Co-culture adaptations of this fibrin remodeling assay may integrate epithelial cells or macrophages in order to more broadly evaluate additional contributions to fibrotic remodeling in IPF.

5.2 Future Directions

5.2.1 High-Throughput Screening for COVID-19 Therapeutics

Findings from this thesis have already been used to support application of this assay to evaluate potential COVID-19 therapeutics. The pathophysiology of SARS-COV 2 is still largely unknown, but fibrin remodeling appears to play a major role in resolution of severe infections. Damage to alveolar epithelial cells by SARS-COV 2 and accompanying bacterial infection cause edema and subsequent coagulation to form fibrin clots in the lungs [260]. This can create a positive feedback cycle of fibrin formation, myobroblast activation, collagen production, and stiffening of the lungs that can cause additional epithelial damage. By implementing this assay to find therapeutics that minimize fibrotic remodeling of fibrin, we may be able to suggest prophylactic drugs that lessen the extent of damage during severe stages of COVID-19. Our efforts to evaluate FDA drug libraries for fibroblastic remodeling may help determine therapies that can help improve remodeling of fibrin clots in the lungs to minimize permanent damage in the lungs.

However, fibrin remodeling is only a small aspect of COVID-19 pathogenesis. Immune response is vital to clearance of the virus, and persistence of the fibrin matrix may play a role in containing immune cells as they fight the virus. Additionally, non-plasmin signaling of the fibrinolytic system may be involved in generation of the cytokine storm [261]. An overly fibrinolytic environment could therefore inadvertently contribute to increases in inflammatory cytokines, with potentially damaging systemic effects.

Other important aspects of covid-19 pathogenesis are beyond the scope of this assay. Questions involving differences in immune response, severity of cytokine storm,

and development of systemic damage require alternative model systems for evaluation. Other *in vitro* models, animal models, and human data are necessary to address these unanswered questions regarding COVID-19 pathogenesis and treatment.

5.2.2 *Evaluation of Nox4 Inhibitor for IPF*

Our lab also has an ongoing grant to evaluate a novel Nox4 inhibitor for its effects on fibrotic remodeling with *in vitro* models of fibrosis. Both direct and indirect mechanisms linking reactive oxygen species and TGF- β 1 pathways have been identified as potential pathogenic contributors in IPF; however, no current IPF therapeutics use this as a target [262]. Additionally, these pathways target some of the age-specific changes in ROS metabolism that correlate with IPF. Preliminary experiments with hydrogen peroxide in our cell-mediated fibrinolysis indicated that fibrin degradation in our system is sensitive to ROS, so we hope to see alleviations in fibrotic remodeling in response to this novel Nox4 inhibitor. This application may require adaptations of the fibrin remodeling assay that evaluate remodeling over longer periods of time. Dynamic culture conditions may also be implemented to evaluate interventional therapy that is introduced after assays are already on a pathogenic trajectory.

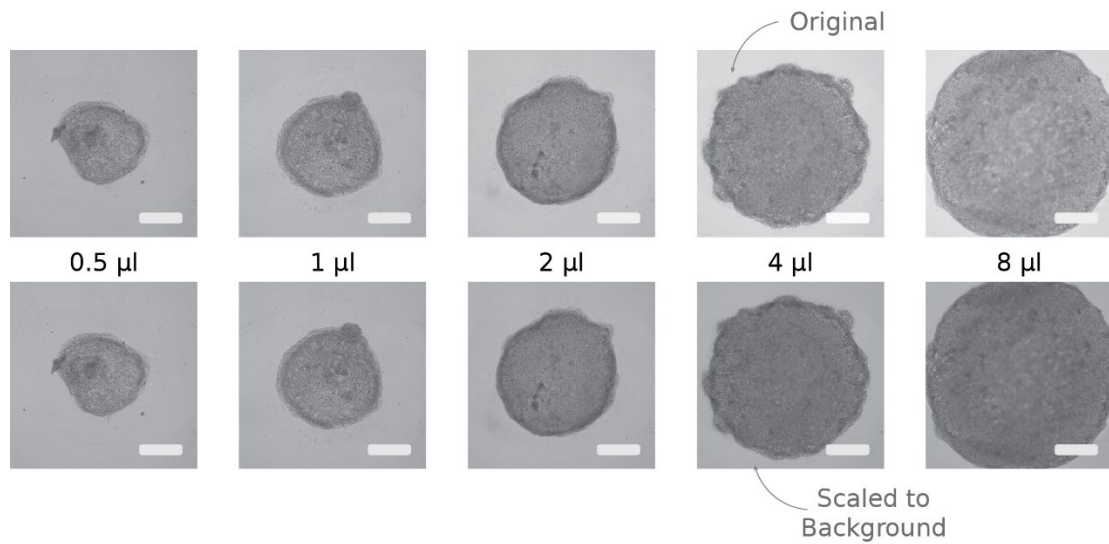
5.2.3 *Co-culture models*

In order to evaluate additional contributors to the multifactorial process of ECM remodeling of the lungs, it will be interesting to evaluate co-culture models in this assay. In particular, epithelial cells and macrophages have been shown to alter fibroblast phenotypes in the context of fibrotic remodeling. Preliminary experiments with small airway epithelial cells in the fibrin scaffolds demonstrated immediate fibrin degradation

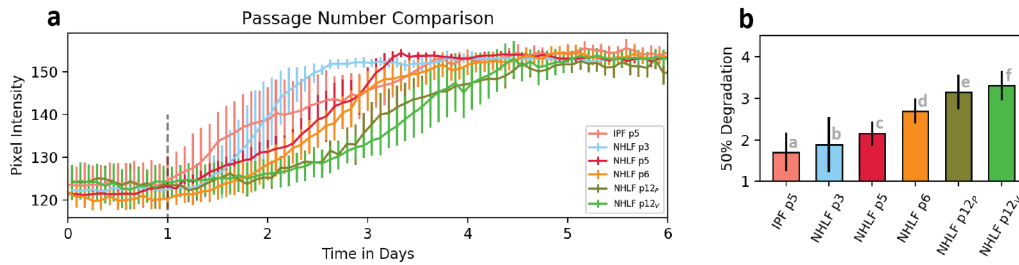
regardless of stimulus. Endothelial cells are known to be particularly pro-fibrinolytic, producing high amounts of tPA [263]. Future adaptations of this experiment may add different amount of intact or damaged epithelial cells to fibroblast-laden assays in order to evaluate contributions of epithelium and damaged epithelium to fibrotic remodeling. Macrophages will also be included in co-culture assays in order to evaluate the effects of macrophage-secreted factors on remodeling. However, in sophisticated co-culture models, the additional elements of variability can make assay results more difficult to interpret. In order to differentiate between conditions, these models need to be geared towards specific questions. Co-culture models may be uniquely geared towards evaluating cellular invasion, differentiation, and synergistic drug effects involving positive feedback mechanisms or crosstalk. Future adaptations of fibrin remodeling assays may introduce unique capabilities which can address unanswered questions about fibrosis pathogenesis and treatment.

APPENDIX A. SUPPLEMENTAL INFORMATION

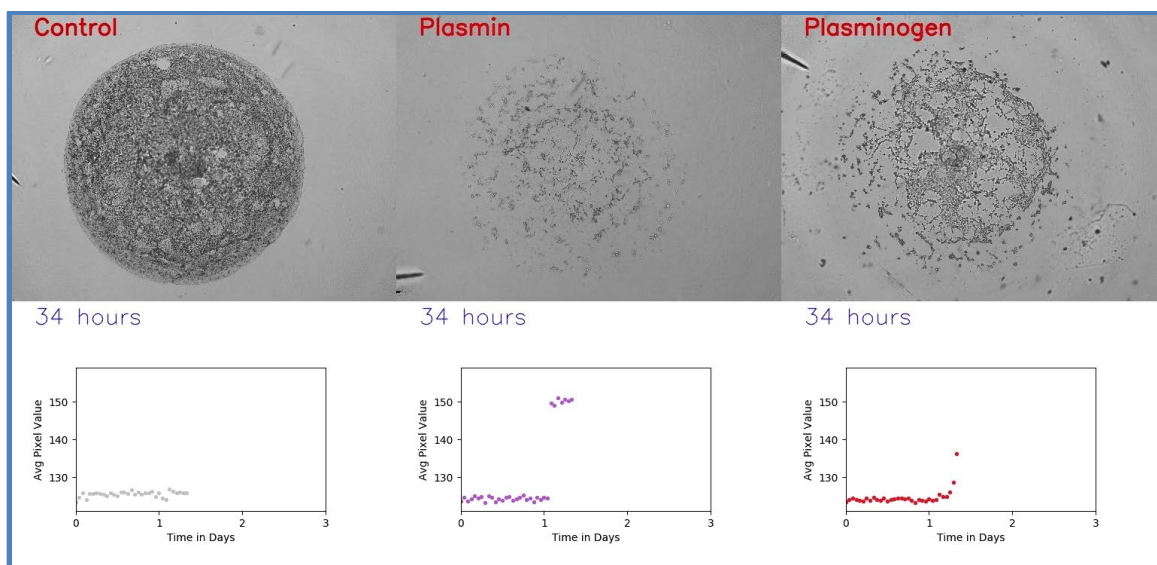
A.1 Supplemental fibrinolysis



Appendix Figure A-1. Brightness correction for live cell imaging: The Incucyte S3 (Essen Biosystems) automatically adjusts image brightness to maintain white balance, with no option to manually fix the relevant settings. In order to compensate for this automated adjustment of images, brightfield micrographs were re-scaled so that the background was consistent between images. This adjustment was necessary for the volume evaluation in Figure 12. Here, upper images show original brightfield and lower images show adjustments made using an automated script in Python 3. These corrected images were used for analysis in Figure 12 D-F. Scale bars are 1mm.

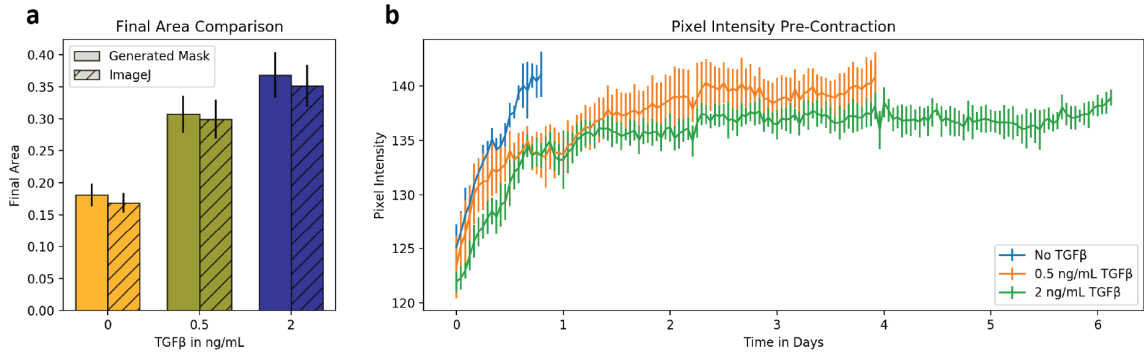


Appendix Figure A-2. Comparison of control conditions: Overlapping conditions from different experiments were compared according to cell passage number. All assays shown used 1 μ l of fibrin with 1000 fibroblasts and plasminogen added at 24 hours, with no additional stimuli. Respective conditions come from IPF therapeutic comparison in Figure 14 (IPF p5), TGF- β 1 response in Figure 13 (NHLF p3), NHLF therapeutic comparison in Figure 14 (NHLF p5), cell number effect in Figure 13 (NHLF p6), plasminogen timing in Figure 11 (NHLF p12_p), and volume consistency in Figure 12 (NHLF p12_v). Passage numbers were compared by time-course pixel intensity (**a**) and time to 50% degradation (**b**). (ad, ae, af, be, bf, ce, cf = $P < 0.01$ by post-hoc Tukey test)

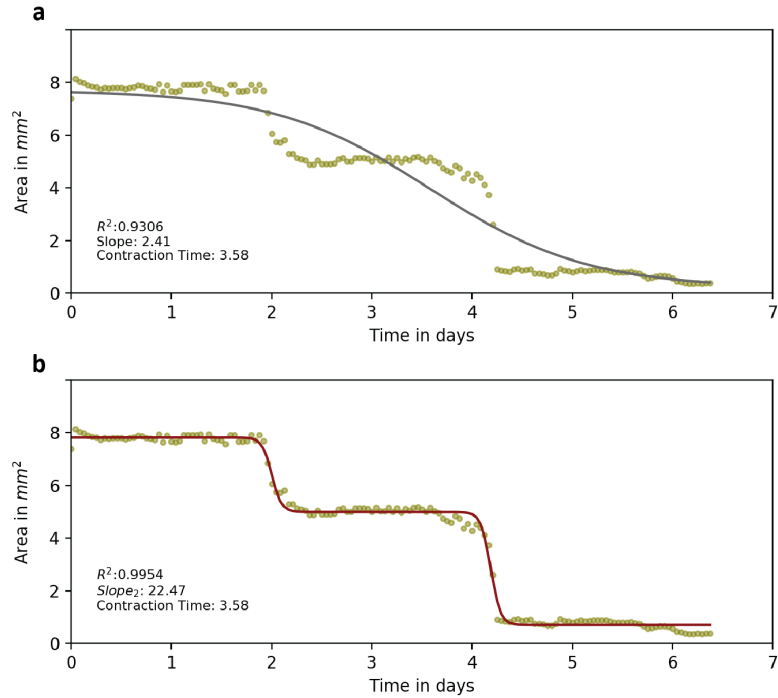


Appendix Figure A-3. Description of Supplemental Video 1 - Fibrinolysis: This video demonstrates degradation of fibroblast-laden fibrin scaffolds with plasmin and plasminogen added at 24 hours. With active plasmin, the matrix degrades almost immediately; however, plasminogen is delayed due to the necessity for plasminogen to be activated by cellular activity. Graphs below each micrograph illustrate changes in average pixel intensity as determined by our automated image processing approach. Micrographs were taken by the Incucyte S3 with 4x objective.

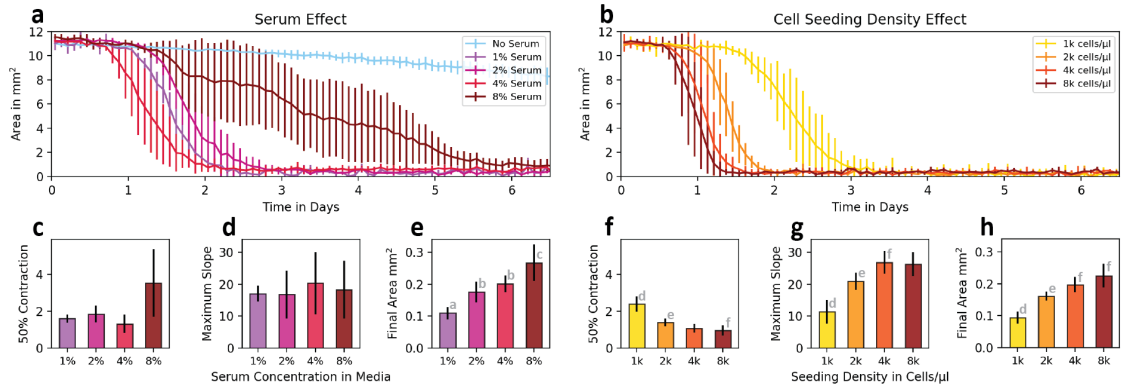
A.2 Supplemental ECM remodeling



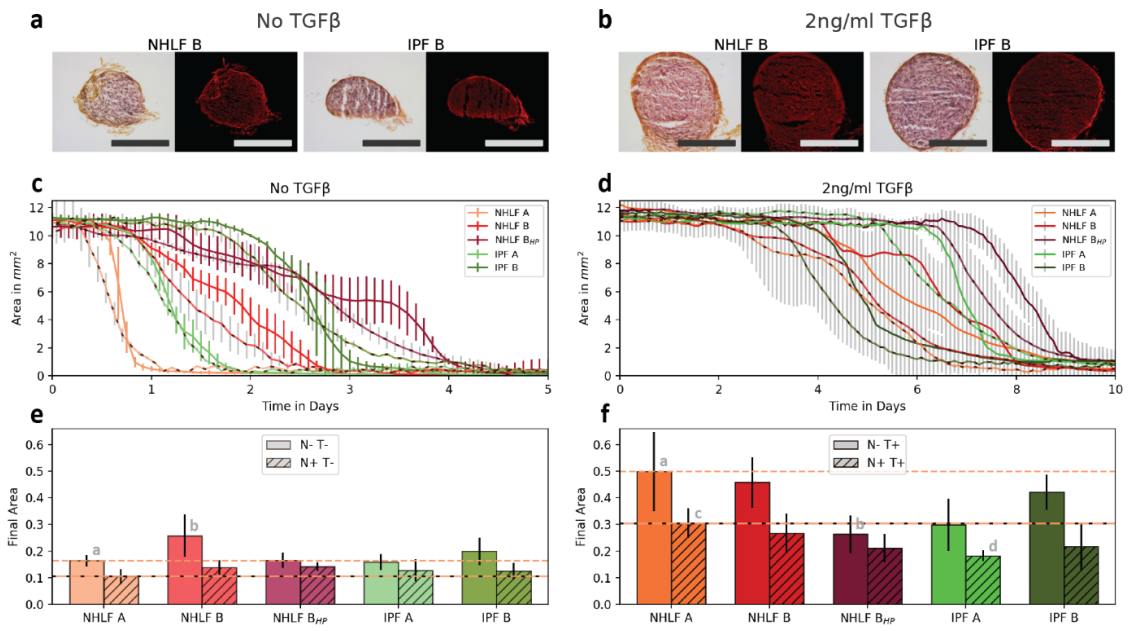
Appendix Figure A-4. Area validation and time-course pixel intensity: **(a)** In order to validate the automated output from the assay mask generator, final assay sizes were compared between the automated image processing approach and ImageJ. This comparison showed no significant differences between alternate determinations of final contracted assay area. **(b)** Leading up to contraction, image brightness within the masked region was evaluated for different TGF- β 1 concentrations. While initial slopes appeared similar between conditions, the lines for time course pixel intensity diverged after 12-24 hours.



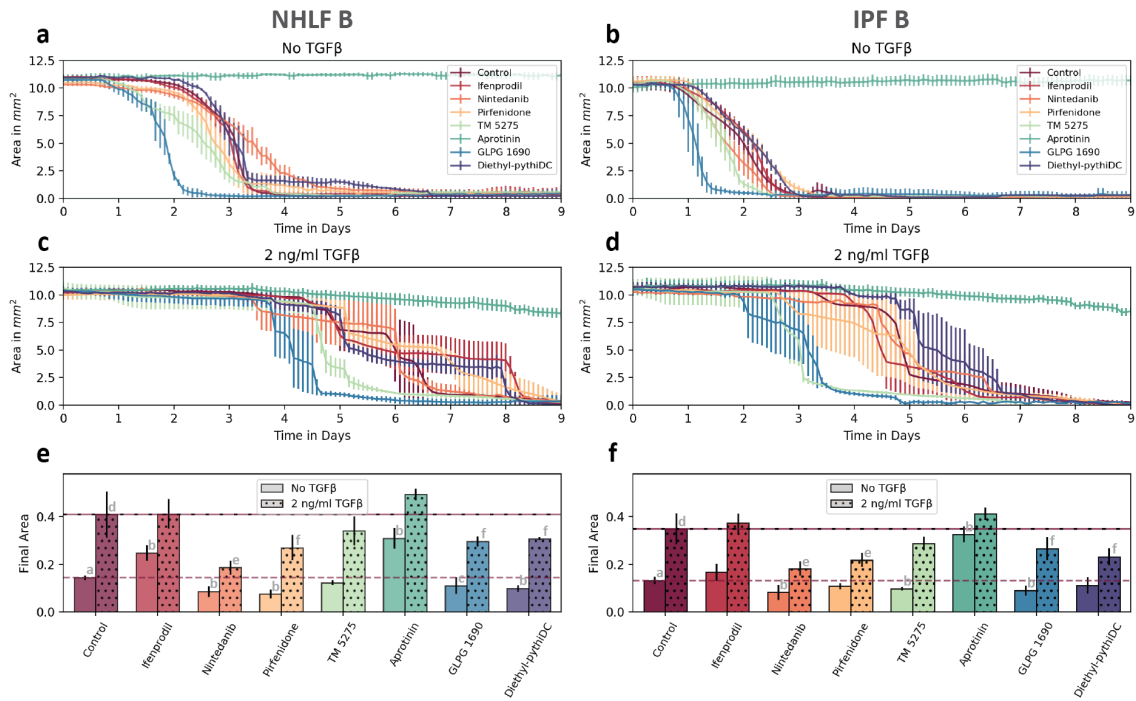
Appendix Figure A-5. Multi-step contraction and double sigmoid fit: Many conditions with higher concentrations of TGF- β 1 or serum contracted in a multi-step process. **(a)** The single sigmoid had relatively low R^2 values, so an alternative approach **(b)** using a double sigmoid was used for improved fit. This enabled more accurate determination of maximum slope.



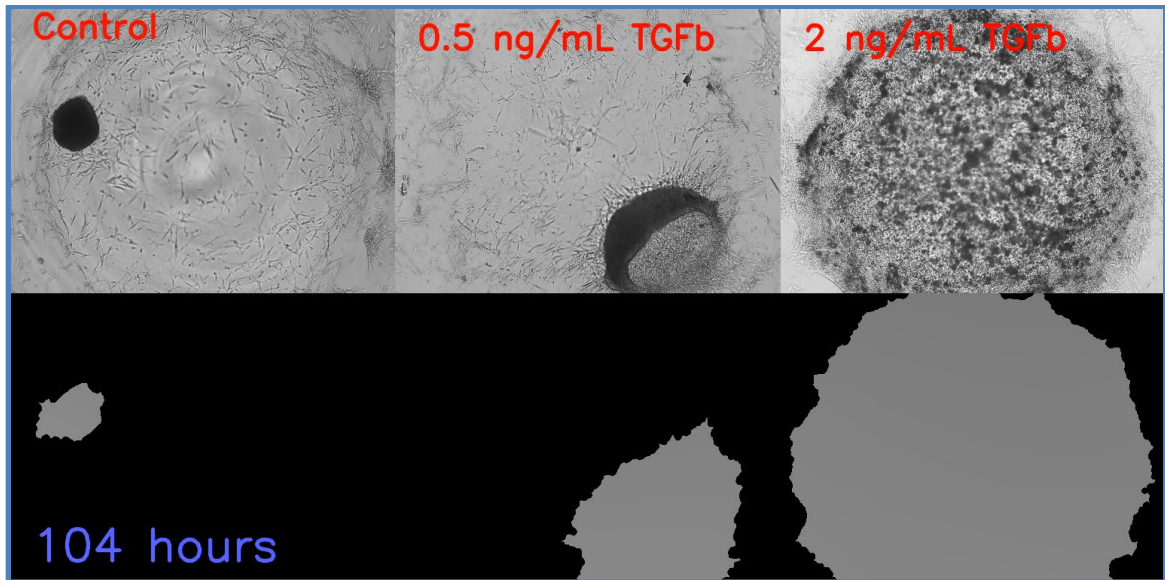
Appendix Figure A-6. Serum concentration and seeding density effects: **(a, b)** Time-course changes in assay area show the effects on assay contraction of FBS concentration on the left and fibroblast seeding density on the right. Fitting of sigmoidal functions to each experimental replicate enabled extraction of 50% contraction time (in days) **(c, f)** and maximum slope **(d, g)**. Note that the disparity between apparent slope and maximum slope for 8% serum (a, d) is detailed in Appendix Figure A-2. **(e, h)** Final contracted area was also determined for each condition, shown in mm². (Statistical significance: ab, bc, ef = $P < 0.05$; de = $P < 0.01$)



Appendix Figure A-7. Consistency in response between cell lines: **(a, b)** Histologic sections show final contracted assays for NHLF B and IPF B with picrosirius red staining. For each example, color brightfield images are shown on the left with fluorescent images on the right. Scale bars are 250 μ m. Time-course changes in assay area show the effects of cell line variability on assay contraction with no TGF- β 1 **(c)** and with 2 ng/ml TGF- β 1 **(d)**. Dotted lines indicate conditions with the IPF therapeutic nintedanib. **(e, f)** Final contracted area was also determined for each condition. (Statistical significance: ab, cd = P < 0.01)



Appendix Figure A-8. Response to therapeutic stimuli: **(a, b)** Time-course changes in assay area show the effects of various therapeutic stimuli on NHLF (left) and IPF fibroblasts (right) in the absence of TGF- β 1. **(c, d)** Parallel conditions to the upper graphs show the effects of these therapeutics with addition of 2 ng/ml TGF- β 1. **(e, f)** Final contracted area was also determined for each condition, indicated in mm². (Statistical significance: ab, de = P < 0.01; bc, df = P < 0.05)



Appendix Figure A-9. Description of Supplemental Video 2 – ECM Remodeling: This video demonstrates altered remodeling of fibroblast laden fibrin scaffolds with different concentrations of TGF- β 1. Higher concentrations result in delayed contraction and larger final size of the contracted matrix. Graphs below each micrograph demonstrate the image processing output of area masks for each time point. Micrographs were taken by the Incucyte S3 with 4x objective.

REFERENCES

1. Broughton, G., 2nd, J.E. Janis, and C.E. Attinger, *The basic science of wound healing*. *Plast Reconstr Surg*, 2006. **117**(7 Suppl): p. 12S-34S.
2. Diegelmann, R.F. and M.C. Evans, *Wound healing: an overview of acute, fibrotic and delayed healing*. *Front Biosci*, 2004. **9**: p. 283-9.
3. Borensztajn, K., B. Crestani, and M. Kolb, *Idiopathic pulmonary fibrosis: from epithelial injury to biomarkers--insights from the bench side*. *Respiration*, 2013. **86**(6): p. 441-52.
4. Dunsmore, S.E. and D.E. Rannels, *Extracellular matrix biology in the lung*. *Am J Physiol*, 1996. **270**(1 Pt 1): p. L3-27.
5. Last, J.A. and K.M. Reiser, *Collagen biosynthesis*. *Environ Health Perspect*, 1984. **55**: p. 169-77.
6. Margadant, C. and A. Sonnenberg, *Integrin-TGF-beta crosstalk in fibrosis, cancer and wound healing*. *EMBO Rep*, 2010. **11**(2): p. 97-105.
7. Wynn, T.A., *Common and unique mechanisms regulate fibrosis in various fibroproliferative diseases*. *J Clin Invest*, 2007. **117**(3): p. 524-9.
8. Mutsaers, S.E., et al., *Mechanisms of tissue repair: from wound healing to fibrosis*. *Int J Biochem Cell Biol*, 1997. **29**(1): p. 5-17.
9. Kotani, I., et al., *Increased procoagulant and antifibrinolytic activities in the lungs with idiopathic pulmonary fibrosis*. *Thromb Res*, 1995. **77**(6): p. 493-504.
10. Huang, W.T., et al., *Plasminogen activator inhibitor 1, fibroblast apoptosis resistance, and aging-related susceptibility to lung fibrosis*. *Exp Gerontol*, 2015. **61**: p. 62-75.
11. Li, B. and J.H. Wang, *Fibroblasts and myofibroblasts in wound healing: force generation and measurement*. *J Tissue Viability*, 2011. **20**(4): p. 108-20.
12. Phan, S.H., *The myofibroblast in pulmonary fibrosis*. *Chest*, 2002. **122**(6 Suppl): p. 286S-289S.
13. Abe, R., et al., *Peripheral blood fibrocytes: differentiation pathway and migration to wound sites*. *J Immunol*, 2001. **166**(12): p. 7556-62.

14. Marudamuthu, A.S., et al., *Role of the urokinase-fibrinolytic system in epithelial-mesenchymal transition during lung injury*. Am J Pathol, 2015. **185**(1): p. 55-68.
15. Raghu, G., et al., *Incidence and prevalence of idiopathic pulmonary fibrosis*. Am J Respir Crit Care Med, 2006. **174**(7): p. 810-6.
16. Kim, K.K., et al., *Alveolar epithelial cell mesenchymal transition develops in vivo during pulmonary fibrosis and is regulated by the extracellular matrix*. Proc Natl Acad Sci U S A, 2006. **103**(35): p. 13180-5.
17. Katzenstein, A.L. and J.L. Myers, *Idiopathic pulmonary fibrosis: clinical relevance of pathologic classification*. Am J Respir Crit Care Med, 1998. **157**(4 Pt 1): p. 1301-15.
18. Young, I.H. and P.T. Bye, *Gas exchange in disease: asthma, chronic obstructive pulmonary disease, cystic fibrosis, and interstitial lung disease*. Compr Physiol, 2011. **1**(2): p. 663-97.
19. Canestaro, W.J., et al., *Drug Treatment of Idiopathic Pulmonary Fibrosis: Systematic Review and Network Meta-Analysis*. Chest, 2016. **149**(3): p. 756-66.
20. Groll, J., et al., *Biofabrication: reappraising the definition of an evolving field*. Biofabrication, 2016. **8**(1).
21. Bajaj, P., et al., *3D Biofabrication Strategies for Tissue Engineering and Regenerative Medicine*. Annual Review of Biomedical Engineering, Vol 16, 2014. **16**: p. 247-276.
22. Moroni, L., et al., *Biofabrication: A Guide to Technology and Terminology*. Trends in Biotechnology, 2018. **36**(4): p. 384-402.
23. Kamm, R.D., et al., *Perspective: The promise of multi-cellular engineered living systems*. APL Bioengineering, 2018. **2**.
24. Wynn, T.A., *Fibrotic disease and the T(H)1/T(H)2 paradigm*. Nat Rev Immunol, 2004. **4**(8): p. 583-94.
25. King, T.E., Jr., A. Pardo, and M. Selman, *Idiopathic pulmonary fibrosis*. Lancet, 2011. **378**(9807): p. 1949-61.
26. Ahluwalia, N., B.S. Shea, and A.M. Tager, *New therapeutic targets in idiopathic pulmonary fibrosis. Aiming to rein in runaway wound-healing responses*. Am J Respir Crit Care Med, 2014. **190**(8): p. 867-78.
27. Selman, M. and A. Pardo, *Revealing the pathogenic and aging-related mechanisms of the enigmatic idiopathic pulmonary fibrosis. an integral model*. Am J Respir Crit Care Med, 2014. **189**(10): p. 1161-72.

28. Betensley, A., R. Sharif, and D. Karamichos, *A Systematic Review of the Role of Dysfunctional Wound Healing in the Pathogenesis and Treatment of Idiopathic Pulmonary Fibrosis*. J Clin Med, 2016. **6**(1).
29. Waters, D.W., et al., *Fibroblast senescence in the pathology of idiopathic pulmonary fibrosis*. Am J Physiol Lung Cell Mol Physiol, 2018. **315**(2): p. L162-L172.
30. Selman, M., et al., *Idiopathic pulmonary fibrosis: prevailing and evolving hypotheses about its pathogenesis and implications for therapy*. Ann Intern Med, 2001. **134**(2): p. 136-51.
31. Collard, H.R., et al., *A new era in idiopathic pulmonary fibrosis: considerations for future clinical trials*. Eur Respir J, 2015. **46**(1): p. 243-9.
32. Moeller, A., et al., *The bleomycin animal model: a useful tool to investigate treatment options for idiopathic pulmonary fibrosis?* Int J Biochem Cell Biol, 2008. **40**(3): p. 362-82.
33. Sundararishnan, A., et al., *Engineered cell and tissue models of pulmonary fibrosis*. Adv Drug Deliv Rev, 2018. **129**: p. 78-94.
34. Cheng, B., et al., *An Integrated Stochastic Model of Matrix-Stiffness-Dependent Filopodial Dynamics*. Biophys J, 2016. **111**(9): p. 2051-2061.
35. Wang, H., et al., *Long-range force transmission in fibrous matrices enabled by tension-driven alignment of fibers*. Biophys J, 2014. **107**(11): p. 2592-603.
36. Baker, B.M., et al., *Cell-mediated fibre recruitment drives extracellular matrix mechanosensing in engineered fibrillar microenvironments*. Nat Mater, 2015. **14**(12): p. 1262-8.
37. Brauer, E., et al., *Collagen Fibrils Mechanically Contribute to Tissue Contraction in an In Vitro Wound Healing Scenario*. Advanced Science News, 2019: p. 1801780.
38. Eder, J., R. Sedrani, and C. Wiesmann, *The discovery of first-in-class drugs: origins and evolution*. Nat Rev Drug Discov, 2014. **13**(8): p. 577-87.
39. Liu, F., et al., *Feedback amplification of fibrosis through matrix stiffening and COX-2 suppression*. J Cell Biol, 2010. **190**(4): p. 693-706.
40. Grinnell, F., et al., *Differences in the regulation of fibroblast contraction of floating versus stressed collagen matrices*. J Biol Chem, 1999. **274**(2): p. 918-23.
41. Grinnell, F., et al., *Release of mechanical tension triggers apoptosis of human fibroblasts in a model of regressing granulation tissue*. Exp Cell Res, 1999. **248**(2): p. 608-19.

42. Zhubanchaliyev, A., et al., *Targeting Mechanotransduction at the Transcriptional Level: YAP and BRD4 Are Novel Therapeutic Targets for the Reversal of Liver Fibrosis*. *Front Pharmacol*, 2016. **7**: p. 462.
43. Hinz, B. and G. Gabbiani, *Fibrosis: recent advances in myofibroblast biology and new therapeutic perspectives*. *F1000 Biol Rep*, 2010. **2**: p. 78.
44. Liang, C.C., A.Y. Park, and J.L. Guan, *In vitro scratch assay: a convenient and inexpensive method for analysis of cell migration in vitro*. *Nat Protoc*, 2007. **2**(2): p. 329-33.
45. Tschumperlin, D.J. and S.S. Margulies, *Equibiaxial deformation-induced injury of alveolar epithelial cells in vitro*. *Am J Physiol*, 1998. **275**(6 Pt 1): p. L1173-83.
46. Douville, N.J., et al., *Combination of fluid and solid mechanical stresses contribute to cell death and detachment in a microfluidic alveolar model*. *Lab Chip*, 2011. **11**(4): p. 609-19.
47. Snyder-Talkington, B.N., et al., *Multi-walled carbon nanotubes induce human microvascular endothelial cellular effects in an alveolar-capillary co-culture with small airway epithelial cells*. *Part Fibre Toxicol*, 2013. **10**: p. 35.
48. Lenz, A.G., et al., *A dose-controlled system for air-liquid interface cell exposure and application to zinc oxide nanoparticles*. *Part Fibre Toxicol*, 2009. **6**: p. 32.
49. Lewis, K.J.R., et al., *Epithelial-mesenchymal crosstalk influences cellular behavior in a 3D alveolus-fibroblast model system*. *Biomaterials*, 2018. **155**: p. 124-134.
50. Prasad, S., C.M. Hogaboam, and G. Jarai, *Deficient repair response of IPF fibroblasts in a co-culture model of epithelial injury and repair*. *Fibrogenesis Tissue Repair*, 2014. **7**: p. 7.
51. Asmani, M., et al., *Fibrotic microtissue array to predict anti-fibrosis drug efficacy*. *Nat Commun*, 2018. **9**(1): p. 2066.
52. Chen, Z., et al., *Lung Microtissue Array to Screen the Fibrogenic Potential of Carbon Nanotubes*. *Sci Rep*, 2016. **6**: p. 31304.
53. Clark, R.A., et al., *Fibroblast invasive migration into fibronectin/fibrin gels requires a previously uncharacterized dermatan sulfate-CD44 proteoglycan*. *J Invest Dermatol*, 2004. **122**(2): p. 266-77.
54. Svee, K., et al., *Acute lung injury fibroblast migration and invasion of a fibrin matrix is mediated by CD44*. *J Clin Invest*, 1996. **98**(8): p. 1713-27.
55. Tuan, T.L., et al., *In vitro fibroplasia: matrix contraction, cell growth, and collagen production of fibroblasts cultured in fibrin gels*. *Exp Cell Res*, 1996. **223**(1): p. 127-34.

56. Wenzel, C., et al., *A novel 3D high-content assay identifies compounds that prevent fibroblast invasion into tissue surrogates*. *Exp Cell Res*, 2015. **339**(1): p. 35-43.
57. Xu, Q., et al., *In vitro models of TGF-beta-induced fibrosis suitable for high-throughput screening of antifibrotic agents*. *Am J Physiol Renal Physiol*, 2007. **293**(2): p. F631-40.
58. Moraes, C., et al., *Aqueous two-phase printing of cell-containing contractile collagen microgels*. *Biomaterials*, 2013. **34**(37): p. 9623-31.
59. Leung, B.M., et al., *Microscale 3D collagen cell culture assays in conventional flat-bottom 384-well plates*. *J Lab Autom*, 2015. **20**(2): p. 138-45.
60. Bell, E., B. Ivarsson, and C. Merrill, *Production of a tissue-like structure by contraction of collagen lattices by human fibroblasts of different proliferative potential in vitro*. *Proc Natl Acad Sci U S A*, 1979. **76**(3): p. 1274-8.
61. Hara, M., et al., *Construction of collagen gel scaffolds for mechanical stress analysis*. *Biosci Biotechnol Biochem*, 2014. **78**(3): p. 458-61.
62. Ilagan, R., et al., *Linear measurement of cell contraction in a capillary collagen gel system*. *Biotechniques*, 2010. **48**(2): p. 153-5.
63. Moraes, C., et al., *Supersoft lithography: candy-based fabrication of soft silicone microstructures*. *Lab Chip*, 2015. **15**(18): p. 3760-5.
64. Vernon, R.B. and M.D. Gooden, *An improved method for the collagen gel contraction assay*. *In Vitro Cell Dev Biol Anim*, 2002. **38**(2): p. 97-101.
65. Agarwal, A., et al., *Two-photon laser scanning microscopy of epithelial cell-modulated collagen density in engineered human lung tissue*. *Tissue Eng*, 2001. **7**(2): p. 191-202.
66. Ishikawa, S., K. Ishimori, and S. Ito, *A 3D epithelial-mesenchymal co-culture model of human bronchial tissue recapitulates multiple features of airway tissue remodeling by TGF-beta1 treatment*. *Respir Res*, 2017. **18**(1): p. 195.
67. Bravo, D.D.C.-R., T.; Chen, J.; Wang, J., *An impedance-based cell contraction assay using human primary smooth muscle cells and fibroblasts*. *Journal of Pharmacological and Toxicological Methods*, 2018. **89**: p. 47-53.
68. Jin, T., et al., *A novel collagen gel-based measurement technique for quantitation of cell contraction force*. *J R Soc Interface*, 2015. **12**(106).
69. Delvoye, P., et al., *Measurement of mechanical forces generated by skin fibroblasts embedded in a three-dimensional collagen gel*. *J Invest Dermatol*, 1991. **97**(5): p. 898-902.

70. Ma, S.H., et al., *Monodisperse collagen-gelatin beads as potential platforms for 3D cell culturing*. Journal of Materials Chemistry B, 2013. **1**(38): p. 5128-5136.
71. Chen, C.Z., et al., *The Scar-in-a-Jar: studying potential antifibrotic compounds from the epigenetic to extracellular level in a single well*. Br J Pharmacol, 2009. **158**(5): p. 1196-209.
72. Hong, S.M., et al., *Collagen microsphere production on a chip*. Lab on a Chip, 2012. **12**(18): p. 3277-3280.
73. Ulrich, T.A., et al., *Microscale mechanisms of agarose-induced disruption of collagen remodeling*. Biomaterials, 2011. **32**(24): p. 5633-42.
74. Wolters, P.J., et al., *Time for a change: is idiopathic pulmonary fibrosis still idiopathic and only fibrotic?* Lancet Respir Med, 2018. **6**(2): p. 154-160.
75. Sakai, N. and A.M. Tager, *Fibrosis of two: Epithelial cell-fibroblast interactions in pulmonary fibrosis*. Biochim Biophys Acta, 2013. **1832**(7): p. 911-21.
76. Horowitz, J.C. and V.J. Thannickal, *Epithelial-mesenchymal interactions in pulmonary fibrosis*. Semin Respir Crit Care Med, 2006. **27**(6): p. 600-12.
77. Fernandez-Perez, E.R., et al., *Ventilator settings and outcome of respiratory failure in chronic interstitial lung disease*. Chest, 2008. **133**(5): p. 1113-9.
78. Fumeaux, T., C. Rothmeier, and P. Jolliet, *Outcome of mechanical ventilation for acute respiratory failure in patients with pulmonary fibrosis*. Intensive Care Med, 2001. **27**(12): p. 1868-74.
79. Lin, H., et al., *Air-liquid interface (ALI) culture of human bronchial epithelial cell monolayers as an in vitro model for airway drug transport studies*. J Pharm Sci, 2007. **96**(2): p. 341-50.
80. Huh, D., et al., *Reconstituting organ-level lung functions on a chip*. Science, 2010. **328**(5986): p. 1662-8.
81. Elbert, K.J., et al., *Monolayers of human alveolar epithelial cells in primary culture for pulmonary absorption and transport studies*. Pharm Res, 1999. **16**(5): p. 601-8.
82. Srinivasan, B., et al., *TEER measurement techniques for in vitro barrier model systems*. J Lab Autom, 2015. **20**(2): p. 107-26.
83. Sucre, J.M.S., et al., *Successful Establishment of Primary Type II Alveolar Epithelium with 3D Organotypic Coculture*. Am J Respir Cell Mol Biol, 2018. **59**(2): p. 158-166.
84. LeBoeuf, R.D., et al., *Human fibrinogen specifically binds hyaluronic acid*. J Biol Chem, 1986. **261**(27): p. 12586-92.

85. Miron-Mendoza, M., et al., *Fibroblast-fibronectin patterning and network formation in 3D fibrin matrices*. Matrix Biol, 2017. **64**: p. 69-80.
86. Greiling, D. and R.A. Clark, *Fibronectin provides a conduit for fibroblast transmigration from collagenous stroma into fibrin clot provisional matrix*. J Cell Sci, 1997. **110 (Pt 7)**: p. 861-70.
87. Lin, F., et al., *Three-dimensional migration of human adult dermal fibroblasts from collagen lattices into fibrin/fibronectin gels requires syndecan-4 proteoglycan*. J Invest Dermatol, 2005. **124(5)**: p. 906-13.
88. Brown, L.F., et al., *Fibroblast migration in fibrin gel matrices*. Am J Pathol, 1993. **142(1)**: p. 273-83.
89. Hattori, N., et al., *Bleomycin-induced pulmonary fibrosis in fibrinogen-null mice*. J Clin Invest, 2000. **106(11)**: p. 1341-50.
90. Ploplis, V.A., et al., *A total fibrinogen deficiency is compatible with the development of pulmonary fibrosis in mice*. Am J Pathol, 2000. **157(3)**: p. 703-8.
91. Thannickal, V.J., et al., *Mechanisms of pulmonary fibrosis*. Annu Rev Med, 2004. **55**: p. 395-417.
92. Tomasek, J.J., et al., *Myofibroblasts and mechano-regulation of connective tissue remodelling*. Nat Rev Mol Cell Biol, 2002. **3(5)**: p. 349-63.
93. Leask, A. and D.J. Abraham, *TGF-beta signaling and the fibrotic response*. FASEB J, 2004. **18(7)**: p. 816-27.
94. Desmouliere, A., C. Chaponnier, and G. Gabbiani, *Tissue repair, contraction, and the myofibroblast*. Wound Repair Regen, 2005. **13(1)**: p. 7-12.
95. Darby, I.A., et al., *The myofibroblast, a key cell in normal and pathological tissue repair*. Cell Mol Life Sci, 2016. **73(6)**: p. 1145-57.
96. Rice, J.J., et al., *Engineering the regenerative microenvironment with biomaterials*. Adv Healthc Mater, 2013. **2(1)**: p. 57-71.
97. Xu, X., et al., *Hyaluronic Acid-Based Hydrogels: from a Natural Polysaccharide to Complex Networks*. Soft Matter, 2012. **8(12)**: p. 3280-3294.
98. Reed, M.J., et al., *TGF-beta 1 induces the expression of type I collagen and SPARC, and enhances contraction of collagen gels, by fibroblasts from young and aged donors*. J Cell Physiol, 1994. **158(1)**: p. 169-79.
99. Mio, T., et al., *Human bronchial epithelial cells modulate collagen gel contraction by fibroblasts*. Am J Physiol, 1998. **274(1 Pt 1)**: p. L119-26.

100. Nishiyama, T., et al., *Quantitative evaluation of the factors affecting the process of fibroblast-mediated collagen gel contraction by separating the process into three phases*. Coll Relat Res, 1988. **8**(3): p. 259-73.
101. Desmouliere, A., et al., *Transforming growth factor-beta 1 induces alpha-smooth muscle actin expression in granulation tissue myofibroblasts and in quiescent and growing cultured fibroblasts*. J Cell Biol, 1993. **122**(1): p. 103-11.
102. Wilson, S.E., Y.G. He, and S.A. Lloyd, *EGF, EGF receptor, basic FGF, TGF beta-1, and IL-1 alpha mRNA in human corneal epithelial cells and stromal fibroblasts*. Invest Ophthalmol Vis Sci, 1992. **33**(5): p. 1756-65.
103. Cillo, J.E., Jr., et al., *Growth factor and cytokine gene expression in mechanically strained human osteoblast-like cells: implications for distraction osteogenesis*. Oral Surg Oral Med Oral Pathol Oral Radiol Endod, 2000. **90**(2): p. 147-54.
104. Khalil, N., et al., *Macrophage production of transforming growth factor beta and fibroblast collagen synthesis in chronic pulmonary inflammation*. J Exp Med, 1989. **170**(3): p. 727-37.
105. Hinz, B., et al., *Mechanical tension controls granulation tissue contractile activity and myofibroblast differentiation*. Am J Pathol, 2001. **159**(3): p. 1009-20.
106. Christiansen, D.L., E.K. Huang, and F.H. Silver, *Assembly of type I collagen: fusion of fibril subunits and the influence of fibril diameter on mechanical properties*. Matrix Biol, 2000. **19**(5): p. 409-20.
107. Vernon, R.B., et al., *Reorganization of basement membrane matrices by cellular traction promotes the formation of cellular networks in vitro*. Lab Invest, 1992. **66**(5): p. 536-47.
108. Chung, S., et al., *Microfluidic Platforms for Studies of Angiogenesis, Cell Migration, and Cell-Cell Interactions*. Annals of Biomedical Engineering, 2010. **38**(3): p. 1164-1177.
109. Huang, G.Y., et al., *Microfluidic hydrogels for tissue engineering*. Biofabrication, 2011. **3**(1).
110. Cubaud, T. and T.G. Mason, *Capillary threads and viscous droplets in square microchannels*. Physics of Fluids, 2008. **20**(5).
111. Yamada, M., et al., *Cell-sized condensed collagen microparticles for preparing microengineered composite spheroids of primary hepatocytes*. Lab on a Chip, 2015. **15**(19): p. 3941-3951.
112. Epa, A.P., et al., *Normal Human Lung Epithelial Cells Inhibit Transforming Growth Factor-beta Induced Myofibroblast Differentiation via Prostaglandin E2*. PLoS One, 2015. **10**(8): p. e0135266.

113. Wang, M.C., et al., *Arterial stiffness correlated with cardiac remodelling in patients with chronic kidney disease*. *Nephrology (Carlton)*, 2007. **12**(6): p. 591-7.
114. Harley, B.A., et al., *A new technique for calculating individual dermal fibroblast contractile forces generated within collagen-GAG scaffolds*. *Biophys J*, 2007. **93**(8): p. 2911-22.
115. Wynn, T.A., *Cellular and molecular mechanisms of fibrosis*. *J Pathol*, 2008. **214**(2): p. 199-210.
116. Robin, J., *Methods for Measuring Hydroxyproline and Estimating In Vivo Rates of Collagen Synthesis and Degradation*. *Fibrosis Research*, 2005: p. 189-207.
117. Leeming, D.J., et al., *Enzyme-linked immunosorbent serum assay specific for the 7S domain of Collagen Type IV (P4NP 7S): A marker related to the extracellular matrix remodeling during liver fibrogenesis*. *Hepatol Res*, 2012. **42**(5): p. 482-93.
118. Cardoso, W.V., et al., *Collagen and elastin in human pulmonary emphysema*. *Am Rev Respir Dis*, 1993. **147**(4): p. 975-81.
119. Buttner, C., A. Skupin, and E.P. Rieber, *Transcriptional activation of the type I collagen genes COL1A1 and COL1A2 in fibroblasts by interleukin-4: analysis of the functional collagen promoter sequences*. *J Cell Physiol*, 2004. **198**(2): p. 248-58.
120. Wolman, M. and F.H. Kasten, *Polarized light microscopy in the study of the molecular structure of collagen and reticulin*. *Histochemistry*, 1986. **85**(1): p. 41-9.
121. Hu, Q., et al., *In vitro anti-fibrotic activities of herbal compounds and herbs*. *Nephrol Dial Transplant*, 2009. **24**(10): p. 3033-41.
122. Limper, A.H. and J. Roman, *Fibronectin. A versatile matrix protein with roles in thoracic development, repair and infection*. *Chest*, 1992. **101**(6): p. 1663-73.
123. Kadler, K.E., A. Hill, and E.G. Canty-Laird, *Collagen fibrillogenesis: fibronectin, integrins, and minor collagens as organizers and nucleators*. *Curr Opin Cell Biol*, 2008. **20**(5): p. 495-501.
124. Thannickal, V.J., et al., *Myofibroblast differentiation by transforming growth factor-beta1 is dependent on cell adhesion and integrin signaling via focal adhesion kinase*. *J Biol Chem*, 2003. **278**(14): p. 12384-9.
125. Klingberg, F., B. Hinz, and E.S. White, *The myofibroblast matrix: implications for tissue repair and fibrosis*. *J Pathol*, 2013. **229**(2): p. 298-309.
126. Cukierman, E., et al., *Taking cell-matrix adhesions to the third dimension*. *Science*, 2001. **294**(5547): p. 1708-12.

127. Baldock, C., et al., *Shape of tropoelastin, the highly extensible protein that controls human tissue elasticity*. Proc Natl Acad Sci U S A, 2011. **108**(11): p. 4322-7.
128. Hoff, C.R., D.R. Perkins, and J.M. Davidson, *Elastin gene expression is upregulated during pulmonary fibrosis*. Connect Tissue Res, 1999. **40**(2): p. 145-53.
129. Watanabe, K., et al., *Rapid decrease in forced vital capacity in patients with idiopathic pulmonary upper lobe fibrosis*. Respir Investig, 2012. **50**(3): p. 88-97.
130. Stucki, J.D., et al., *Medium throughput breathing human primary cell alveolus-on-chip model*. Sci Rep, 2018. **8**(1): p. 14359.
131. King, T.E., Jr., et al., *Idiopathic pulmonary fibrosis: relationship between histopathologic features and mortality*. Am J Respir Crit Care Med, 2001. **164**(6): p. 1025-32.
132. Hinz, B., *Tissue stiffness, latent TGF-beta1 activation, and mechanical signal transduction: implications for the pathogenesis and treatment of fibrosis*. Curr Rheumatol Rep, 2009. **11**(2): p. 120-6.
133. du Bois, R.M., et al., *Forced vital capacity in patients with idiopathic pulmonary fibrosis: test properties and minimal clinically important difference*. Am J Respir Crit Care Med, 2011. **184**(12): p. 1382-9.
134. Raghu, G., et al., *An official ATS/ERS/JRS/ALAT statement: idiopathic pulmonary fibrosis: evidence-based guidelines for diagnosis and management*. Am J Respir Crit Care Med, 2011. **183**(6): p. 788-824.
135. Anzueto, A. and M. Miravittles, *Pathophysiology of dyspnea in COPD*. Postgrad Med, 2017. **129**(3): p. 366-374.
136. Pellegrino, R., et al., *Interpretative strategies for lung function tests*. Eur Respir J, 2005. **26**(5): p. 948-68.
137. Huang, G., et al., *Functional and Biomimetic Materials for Engineering of the Three-Dimensional Cell Microenvironment*. Chem Rev, 2017. **117**(20): p. 12764-12850.
138. Elson, E.L. and G.M. Genin, *Tissue constructs: platforms for basic research and drug discovery*. Interface Focus, 2016. **6**(1): p. 20150095.
139. Green, J.J. and J.H. Elisseeff, *Mimicking biological functionality with polymers for biomedical applications*. Nature, 2016. **540**(7633): p. 386-394.
140. Seliktar, D., *Designing cell-compatible hydrogels for biomedical applications*. Science, 2012. **336**(6085): p. 1124-8.

141. Finkelstein, J.N., et al., *Early alterations in extracellular matrix and transforming growth factor beta gene expression in mouse lung indicative of late radiation fibrosis*. *Int J Radiat Oncol Biol Phys*, 1994. **28**(3): p. 621-31.
142. Hinz, B., *Mechanical aspects of lung fibrosis: a spotlight on the myofibroblast*. *Proc Am Thorac Soc*, 2012. **9**(3): p. 137-47.
143. Pinkerton, K.E., et al., *Architecture and Cellular Composition of the Air-Blood Tissue Barrier*, in *Comparative Biology of the Normal Lung*. 2015.
144. Mertz, D.R., T. Ahmed, and S. Takayama, *Engineering cell heterogeneity into organs-on-a-chip*. *Lab Chip*, 2018. **18**(16): p. 2378-2395.
145. Wynn, T.A., *Integrating mechanisms of pulmonary fibrosis*. *J Exp Med*, 2011. **208**(7): p. 1339-50.
146. Thiberville, L., et al., *Human in vivo fluorescence microimaging of the alveolar ducts and sacs during bronchoscopy*. *Eur Respir J*, 2009. **33**(5): p. 974-85.
147. Klingele, T.G. and N.C. Staub, *Alveolar shape changes with volume in isolated, air-filled lobes of cat lung*. *J Appl Physiol*, 1970. **28**(4): p. 411-4.
148. Haefeli-Bleuer, B. and E.R. Weibel, *Morphometry of the human pulmonary acinus*. *Anat Rec*, 1988. **220**(4): p. 401-14.
149. Yilmaz, C., et al., *Quantification of regional interstitial lung disease from CT-derived fractional tissue volume: a lung tissue research consortium study*. *Acad Radiol*, 2011. **18**(8): p. 1014-23.
150. Jones, M.G., et al., *Three-dimensional characterization of fibroblast foci in idiopathic pulmonary fibrosis*. *JCI Insight*, 2016. **1**(5).
151. Meng, P., et al., *Fibred confocal fluorescence microscopy in the diagnosis of interstitial lung diseases*. *J Thorac Dis*, 2016. **8**(12): p. 3505-3514.
152. Sznitman, J., *Respiratory microflows in the pulmonary acinus*. *J Biomech*, 2013. **46**(2): p. 284-98.
153. Bastacky, J., et al., *Alveolar lining layer is thin and continuous: low-temperature scanning electron microscopy of rat lung*. *J Appl Physiol* (1985), 1995. **79**(5): p. 1615-28.
154. Mercer, R.R., M.L. Russell, and J.D. Crapo, *Alveolar septal structure in different species*. *J Appl Physiol* (1985), 1994. **77**(3): p. 1060-6.
155. Hospodiuk, M., et al., *The bioink: A comprehensive review on bioprintable materials*. *Biotechnol Adv*, 2017. **35**(2): p. 217-239.

156. Hwang, H.H., et al., *3D-Printing of Functional Biomedical Microdevices via Light- and Extrusion-Based Approaches*. *Small Methods*, 2018. **2**(2).
157. Pati, F., et al., *Printing three-dimensional tissue analogues with decellularized extracellular matrix bioink*. *Nat Commun*, 2014. **5**: p. 3935.
158. Hecker, L., et al., *Reversal of persistent fibrosis in aging by targeting Nox4-Nrf2 redox imbalance*. *Sci Transl Med*, 2014. **6**(231): p. 231ra47.
159. Yanai, H., et al., *Cellular senescence-like features of lung fibroblasts derived from idiopathic pulmonary fibrosis patients*. *Aging (Albany NY)*, 2015. **7**(9): p. 664-72.
160. Mosesson, M.W., *Fibrinogen and fibrin structure and functions*. *J Thromb Haemost*, 2005. **3**(8): p. 1894-904.
161. Laurens, N., P. Koolwijk, and M.P. de Maat, *Fibrin structure and wound healing*. *J Thromb Haemost*, 2006. **4**(5): p. 932-9.
162. Moriwaki, H., et al., *Overexpression of urokinase by macrophages or deficiency of plasminogen activator inhibitor type 1 causes cardiac fibrosis in mice*. *Circ Res*, 2004. **95**(6): p. 637-44.
163. Flevaris, P. and D. Vaughan, *The Role of Plasminogen Activator Inhibitor Type-1 in Fibrosis*. *Semin Thromb Hemost*, 2017. **43**(2): p. 169-177.
164. Chaires-Rosas, C.P., et al., *Differential adhesion and fibrinolytic activity of mesenchymal stem cells from human bone marrow, placenta, and Wharton's jelly cultured in a fibrin hydrogel*. *J Tissue Eng*, 2019. **10**: p. 2041731419840622.
165. Collen, D., *Ham-Wasserman lecture: role of the plasminogen system in fibrin-homeostasis and tissue remodeling*. *Hematology Am Soc Hematol Educ Program*, 2001: p. 1-9.
166. Muhleder, S., et al., *The role of fibrinolysis inhibition in engineered vascular networks derived from endothelial cells and adipose-derived stem cells*. *Stem Cell Res Ther*, 2018. **9**(1): p. 35.
167. Roussel, B.D., et al., *HMGB-1 promotes fibrinolysis and reduces neurotoxicity mediated by tissue plasminogen activator*. *J Cell Sci*, 2011. **124**(Pt 12): p. 2070-6.
168. Castillo, O., et al., *Endothelial fibrinolytic response onto an evolving matrix of fibrin*. *BMC Hematol*, 2016. **16**: p. 9.
169. Kanamaru, Y., et al., *Mast cell-mediated remodeling and fibrinolytic activity protect against fatal glomerulonephritis*. *J Immunol*, 2006. **176**(9): p. 5607-15.
170. Cesarman-Maus, G. and K.A. Hajjar, *Molecular mechanisms of fibrinolysis*. *Br J Haematol*, 2005. **129**(3): p. 307-21.

171. Kucharewicz, I., et al., *The plasmin system in airway remodeling*. Thromb Res, 2003. **112**(1-2): p. 1-7.
172. Levi, M., et al., *Assessment of the relative contribution of different protease inhibitors to the inhibition of plasmin in vivo*. Thromb Haemost, 1993. **69**(2): p. 141-6.
173. Bouma, B.N. and L.O. Mosnier, *Thrombin activatable fibrinolysis inhibitor (TAFI)--how does thrombin regulate fibrinolysis?* Ann Med, 2006. **38**(6): p. 378-88.
174. Douglas, S.A., et al., *Human cathepsins K, L, and S: Related proteases, but unique fibrinolytic activity*. Biochim Biophys Acta Gen Subj, 2018. **1862**(9): p. 1925-1932.
175. Loskutoff, D.J. and J.P. Quigley, *PAI-1, fibrosis, and the elusive provisional fibrin matrix*. J Clin Invest, 2000. **106**(12): p. 1441-3.
176. Sisson, T.H. and R.H. Simon, *The plasminogen activation system in lung disease*. Curr Drug Targets, 2007. **8**(9): p. 1016-29.
177. Swaisgood, C.M., et al., *The development of bleomycin-induced pulmonary fibrosis in mice deficient for components of the fibrinolytic system*. Am J Pathol, 2000. **157**(1): p. 177-87.
178. Chester, D. and A.C. Brown, *The role of biophysical properties of provisional matrix proteins in wound repair*. Matrix Biol, 2017. **60-61**: p. 124-140.
179. Lorimier, S., et al., *The rate of fibrinolysis is increased by free retraction of human gingival fibroblast populated fibrin lattices*. Int J Biochem Cell Biol, 1997. **29**(1): p. 181-9.
180. Murphy, S.V., A. Skardal, and A. Atala, *Evaluation of hydrogels for bio-printing applications*. J Biomed Mater Res A, 2013. **101**(1): p. 272-84.
181. Ahmed, T.A., E.V. Dare, and M. Hincke, *Fibrin: a versatile scaffold for tissue engineering applications*. Tissue Eng Part B Rev, 2008. **14**(2): p. 199-215.
182. Guillotin, B., et al., *Laser assisted bioprinting of engineered tissue with high cell density and microscale organization*. Biomaterials, 2010. **31**(28): p. 7250-6.
183. Xu, T., et al., *Viability and electrophysiology of neural cell structures generated by the inkjet printing method*. Biomaterials, 2006. **27**(19): p. 3580-8.
184. Li, Y., et al., *Fibrin gel as an injectable biodegradable scaffold and cell carrier for tissue engineering*. ScientificWorldJournal, 2015. **2015**: p. 685690.

185. Gorodetsky, R., et al., *Fibrin microbeads (FMB) as biodegradable carriers for culturing cells and for accelerating wound healing*. *J Invest Dermatol*, 1999. **112**(6): p. 866-72.
186. Johansson, H.O., et al., *Driving forces for phase separation and partitioning in aqueous two-phase systems*. *J Chromatogr B Biomed Sci Appl*, 1998. **711**(1-2): p. 3-17.
187. Pratt, C.W. and D.M. Monroe, *Microplate coagulation assays*. *Biotechniques*, 1992. **13**(3): p. 430-3.
188. Ilich, A., I. Bokarev, and N.S. Key, *Global assays of fibrinolysis*. *Int J Lab Hematol*, 2017. **39**(5): p. 441-447.
189. Collet, J.P., et al., *Influence of fibrin network conformation and fibrin fiber diameter on fibrinolysis speed: dynamic and structural approaches by confocal microscopy*. *Arterioscler Thromb Vasc Biol*, 2000. **20**(5): p. 1354-61.
190. Samarakoon, R., J.M. Overstreet, and P.J. Higgins, *TGF-beta signaling in tissue fibrosis: redox controls, target genes and therapeutic opportunities*. *Cell Signal*, 2013. **25**(1): p. 264-8.
191. Tuan, T.L., et al., *Elevated levels of plasminogen activator inhibitor-1 may account for the altered fibrinolysis by keloid fibroblasts*. *J Invest Dermatol*, 1996. **106**(5): p. 1007-11.
192. Verrecchia, F., M.L. Chu, and A. Mauviel, *Identification of novel TGF-beta /Smad gene targets in dermal fibroblasts using a combined cDNA microarray/promoter transactivation approach*. *J Biol Chem*, 2001. **276**(20): p. 17058-62.
193. Mu, X.C. and P.J. Higgins, *Differential growth state-dependent regulation of plasminogen activator inhibitor type-1 expression in senescent IMR-90 human diploid fibroblasts*. *J Cell Physiol*, 1995. **165**(3): p. 647-57.
194. Martens, J.W., et al., *Aging of stromal-derived human breast fibroblasts might contribute to breast cancer progression*. *Thromb Haemost*, 2003. **89**(2): p. 393-404.
195. Serrano, M., et al., *Oncogenic ras provokes premature cell senescence associated with accumulation of p53 and p16INK4a*. *Cell*, 1997. **88**(5): p. 593-602.
196. Vasta, J.D., et al., *Selective Inhibition of Collagen Prolyl 4-Hydroxylase in Human Cells*. *ACS Chem Biol*, 2016. **11**(1): p. 193-9.
197. Pardo, A. and M. Selman, *Lung Fibroblasts, Aging, and Idiopathic Pulmonary Fibrosis*. *Ann Am Thorac Soc*, 2016. **13 Suppl 5**: p. S417-S421.

198. Cesari, M., M. Pahor, and R.A. Incalzi, *Plasminogen activator inhibitor-1 (PAI-1): a key factor linking fibrinolysis and age-related subclinical and clinical conditions*. Cardiovasc Ther, 2010. **28**(5): p. e72-91.
199. Gorlach, A., et al., *Reactive oxygen species modulate HIF-1 mediated PAI-1 expression: involvement of the GTPase Rac1*. Thromb Haemost, 2003. **89**(5): p. 926-35.
200. He, T., et al., *Oxidative exposure impairs TGF-beta pathway via reduction of type II receptor and SMAD3 in human skin fibroblasts*. Age (Dordr), 2014. **36**(3): p. 9623.
201. Yasuda, K., K. Aoshiba, and A. Nagai, *Transforming growth factor-beta promotes fibroblast apoptosis induced by H2O2*. Exp Lung Res, 2003. **29**(3): p. 123-34.
202. Gorres, K.L. and R.T. Raines, *Prolyl 4-hydroxylase*. Crit Rev Biochem Mol Biol, 2010. **45**(2): p. 106-24.
203. Bruick, R.K. and S.L. McKnight, *A conserved family of prolyl-4-hydroxylases that modify HIF*. Science, 2001. **294**(5545): p. 1337-40.
204. Schuliga, M., et al., *The fibrogenic actions of the coagulant and plasminogen activation systems in pulmonary fibrosis*. Int J Biochem Cell Biol, 2018. **97**: p. 108-117.
205. Knuppel, L., et al., *A Novel Antifibrotic Mechanism of Nintedanib and Pirfenidone. Inhibition of Collagen Fibril Assembly*. Am J Respir Cell Mol Biol, 2017. **57**(1): p. 77-90.
206. Clark, R.A., *Fibrin and wound healing*. Ann N Y Acad Sci, 2001. **936**: p. 355-67.
207. Midwood, K.S., L.V. Williams, and J.E. Schwarzbauer, *Tissue repair and the dynamics of the extracellular matrix*. Int J Biochem Cell Biol, 2004. **36**(6): p. 1031-7.
208. Frantz, C., K.M. Stewart, and V.M. Weaver, *The extracellular matrix at a glance*. J Cell Sci, 2010. **123**(Pt 24): p. 4195-200.
209. Herouy, Y., et al., *Plasminogen activation in venous leg ulcers*. Br J Dermatol, 2000. **143**(5): p. 930-6.
210. Li, W.Y., et al., *Plasminogen activator/plasmin system: a major player in wound healing?* Wound Repair Regen, 2003. **11**(4): p. 239-47.
211. Richeldi, L., et al., *Corticosteroids for idiopathic pulmonary fibrosis*. Cochrane Database Syst Rev, 2003(3): p. CD002880.

212. Davies, H.R., L. Richeldi, and E.H. Walters, *Immunomodulatory agents for idiopathic pulmonary fibrosis*. Cochrane Database Syst Rev, 2003(3): p. CD003134.
213. Juarez, M.M., et al., *Acute exacerbation of idiopathic pulmonary fibrosis-a review of current and novel pharmacotherapies*. J Thorac Dis, 2015. 7(3): p. 499-519.
214. Menou, A., J. Duitman, and B. Crestani, *The impaired proteases and anti-proteases balance in Idiopathic Pulmonary Fibrosis*. Matrix Biol, 2018. 68-69: p. 382-403.
215. Adnot, S., M. Breau, and A. Houssaini, *PAI-1: A New Target for Controlling Lung-Cell Senescence and Fibrosis?* Am J Respir Cell Mol Biol, 2020. 62(3): p. 271-272.
216. Schuliga, M., et al., *The fibrogenic actions of lung fibroblast-derived urokinase: a potential drug target in IPF*. Sci Rep, 2017. 7: p. 41770.
217. Probst, C.K., et al., *Vascular Permeability in the Fibrotic Lung*. Eur Respir J, 2020.
218. Czekay, R.P., et al., *Plasminogen activator inhibitor-1 detaches cells from extracellular matrices by inactivating integrins*. J Cell Biol, 2003. 160(5): p. 781-91.
219. Marudamuthu, A.S., et al., *Plasminogen activator inhibitor-1 suppresses profibrotic responses in fibroblasts from fibrotic lungs*. J Biol Chem, 2015. 290(15): p. 9428-41.
220. Tuan, T.L., et al., *Adenoviral overexpression and small interfering RNA suppression demonstrate that plasminogen activator inhibitor-1 produces elevated collagen accumulation in normal and keloid fibroblasts*. Am J Pathol, 2008. 173(5): p. 1311-25.
221. Junqueira, L.C., G. Bignolas, and R.R. Brentani, *Picrosirius staining plus polarization microscopy, a specific method for collagen detection in tissue sections*. Histochem J, 1979. 11(4): p. 447-55.
222. Wegner, K.A., et al., *Fluorescence of Picrosirius Red Multiplexed With Immunohistochemistry for the Quantitative Assessment of Collagen in Tissue Sections*. J Histochem Cytochem, 2017. 65(8): p. 479-490.
223. Leipnitz, G., et al., *Reference values and variability of plasminogen in healthy blood donors and its relation to parameters of the fibrinolytic system*. Haemostasis, 1988. 18 Suppl 1: p. 61-8.
224. Dvorak, H.F., *Vascular permeability to plasma, plasma proteins, and cells: an update*. Curr Opin Hematol, 2010. 17(3): p. 225-9.

225. Gharaee-Kermani, M., et al., *Recent advances in molecular targets and treatment of idiopathic pulmonary fibrosis: focus on TGFbeta signaling and the myofibroblast*. *Curr Med Chem*, 2009. **16**(11): p. 1400-17.
226. Walsh, B.J., et al., *Microplate reader-based quantitation of collagens*. *Anal Biochem*, 1992. **203**(2): p. 187-90.
227. Borges, L.F., S.R. Taboga, and P.S. Gutierrez, *Simultaneous observation of collagen and elastin in normal and pathological tissues: analysis of Sirius-red-stained sections by fluorescence microscopy*. *Cell Tissue Res*, 2005. **320**(3): p. 551-2.
228. Verrecchia, F. and A. Mauviel, *Transforming growth factor-beta and fibrosis*. *World J Gastroenterol*, 2007. **13**(22): p. 3056-62.
229. Dennler, S., et al., *Direct binding of Smad3 and Smad4 to critical TGF beta-inducible elements in the promoter of human plasminogen activator inhibitor-type 1 gene*. *EMBO J*, 1998. **17**(11): p. 3091-100.
230. Idell, S., et al., *Mechanisms of fibrin formation and lysis by human lung fibroblasts: influence of TGF-beta and TNF-alpha*. *Am J Physiol*, 1992. **263**(4 Pt 1): p. L487-94.
231. Li, X.X., et al., *Idiopathic pulmonary fibrosis in relation to gene polymorphisms of transforming growth factor-beta1 and plasminogen activator inhibitor 1*. *Chin Med J (Engl)*, 2011. **124**(13): p. 1923-7.
232. Huang, X., et al., *Matrix stiffness-induced myofibroblast differentiation is mediated by intrinsic mechanotransduction*. *Am J Respir Cell Mol Biol*, 2012. **47**(3): p. 340-8.
233. Bernstein, A.M., et al., *Urokinase receptor cleavage: a crucial step in fibroblast-to-myofibroblast differentiation*. *Mol Biol Cell*, 2007. **18**(7): p. 2716-27.
234. Zhang, K., et al., *Myofibroblasts and their role in lung collagen gene expression during pulmonary fibrosis. A combined immunohistochemical and in situ hybridization study*. *Am J Pathol*, 1994. **145**(1): p. 114-25.
235. Vancheri, C., *Idiopathic pulmonary fibrosis: an altered fibroblast proliferation linked to cancer biology*. *Proc Am Thorac Soc*, 2012. **9**(3): p. 153-7.
236. Sueblinvong, V., et al., *Predisposition for disrepair in the aged lung*. *Am J Med Sci*, 2012. **344**(1): p. 41-51.
237. Amara, N., et al., *NOX4/NADPH oxidase expression is increased in pulmonary fibroblasts from patients with idiopathic pulmonary fibrosis and mediates TGFbeta1-induced fibroblast differentiation into myofibroblasts*. *Thorax*, 2010. **65**(8): p. 733-8.

238. Kadoya, K., et al., *Specific Features of Fibrotic Lung Fibroblasts Highly Sensitive to Fibrotic Processes Mediated via TGF-beta-ERK5 Interaction*. Cell Physiol Biochem, 2019. **52**(4): p. 822-837.
239. Wang, Y., et al., *N-methyl-D-aspartate receptor activation mediates lung fibroblast proliferation and differentiation in hyperoxia-induced chronic lung disease in newborn rats*. Respir Res, 2016. **17**(1): p. 136.
240. Zhang, C., et al., *Ifenprodil and Flavopiridol Identified by Genomewide RNA Interference Screening as Effective Drugs To Ameliorate Murine Acute Lung Injury after Influenza A H5N1 Virus Infection*. mSystems, 2019. **4**(6).
241. Li, X., et al., *NMDA receptor activation inhibits the antifibrotic effect of BM-MSCs on bleomycin-induced pulmonary fibrosis*. Am J Physiol Lung Cell Mol Physiol, 2018. **315**(3): p. L404-L421.
242. Rangarajan, S., et al., *Novel Mechanisms for the Antifibrotic Action of Nintedanib*. Am J Respir Cell Mol Biol, 2016. **54**(1): p. 51-9.
243. Conte, E., et al., *Effect of pirfenidone on proliferation, TGF-beta-induced myofibroblast differentiation and fibrogenic activity of primary human lung fibroblasts*. Eur J Pharm Sci, 2014. **58**: p. 13-9.
244. Staab-Weijnitz, C.A., et al., *FK506-Binding Protein 10, a Potential Novel Drug Target for Idiopathic Pulmonary Fibrosis*. Am J Respir Crit Care Med, 2015. **192**(4): p. 455-67.
245. Huang, W.T., et al., *Therapeutic value of small molecule inhibitor to plasminogen activator inhibitor-1 for lung fibrosis*. Am J Respir Cell Mol Biol, 2012. **46**(1): p. 87-95.
246. Maher, T.M., et al., *Safety, tolerability, pharmacokinetics, and pharmacodynamics of GLPG1690, a novel autotaxin inhibitor, to treat idiopathic pulmonary fibrosis (FLORA): a phase 2a randomised placebo-controlled trial*. Lancet Respir Med, 2018. **6**(8): p. 627-635.
247. Habel, D.M. and C.M. Hogaboam, *Heterogeneity of Fibroblasts and Myofibroblasts in Pulmonary Fibrosis*. Curr Pathobiol Rep, 2017. **5**(2): p. 101-110.
248. Chapman, H.A., *Epithelial-mesenchymal interactions in pulmonary fibrosis*. Annu Rev Physiol, 2011. **73**: p. 413-35.
249. Bhattacharya, J. and M.A. Matthay, *Regulation and repair of the alveolar-capillary barrier in acute lung injury*. Annu Rev Physiol, 2013. **75**: p. 593-615.
250. Camelo, A., et al., *The epithelium in idiopathic pulmonary fibrosis: breaking the barrier*. Front Pharmacol, 2014. **4**: p. 173.

251. Selman, M. and A. Pardo, *Idiopathic pulmonary fibrosis: an epithelial/fibroblastic cross-talk disorder*. *Respir Res*, 2002. **3**: p. 3.
252. Florez-Sampedro, L., S. Song, and B.N. Melgert, *The diversity of myeloid immune cells shaping wound repair and fibrosis in the lung*. *Regeneration (Oxf)*, 2018. **5**(1): p. 3-25.
253. Prasse, A., et al., *A vicious circle of alveolar macrophages and fibroblasts perpetuates pulmonary fibrosis via CCL18*. *Am J Respir Crit Care Med*, 2006. **173**(7): p. 781-92.
254. Lehtonen, S.T., et al., *Pirfenidone and nintedanib modulate properties of fibroblasts and myofibroblasts in idiopathic pulmonary fibrosis*. *Respir Res*, 2016. **17**: p. 14.
255. Mora, A.L., et al., *Emerging therapies for idiopathic pulmonary fibrosis, a progressive age-related disease*. *Nat Rev Drug Discov*, 2017. **16**(11): p. 810.
256. Lehmann, M., et al., *Differential effects of Nintedanib and Pirfenidone on lung alveolar epithelial cell function in ex vivo murine and human lung tissue cultures of pulmonary fibrosis*. *Respir Res*, 2018. **19**(1): p. 175.
257. Bellamri, N., et al., *Alteration of human macrophage phenotypes by the anti-fibrotic drug nintedanib*. *Int Immunopharmacol*, 2019. **72**: p. 112-123.
258. Li, Z., et al., *Pirfenidone suppresses MAPK signalling pathway to reverse epithelial-mesenchymal transition and renal fibrosis*. *Nephrology (Carlton)*, 2017. **22**(8): p. 589-597.
259. Toda, M., et al., *Pirfenidone suppresses polarization to M2 phenotype macrophages and the fibrogenic activity of rat lung fibroblasts*. *J Clin Biochem Nutr*, 2018. **63**(1): p. 58-65.
260. Whyte, C.S., et al., *Fibrinolytic abnormalities in acute respiratory distress syndrome (ARDS) and versatility of thrombolytic drugs to treat COVID-19*. *J Thromb Haemost*, 2020.
261. Gomez-Salinerio, J.M. and S. Rafii, *Plasmin regulation of acute cytokine storm*. *Blood*, 2017. **130**(1): p. 5-6.
262. Koli, K., et al., *Transforming growth factor-beta activation in the lung: focus on fibrosis and reactive oxygen species*. *Antioxid Redox Signal*, 2008. **10**(2): p. 333-42.
263. Shetty, S., et al., *The fibrinolytic system and the regulation of lung epithelial cell proteolysis, signaling, and cellular viability*. *Am J Physiol Lung Cell Mol Physiol*, 2008. **295**(6): p. L967-75.

